Dynamics of EF-Tu/ternary complex in live *E. coli* using superresolution imaging

By
Mainak Mustafi

A dissertation submitted in partial fulfillment of the requirements for the degree of

Doctor of Philosophy
(Chemistry)

at the

UNIVERSITY OF WISCONSIN-MADISON
2019

Date of final oral examination: 12/17/2019

The dissertation is approved by the following members of the Final Oral Committee:

James C. Weisshaar, Professor, Chemistry

M. Thomas Record Jr., Professor, Chemistry & Biochemistry

Samuel H. Gellman, Professor, Chemistry

Jue D. (Jade) Wang, Professor, Bacteriology

Table of Content

Dynamics of EF-Tu/ternary complex in live *E. coli* using superresolution imaging

Under the supervision of Prof James C. weisshaar

At University of Wisconsin-Madison

Abstract:

Translation elongation is a complicated process where amino acids are added to the peptide chain within the ribosomes for protein production. In each elongation cycle the ribosome samples different aminoacyl tRNA (aa-tRNA) species to find a match for the mRNA codon. There are around 40-45 different tRNA species in *E. coli* and on an average all of them have to be sampled to find a match. Then the aa-tRNA transfers the amino acid to the growing peptide chain and the deacylated tRNA leaves. For cells growing in good growth medium, the entire cycle takes around 50 ms. Different proteins (elongation factors) are involved in different steps of the elongations cycle, the two major ones being EF-Tu and EF-G. EF-Tu forms a ternary complex with aa-tRNA and GTP and thus brings the aa-tRNA to the ribosome. The elongation cycle has been studied in great detail using both bulk and single molecule experiments, but the initial interaction of ternary complex with ribosome (specifically with L7/L12 stalk) is not properly understood, mainly due to the lack of structural data. Using superresolution imaging (PALM), we have studied dynamics of ternary complex and L7/L12 stalk interaction. Our results have shown that the interaction is highly transient and multiple ternary complexes can bind to translating ribosomes at the same time. This high binding stoichiometry can lead to high concentration of tRNA around ribosomes for efficient translation. We have further incorporated the effects of nutrient limitation, osmotic effects and various translation halting drug treatment on the dynamics of EF-Tu/ternary complex

Acknowledgements:

I am thankful to all the people who have supported and helped me during my time in graduate school. Completing a PhD thesis is no easy task and my thesis would in no way have been successful without the support of many friends, family members and colleagues.

First and foremost, I would like to thank my family – my parents and my younger brother. I am originally from the city of Kolkata in West Bengal, India. My parents are still based there. My brother is doing a job in Bangalore, India. My entire family have always supported me and gave me the encouragement whenever I have needed it and I believe that has contributed enormously towards my successful PhD journey. They have always believed in me and my abilities and have pushed me towards new challenges. Whenever I have needed any help, they were always there to support me and for this I will always be grateful. It has been difficult to stay in a different country for over five years, away from my family, but their constant support has made my PhD journey easier.

I would also like to thank my advisor, Prof James Weisshaar for his mentorship. A PhD cannot be successful without a supportive PI and Jim has been very supportive to me during my time in the Weisshaar lab. Jim has taught me a great deal in the last five years in how to be a good scientist. He has taught me to be critical about my own data so that I can avoid making mistakes. Jim has also taught me a lot on how to obtain quantitative information from my experimental data, which has helped to expand my own analytical ability. He has also helped with my future planning. Thus, I am very grateful to him. He has had tremendous contribution in my scientific growth.

My PhD wouldn't have gone nearly as well if it weren't for my extremely supportive lab-mates. The Weisshaar lab has decreased in size significantly, since I have joined, but the enthusiasm for doing good research has never changed. Such positive attitude and hard-working nature of my colleagues have pushed me into doing better research. There are lot of people I am thankful to in this lab. I will start by acknowledging Heejun, who was my initial mentor. I have only worked with him for a year, but he has taught me a lot in that short period of time. I had almost no biology background before joining this lab and after working with Heejun my knowledge increased significantly. He taught me numerous molecular biology techniques, which have been extremely useful throughout my PhD. Soni was the one who taught me how to do the superresolution imaging experiments. She is an extremely smart person and we have had numerous scientific discussions which have benefitted me tremendously. Apart from the scientific discussions, we also had discussions about basketball, soccer and cs, which brought a refreshing feel to our daily scientific lives. Wenting, Nikolai and Yanyu were my other office-mates. They are all extremely smart people and all have done some really interesting research. I have had many discussions with them and all have supported me a lot throughout the years. Apart from science, Wenting always had lot of snacks and always made sure no one ever went hungry in the lab. Nikolai and I have shared an interest in gaming and we have also had a lan party. Yanyu joined the lab a year after me and is the last graduate student in this lab. He is one of the smartest people I have met and we have even collaborated on few research projects. The past year has been mostly the two of us in the lab and I believe both of us have contributed to each other's research significantly. He has been extremely dependable. Celine is the newest addition to our group. She is here on a sabbatical from CMB, CNRS-Orleans, France. She is a very good structural biologist and extremely knowledgeable in AMPs. Within a short period she

has taught me a lot about structural and functional relationship in different AMPs. It has been great to have her around.

Zhilin, Ranga and Anurag were in a different student office but are in no way less impactful in my PhD life. They were doing totally different research with almost no overlap with mine but still they helped me whenever I needed it. They were never shy of giving me suggestions which proved to be extremely beneficial. It has been great to have them around as lab-mates. Zhilin has also taught me how to do their standard experimental assays, which have helped me to broaden my experimental skills. I am extremely grateful to have had such wonderful lab-mates.

I am also thankful to all the people who have helped me with my research in grad school. Hector from Prof Rick Gourse's lab, who have helped me a lot when I was facing trouble with PCR. Munish, Xian and Emily, from Prof Tom Record's lab, who have helped me with measuring osmolality of my growth media. Rachel, from Prof Lloyd Smith's lab, who have spent a significant amount of time doing Mass Spec measurements of my cell lysates. Charu, from Prof Emery Bresnick's lab, who have taught me how to do qPCR and Western blot. Every one of them have had a significant impact on my research I am grateful to them for their time and effort.

I have enjoyed my time in grad school and in a big way I owe it to all my awesome friends. I am extremely grateful to Anurag and Munish, who have always been my closest friends since I have arrived in Madison. We have gone to several concerts, tried numerous restaurants, gone bowling and did numerous other activities. Without them my life would have been pretty dull. I am also extremely lucky to have friends like Kushal, Prasanth and Tanmoy, who have joined grad school after me but in no way contributed less than my other friends. We

have gone to watch numerous movies together and even went for several road trips together. Life would be very different if these people wouldn't have been around, and so I am extremely grateful to them. Also, I cannot forget Sriteja, who was an awesome senior and helped me anytime I needed it. Charu was another person who shared my enthusiasm for new restaurants. We have tried numerous new places together and I have enjoyed them all. She is an extremely enthusiastic person and have motivated me whenever I needed it. I am lucky to have her as a friend.

I cannot forget my friends from my undergraduate life who are still a constant source of support for me. I would like to thank Ayan, Samata, Soumya, Parmeet, Ahanjit, AKD, Piyush, Akula, Kapil, Arpit and Yash for all the phone calls and help throughout all these years. They will always be a big part of my life.

Chapter 1:

Introduction

Inside every organism, many different complex and multi-step biological processes occur in tandem for its efficient growth. Often, numerous proteins and macromolecular complexes are involved in each step of the different cellular processes. To understand how these processes work, it is important to understand how these proteins interact with each other from both structural and temporal respect. Many of these processes share mechanistic similarities among different organisms even though the proteins involved and the complexity varies. All cellular organisms can broadly be characterized into 2 different groups – Eukaryotes and Prokaryotes. Eukaryotes are multicellular organisms, such as mammals, and in these cells the different processes occur in defined cellular compartment or organelles. Prokaryotes are single celled organisms – like bacteria, and in these cells, there is no defined organelle. My work has been focused on a specific bacterium called *Escherichia coli* or *E. coli* – which is a model organism, as it has been widely studied over the years.

Most of our understanding about these cellular processes come from the *in vitro* experiments performed over the years. These experiments have been instrumental in determining the proteins involved in the different processes and their functions. Structural and biochemical studies provide a lot of information on how these proteins interact among themselves. There are also many different kinetic studies performed on the protein complexes which gives information about the rate and stability of the different steps in these processes. Even though these *in vitro* experiments have expanded our knowledge about the system, how a protein behaves in a live cell might be significantly different compared to *in vitro* conditions. Much of the difference is observed in the dynamics of the protein interactions because the cell is very densely packed. Due to such crowding, the rate of interactions in a live cell can be significantly different compared to *in vitro* conditions. It is known that binding constants are higher *in vivo* compared to *in vitro*

values [1]. Thus, it is important to study these systems inside a live cell to get a more accurate understanding of their dynamics.

Studying live cell dynamics of individual proteins has been a challenging task until recently. Fluorescence imaging is a powerful tool to visualize the interior of the cell. For this technique, the protein of interest is tagged with a fluorophore/fluorescent protein which serves as a proxy for the location of the protein of interest. But due to the diffraction limit of ~250 nm, it has not been possible to study single proteins [2]. Any object below this limit cannot be resolved in a microscope and since most proteins are ~20-30 times smaller than this limit, it has been impossible to study individual proteins. Since the development of superresolution microscopy techniques, it has become a lot easier to visualize individual proteins in a cell and their interacting partners. This breakthrough initially happened around the year 1994 when Stefan Hell invented the Stimulated Emission Depletion microscope (STED) which could achieve resolution ~10-20 nm depending on the intensity of the laser used [3, 4]. In this technique, first all the fluorophores are excited by a laser and then the excited molecules are illuminated by a donut shaped laser beam, which causes stimulated emission. Only the molecules at the center of the donut beam can still show fluorescence. The power of the donut shaped beam determines the resolution. But this technique was not completely suitable for biological samples which are highly prone to laser damage.

In the late 90s, W.E. Moerner discovered that when a laser of specific wavelength is shined on a variant of green fluorescent protein (GFP), it can turn its fluorescent on or off [5]. This discovery led to a revolution in fluorescence microscopy. Using this principle, in the year 2006, 3 different groups published their work on how to overcome the diffraction limit of optical microscopy and achieve resolution as high as ~30 nm. All the 3 techniques (PALM, STORM and

FPALM) worked on very similar principle of stochastically turning the fluorophore on and off and only imaging a single protein tagged with the fluorophore at a time [6-8]. Also, low powered lasers can be used for these techniques which didn't cause appreciable laser damage to the live cells. Thus, information of a single protein as well as its interaction dynamics in live cells can now be obtained. A schematic of the PALM technique is shown in Fig 1.1. In 2014, Stefan Hell, W. E. Moerner and Eric Betzig were awarded the Nobel prize in Chemistry for their contributions towards superresolution imaging.

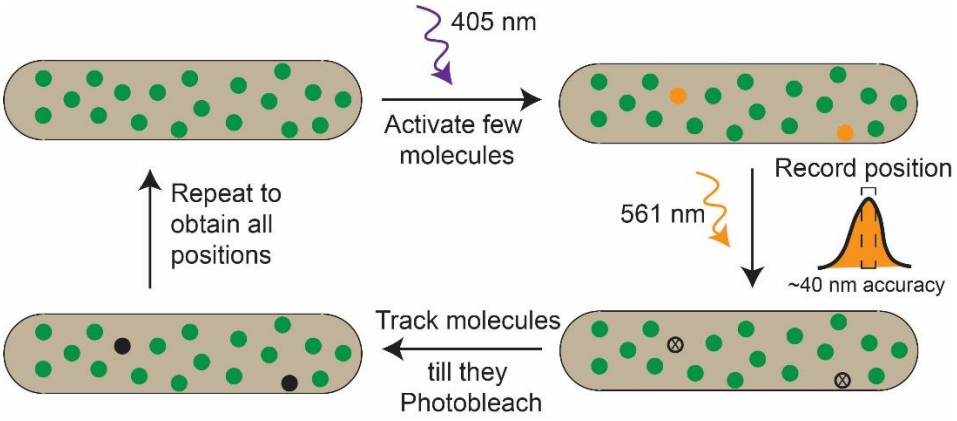

Fig 1.1: Schematic representation of how the PALM technique works. The protein of interest is labeled with a photoactivatable or photoconvertible fluorescent protein. The resolution of this technique depends on the quantum efficiency of the fluorophore.

In our lab, we use Photoactivated Localization Microscopy (PALM) to study the dynamics of our protein of interest in a live cell. As explained above, PALM can give information about the location of individual proteins with ~30-40 nm accuracy. Thus, we can obtain the positional information of multiple protein molecules and monitor how these positions change over time. By using single particle tracking (SPT) we can connect the positions over time and thus we can generate molecular trajectories [9]. A lot of dynamic information can be

extracted from these molecular trajectories – for instance, we can obtain the diffusion coefficient of our protein of interest from the mean squared displacement vs time plot. We can also plot the single step displacement distribution and by fitting the distribution with 2 or 3 populations, the dynamics of different protein states can be obtained. It is also possible to estimate the lifetime of the different diffusive states. In my studies, I have used such methods to study the dynamics of the translation elongation cycle.

The central dogma of biology consists of three different processes – Transcription, Translation and Replication [10]. In Transcription, mRNA is produced from DNA by a protein complex called RNA polymerase [11]. In Translation, proteins are produced from the mRNA by ribosomes, which is a macromolecular complex made up of many different proteins and RNA [11]. In Replication, another set of DNA or a sister chromosome is made as the cell prepares to divide [11]. The translation process itself can be broken down into subprocesses – initiation, elongation and termination. These processes are carried out by many different translation factors which interact with the ribosomes in a specific sequence. During initiation, the start site of the mRNA is identified by the ribosomes and the 50S and the 30S subunits of the ribosome assemble together on the mRNA start site to form the 70S ribosome complex [12]. Elongation is a multistep cycle where the tRNA anticodon is matched with the mRNA codon at the A-site and the corresponding amino acid gets added to the growing peptide chain [13]. The cycle is repeated to make the entire protein. Different translation factors are involved at different steps of the elongation cycle. A schematic of the elongation cycle along with the different proteins involved is shown in Fig 1.2. During termination, after the protein has been made, few different translation factors help the ribosome to identify the stop site and to disassemble from the mRNA and break down into 50S and 30S subunits again.

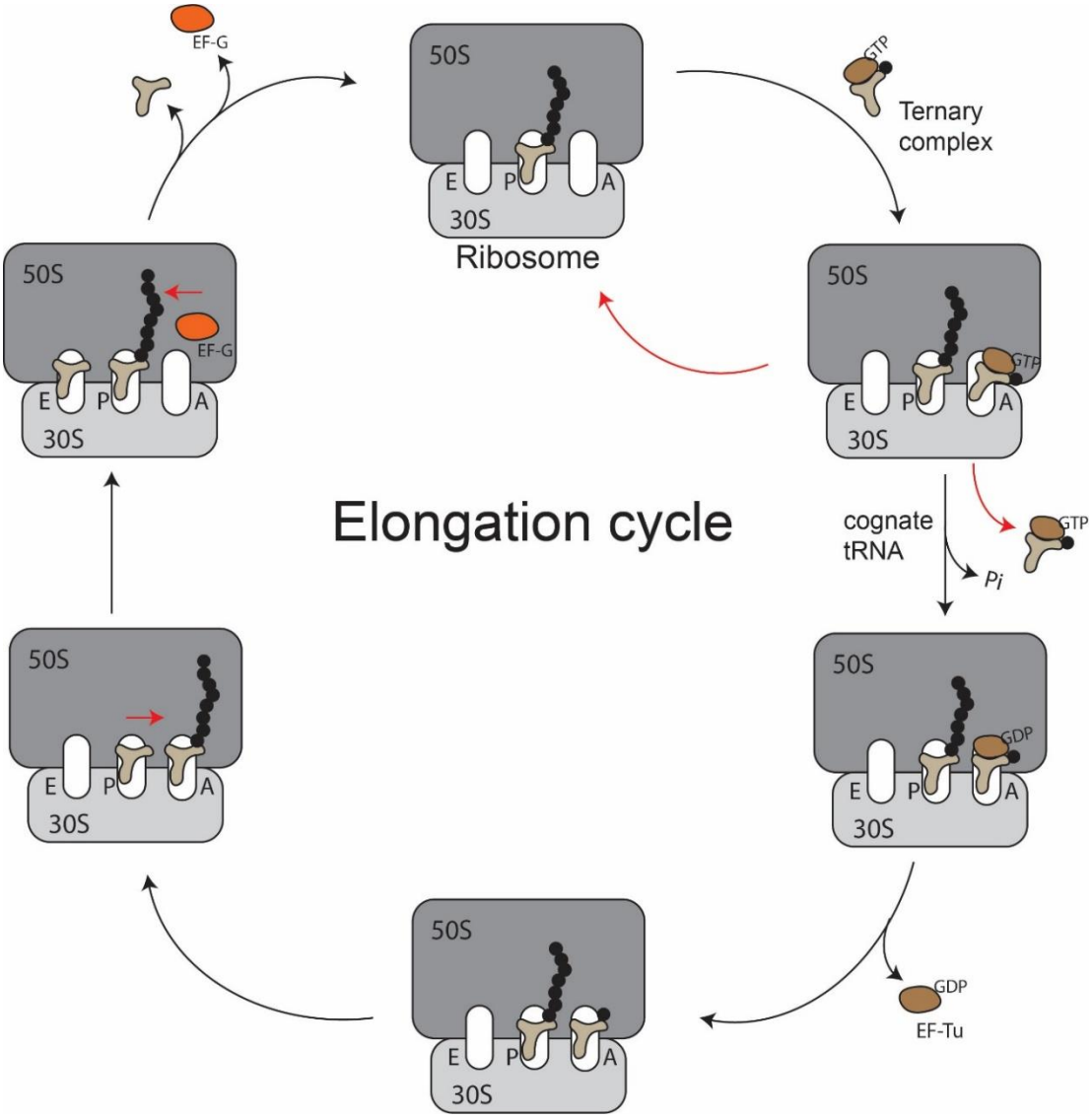

Fig 1.2: Schematic representation of the elongation cycle in the Translation process. The black arrow pathway represents the completion of the cycle, but this pathway is less likely. The red arrow pathway indicates the most likely outcome, when there is a mismatch between the codon of mRNA and the anticodon of tRNA. In this situation, the ternary complex dissociates from the ribosome without undergoing GTP hydrolysis.

The elongation cycle consists of a complex series of events in which an amino acid gets added to the growing peptide chain. In bacteria, the different translation factors (elongation

factors, ‘EF’) involved are – EF-Tu, EF-G, EF-4 and EF-P. EF-Tu helps to bring the aminoacylated tRNA (aatRNA) to the ribosomes for the start of the cycle. The EF-Tu-aatRNA complex along with a GTP molecule is called a ternary complex. Based on the copy numbers of EF-Tu and tRNA, and their *in vitro* binding constant, EF-Tu is majorly present in the ternary complex form [14]. The ternary complex initially binds to a stalk protein on the ribosome called L7/L12 [15, 16]. In *E. coli*, there are 4 such proteins per ribosome. After the ternary complex binds to one of the L7/L12 protein, the aatRNA checks the A-site of the ribosome to see if the codon of the mRNA and the anti-codon of the tRNA matches. If there is a match, then the GTP of the ternary complex gets hydrolyzed to GDP and then EF-Tu leaves. The tRNA can then go into a more favorable conformation at the A-site. The growing peptide chain on the P-site tRNA then gets transferred to the A-site tRNA. In the next step, EF-G binds to the ribosome, also at the L7/L12 stalk. EF-G helps with the translocation of the tRNA and the mRNA from the A to P-site, so that a new tRNA can bind to the ribosome at the A-site again. The deacylated P-site tRNA correspondingly gets transferred to the E-site and leaves the ribosomes thereafter. EF-P can assist with the exit of the E-site tRNA. The entire elongation cycle takes around 50 ms to complete when the bacteria is growing in good/rich growth medium. Thus, every step in the cycle – from finding a match between tRNA anti-codon and the mRNA codon to the translocation of the tRNA to the P-site occurs rapidly. Lots of *in vitro* kinetics study have been done to understand the steps of the elongation cycle [17-20] but these rates are usually much slower than the expected rates in live cells [21, 22]. Also, due to such short or transient interaction, it has not been possible to obtain structural information about the ternary complex-L7/L12 interaction [23]. My primary research has been aimed to understand the dynamics of the

ternary complex – L7/L12 interaction and also the dynamics of EF-Tu overall in the cell. The details of this work are provided in the chapter 2 of this thesis.

Translation is a very efficient process involving numerous proteins working in tandem. It is also an extremely fast process – as mentioned above, the elongation cycle can complete in as less as 50 ms [21, 22], with very low error frequency. Thus, understanding the mechanistic steps involved has been of broad interest from a kinetic standpoint. The rate of the entire translation process has been shown to vary significantly in different growth media – decreasing by a factor of ~2 from rich to minimal media [24, 25]. It has been contested which factor is essentially responsible for the decrease in translation rate. Few possible explanations have been – (i) increase of rare codon usage [26], (ii) decrease in specific tRNA species [27, 28], (iii) increase in (p)ppGpp, which is a competitor of GTP/GDP [29-32], etc. Recently, there has been a theoretical model which states that the diffusion of ternary complex in the crowded cytoplasm determines the rate of the translation process and ultimately the growth rate of the bacteria [24, 25, 33]. The model further discriminates between growth media based on their carbon source and osmolality, stating – there will be a decrease in effective ternary complex concentration in medium with poorer carbon source and there will be a decrease in ternary complex diffusion in medium with higher osmolality because of higher cytoplasmic crowding. These effects will lead to a decrease in effective tRNA concentration at the ribosome for efficient translation, thus reducing the translation rate. It has been shown that when bacteria are exposed to high osmotic shock, the bacterial cytoplasm can lose most of its water content, increasing the crowding significantly [34]. This has a drastic effect on free protein diffusion. But when the bacterial growth is allowed to reach steady state after the initial shock, the free protein diffusion can go back to initial value [35]. Thus, to understand the dependence of translational rate on growth medium, it is important

to understand experimentally what the effect of the concentration and diffusion of ternary complex on the translation rate in different growth media is. The details of this work [36] are described in the chapter 3 of this thesis.

As mentioned above, translation is an extremely important process for the efficient growth of the cell. Understanding the molecular mechanisms of translation have helped in development of many antibiotics, which can target these steps and thus halt the translation process. There are also many naturally occurring antibiotics, isolated from various organisms, which act as a part of their innate defense mechanism against bacterial attacks. The major issue facing the use of these conventional antibiotics is that the bacteria can quickly gain resistance against them. To overcome this problem a lot of focus has been diverted towards developing and identifying new antibacterial molecules or agents which can target different bacterial processes. One such alternative is antimicrobial peptides (AMPs) [37]. These are short, cationic peptides, mostly found in nature, as a part of the defense mechanism of various organisms. Same organism can even produce different AMPs which targets diverse bacterial species. A common mode of action for most AMPs is to first disrupt the cell membrane of the bacteria which causes cellular contents to leak out. They can also freeze the motion of the cellular content – DNA, ribosomes, etc. which can halt many important processes which depend on diffusive search. A specific class of AMP, called proline rich AMP (Pr-AMP), have been shown to be potent antibacterial drugs without the membrane permeabilizing action [37]. They can enter the cells mainly through a specific membrane transporter –SbmA transporter and most of these AMPs bind to the ribosomes to halt translation [38, 39]. One such AMP is Oncocin112 (Onc112). This is a synthetic peptide modified from the original Oncocin, isolated from milkweed bugs. Cryo-EM studies have shown that Onc112 can bind to the peptide exit channel, and biochemical assays

indicate it halts the elongation cycle [40, 41]. This peptide thus has similarities with some antibiotics, like Chloramphenicol (Cam). I have studied the molecular mechanism of the effect of Onc112 on the elongation cycle and compared its effect with other antibiotics. This led to identification of a previously unknown yet vital step in the ternary complex selection. The details of the study are given in chapter 4 of this chapter.

Apart from few other secondary contributions, these were the main projects which I have worked on. These projects have resulted in the following publications:

1. Mustafi M, Weisshaar JC. Simultaneous binding of multiple EF-Tu copies to translating ribosomes in live *Escherichia coli*. mBio. 2018;9:e02143-17.
2. Mustafi M, Weisshaar JC. Near Saturation of Ribosomal L7/L12 Binding Sites with Ternary Complexes in Slowly Growing *E. coli*. Journal of molecular biology. 2019;431:2343-53.
3. Mustafi M, Zhu Y, Weisshaar JC, Long-term Effects of the Proline-rich Antimicrobial Peptide Oncocin112 on the *E. coli* cytoplasm, 2019, manuscript in preparation.

1.1 References:

[1] Phillip Y, Schreiber G. Formation of protein complexes in crowded environments – From *in vitro* to *in vivo*. FEBS Lett. 2013;587:1046-52.

[2] Abbe E. Beiträge zur Theorie des Mikroskops und der mikroskopischen Wahrnehmung. Archiv für Mikroskopische Anatomie. 1873;9:413-68.

[3] Hell SW, Wichmann J. Breaking the diffraction resolution limit by stimulated emission: stimulated-emission-depletion fluorescence microscopy. Opt Lett. 1994;19:780-2.

[4] Klar TA, Hell SW. Subdiffraction resolution in far-field fluorescence microscopy. Opt Lett. 1999;24:954-6.

[5] Dickson RM, Cubitt AB, Tsien RY, Moerner WE. On/off blinking and switching behaviour of single molecules of green fluorescent protein. Nature. 1997;388:355-8.

[6] Betzig E, Patterson GH, Sougrat R, Lindwasser OW, Olenych S, Bonifacino JS, et al. Imaging intracellular fluorescent proteins at nanometer resolution. Science. 2006;313:1642-5.

[7] Rust MJ, Bates M, Zhuang X. Sub-diffraction-limit imaging by stochastic optical reconstruction microscopy (STORM). Nat Methods. 2006;3:793-5.

[8] Hess ST, Girirajan TPK, Mason MD. Ultra-high resolution imaging by fluorescence photoactivation localization microscopy. Biophys J. 2006;91:4258-72.

[9] Manley S, Gillette JM, Patterson GH, Shroff H, Hess HF, Betzig E, et al. High-density mapping of single-molecule trajectories with photoactivated localization microscopy. Nat Methods. 2008;5:155-7.

[10] Crick FH. On protein synthesis. Symp Soc Exp Biol. 1958;12:138-63.

[11] Nelson DM, Cox MM. Lehninger Principles of Biochemistry. Seventh ed: Macmillan Higher Education; 2017.

[12] Gualerzi CO, Pon CL. Initiation of mRNA translation in prokaryotes. Biochemistry. 1990;29:5881-9.

[13] Voorhees RM, Ramakrishnan V. Structural basis of the translational elongation cycle. Annu Rev Biochem. 2013;82:203-36.

[14] Mustafi M, Weisshaar JC. Simultaneous binding of multiple EF-Tu copies to translating ribosomes in live *Escherichia coli*. mBio. 2018;9:e02143-17.

[15] Traut RR, Dey D, Bochkariov DE, Oleinikov AV, Jokhadze GG, Hamman B, et al. Location and domain structure of *Escherichia coli* ribosomal protein L7/L12: site specific cysteine crosslinking and attachment of fluorescent probes. Biochem Cell Biol. 1995;73:949-58.

[16] Kothe U, Wieden HJ, Mohr D, Rodnina MV. Interaction of helix D of elongation factor Tu with helices 4 and 5 of protein L7/12 on the ribosome. J Mol Biol. 2004;336:1011-21.

[17] Wohlgemuth I, Pohl C, Mittelstaet J, Konevega AL, Rodnina MV. Evolutionary optimization of speed and accuracy of decoding on the ribosome. Philos Trans R Soc Lond B Biol Sci. 2011;366:2979-86.

[18] Pape T, Wintermeyer W, Rodnina MV. Complete kinetic mechanism of elongation factor Tu-dependent binding of aminoacyl-tRNA to the A site of the *E. coli* ribosome. EMBO J. 1998;17:7490-7.

[19] Blanchard SC, Gonzalez RL, Kim HD, Chu S, Puglisi JD. tRNA selection and kinetic proofreading in translation. Nat Struct Mol Biol. 2004;11:1008-14.

[20] Geggier P, Dave R, Feldman MB, Terry DS, Altman RB, Munro JB, et al. Conformational sampling of aminoacyl-tRNA during selection on the bacterial ribosome. J Mol Biol. 2010;399:576-95.

[21] Dennis PP, Bremer H. Differential rate of ribosomal protein synthesis in *Escherichia coli* B/r. J Mol Biol. 1974;84:407-22.

[22] Young R, Bremer H. Polypeptide-chain-elongation rate in *Escherichia coli* B/r as a function of growth rate. Biochem J. 1976;160:185.

[23] Schmeing TM, Voorhees RM, Kelley AC, Gao Y-G, Murphy FV, Weir JR, et al. The Crystal Structure of the Ribosome Bound to EF-Tu and Aminoacyl-tRNA. Science. 2009;326:688.

[24] Dai X, Zhu M, Warren M, Balakrishnan R, Patsalo V, Okano H, et al. Reduction of translating ribosomes enables *Escherichia coli* to maintain elongation rates during slow growth. Nat Microbiol. 2016;2:16231.

[25] Dai X, Zhu M, Warren M, Balakrishnan R, Okano H, Williamson JR, et al. Slowdown of translational elongation in *Escherichia coli* under hyperosmotic stress. mBio. 2018;9:e02375-17.

[26] Rosenblum G, Chen C, Kaur J, Cui X, Zhang H, Asahara H, et al. Quantifying elongation rhythm during full-length protein synthesis. J Am Chem Soc. 2013;135:11322-9.

[27] Li SH, Li Z, Park JO, King CG, Rabinowitz JD, Wingreen NS, et al. *Escherichia coli* translation strategies differ across carbon, nitrogen and phosphorus limitation conditions. Nat Microbiol. 2018;3:939-47.

[28] Zhang G, Fedyunin I, Miekley O, Valleriani A, Moura A, Ignatova Z. Global and local depletion of ternary complex limits translational elongation. Nucleic Acids Res. 2010;38:4778-87.

[29] Kanjee U, Ogata K, Houry WA. Direct binding targets of the stringent response alarmone (p)ppGpp. Mol Microbiol. 2012;85:1029-43.

[30] Harshman RB, Yamazaki H. MS I accumulation induced by sodium chloride. Biochemistry. 1972;11:615-8.

[31] Braeken K, Moris M, Daniels R, Vanderleyden J, Michiels J. New horizons for (p)ppGpp in bacterial and plant physiology. Trends Microbiol. 2006;14:45-54.

[32] Shimizu K. Regulation systems of bacteria such as *Escherichia coli* in response to nutrient limitation and environmental stresses. Metabolites. 2013;4:1-35.

[33] Klumpp S, Scott M, Pedersen S, Hwa T. Molecular crowding limits translation and cell growth. Proc Natl Acad Sci U S A. 2013;110:16754-9.

[34] Konopka MC, Shkel IA, Cayley S, Record MT, Weisshaar JC. Crowding and confinement effects on protein diffusion in vivo. J Bacteriol. 2006;188:6115-23.

[35] Konopka MC, Sochacki KA, Bratton BP, Shkel IA, Record MT, Weisshaar JC. Cytoplasmic protein mobility in osmotically stressed *Escherichia coli*. J Bacteriol. 2009;191:231-7.

[36] Mustafi M, Weisshaar JC. Near Saturation of Ribosomal L7/L12 Binding Sites with Ternary Complexes in Slowly Growing *E. coli*. Journal of molecular biology. 2019;431:2343-53.

[37] Antimicrobial Peptides - 2019

Basics for Clinical Application: Springer; 2019.

[38] Graf M, Mardirossian M, Nguyen F, Seefeldt AC, Guichard G, Scocchi M, et al. Proline-rich antimicrobial peptides targeting protein synthesis. Nat Prod Rep. 2017;34:702-11.

[39] Graf M, Wilson DN. Intracellular Antimicrobial Peptides Targeting the Protein Synthesis Machinery. Adv Exp Med Biol. 2019;1117:73-89.

[40] Roy RN, Lomakin IB, Gagnon MG, Steitz TA. The mechanism of inhibition of protein synthesis by the proline-rich peptide oncocin. Nat Struct Mol Biol. 2015;22:466-9.

[41] Seefeldt AC, Nguyen F, Antunes S, Perebaskine N, Graf M, Arenz S, et al. The proline-rich antimicrobial peptide Onc112 inhibits translation by blocking and destabilizing the initiation complex. Nat Struct Mol Biol. 2015;22:470-5.

Chapter 2:

Simultaneous Binding of Multiple EF-Tu Copies to Translating Ribosomes in Live *Escherichia coli*

Reproduced verbatim from:

Mustafi M, Weisshaar JC. Simultaneous binding of multiple EF-Tu copies to translating ribosomes in live *Escherichia coli*. mBio. 2018;9:e02143-17.

2.1 Abstract

In bacteria, elongation factor Tu is a translational co-factor that forms ternary complexes with aminoacyl-tRNA and GTP. Binding of a ternary complex to one of four flexible L7/L12 units on the ribosome tethers a charged tRNA in close proximity to the ribosomal A site. Two sequential tests for a match between the aa-tRNA anticodon and the current mRNA codon then follow. Because one elongation cycle can occur in as little as 50 ms and the vast majority of aa-tRNA copies are not cognate with the current mRNA codon, this testing must occur rapidly. We present a single-molecule localization and tracking study of fluorescently labeled EF-Tu in live *E. coli*. Imaging at 2 ms/frame distinguishes 60% slowly diffusing EF-Tu copies (assigned as transiently bound to translating ribosome) from 40% rapidly diffusing copies (assigned as a mixture of free ternary complexes and free EF-Tu). Combining these percentages with copy number estimates, we infer that the four L7/L12 sites are essentially saturated with ternary complexes *in vivo*. The results corroborate an earlier inference that all four sites can simultaneously tether ternary complexes near the A site, creating a high local concentration that may greatly enhance the rate of testing of aa-tRNAs. Our data and a combinatorial argument both suggest that the initial recognition test for a codon–anticodon match occurs in less than 1–2 ms per aa-tRNA copy. The results refute a recent study of tRNA diffusion in *E. coli* that inferred that aa-tRNAs arrive at the ribosomal A site as bare monomers, not as ternary complexes.

2.2 Importance

Ribosomes catalyze translation of the mRNA codon sequence into the corresponding sequence of amino acids within the nascent polypeptide chain. Polypeptide elongation can be as fast as 50 ms per added amino acid. Each amino acid arrives at the ribosome as a ternary complex comprising an aminoacyl tRNA, an elongation factor called EF-Tu, and GTP. There are 43 different aa-tRNAs in use, only one of which typically matches the current mRNA codon. Thus ternary complexes must be tested very rapidly. Here we use fluorescence-based single-molecule methods that locate and track single EF-Tu copies in *E. coli*. Fast and slow diffusive behavior determines the fraction of EF-Tu copies that are ribosome-bound. We infer simultaneous tethering of ~4 ternary complexes to the ribosome, which may facilitate rapid initial testing for codon matching on a timescale of less than 1–2 ms per aa-tRNA.

2.3 Introduction

In protein synthesis, the elongation cycle comprises an elaborate sequence of steps (1, 2). After an aminoacyl-tRNA (aa-tRNA) binds to the ribosome, it is tested for a match between its anticodon and the current mRNA codon. When a cognate aa-tRNA is found, peptide bond formation occurs and the tRNAs and mRNA translocate through the ribosome, enabling the cycle to begin again. In bacteria, the codon recognition step is catalyzed by elongation factor Tu (EF-Tu), a GTPase. Its eukaryotic homologue is called eEF-1A (3). The translocation step is catalyzed by a second GTPase called elongation factor G (EF-G) (2).

In the standard mechanistic model of *E. coli* translation (1, 2), aa-tRNA binds to the ribosome as a ternary complex: aa-tRNA–EF-Tu(GTP). The ternary complex is recruited to the ribosome by binding to one of four L7/L12 sites that protrude from the stalk of the ribosome, as shown schematically in Fig. 2.1A (4). L7 is identical to L12 except for an acylated N-terminus. Biochemical evidence indicates that the binding interface juxtaposes the C-terminal domain of L7/L12 Domain 1 of EF-Tu (5, 6). The ribosomal stalk thus tethers aa-tRNA copies in close proximity to the ribosomal A site, where they can be tested for a codon match. In good growth conditions, *E. coli* can carry out elongation at a rate of ~17-20 aa/s, implying that the mean time to carry out a complete elongation cycle can be as short as 50 ms (7, 8). Since the vast majority of aa-tRNA copies carry a non-cognate or near-cognate anticodon that does not match the current mRNA codon (9), testing of individual aa-tRNAs for a codon match must be very rapid. A recent global theory of bacterial metabolism suggested that the diffusive search of EF-Tu for its ribosomal binding site is the step limiting the overall growth rate (10).

The sequence of events leading from the initial binding step to codon recognition and peptide bond formation has been dissected in remarkable detail by a groundbreaking series of

rapid-mixing kinetics experiments carried out *in vitro* and summarized in Refs. (1) and (9). Single-molecule studies *in vitro* have helped to further refine the detailed sequence of mechanistic steps (11, 12). The inferred mechanism includes two consecutive stages of codon discrimination: initial selection and subsequent proofreading, with multiple intermediate states delineated for both stages (1). The overall mechanism enables cognate aa-tRNAs to proceed rapidly to accommodation in the A site, while rapidly rejecting non-cognate and near-cognate aa-tRNAs. Most recently, a detailed set of *in vitro* transition rates has been optimally scaled to form a theoretical set of *in vivo*, codon-specific transition rates that yield the correct overall translation rate in exponentially growing *E. coli* (9). These optimized *in vivo* transition rates were then used to predict codon-dependent translation speeds, codon-specific translation dynamics, and missense error frequencies. The good agreement of the model predictions with experiment serves to validate the new method for transforming detailed *in vitro* rates into useful *in vivo* rates.

The *E. coli* ribosomal stalk (schematic in Fig. 2.1A) comprises the L11 protein which binds to rRNA and forms the base of the stalk, the protruding L10 protein which binds to L11 via a flexible connection, and four L7/L12 copies which bind to L10 as a pair of dimers (4). Each L7/L12 has three domains. The N-terminus binds to L10, and a flexible hinge connects the N-terminus to the C-terminus. A compelling body of biochemical evidence detailed in Ref. (4) and summarized below indicates that the C-terminal domain of L7/L12 binds to helix D of EF-Tu within the ternary complex. The only structural evidence for L7/L12 binding to EF-Tu comes from a cryo-EM reconstruction at 1.8 nm resolution (13). The structure suggests a bridge between Domain 1 of EF-Tu (the G domain) and the L7/L12 stalk, in agreement with inferences from the biochemical data. A comprehensive model of ribosomal stalk structure and function suggested that the four highly mobile L7/L12 C-terminal domains serve to efficiently recruit

ternary complexes to the ribosome and to help stabilize the active GTPase conformation of EF-Tu (4). However, there is no crystal structure that reveals the molecular-level details of the initial binding step of the ternary complex to the ribosome. In all high resolution structural studies to date, the L7/L12 stalk is highly mobile and does not yield discernible electron density (2).

We and others have used live-cell, single-molecule fluorescence methods to study the spatial distribution and diffusive properties of a variety of proteins in *E. coli* (14, 15). In a typical experiment, the protein of interest is expressed from the chromosome as a fusion to a photoconvertible fluorescent protein. A weak laser at 405 nm switches the absorption and emission wavelengths of literally one or two protein copies per cell. A more powerful probe laser then enables selective excitation, localization, and tracking of the sparse photoswitched copies until they photobleach. For high copy number proteins, this enables the acquisition of thousands of single-molecule trajectories from each cell over tens of seconds. The spatial localization accuracy is typically $\sigma \sim 40–80$ nm, and the temporal resolution can be in the low-millisecond range (16). In favorable cases, the diffusive properties of a single copy can be related to its biochemical function at a given moment in time.

Here we present a single-molecule localization and tracking study of EF-Tu in *E. coli*. EF-Tu is labeled at the C-terminus with the 26 kDa (17) photoconvertible fluorescent protein mEos2 (18). Measurement of a large number of short-lived diffusive tracks at 2 ms/frame enables an approximate decomposition of the EF-Tu population into two sub-states. We call these states *slow* (assigned as copies transiently bound to translating, 70S ribosomes, including polysomes) and *fast* (copies not bound to ribosomes, presumably mostly EF-Tu within free ternary complexes). Accordingly, the slow copies (~60%) concentrate in the three ribosome-rich regions where most translation occurs, outside the nucleoids (15, 19).

Combining the new diffusion data with copy number estimates for ribosomes and EF-Tu indicates that the four L7/L12 sites are essentially saturated with EF-Tu copies *in vivo*. This new result corroborates the earlier inference from *in vitro* kinetics measurements that all four *E. coli* L7/L12 sites are actively engaged in recruiting ternary complexes to the ribosome (4). The timescale of binding events indicates that free ternary complexes find translating ribosomes extremely efficiently, in good quantitative agreement with the recent model of *in vivo* kinetics (9). Evidently aa-tRNA copies are tested for a match to the current codon on a timescale of 1–2 ms or less, in further agreement with the *in vivo* model. Simultaneous binding of four ternary complexes to each translating ribosome may greatly enhance the rate of testing (4). Finally, the results refute the main conclusion from a recent single-molecule tracking study of tRNA diffusion in *E. coli* (20). That work inferred that most aa-tRNAs are monomeric and freely diffusing, arriving at the ribosomal A site as bare aa-tRNAs, not as ternary complexes.

2.4 Results

2.4.1 Comparison of axial spatial distributions of EF-Tu and ribosomes

Essentially identical copies of EF-Tu are expressed by two genes in *E. coli*: *tufA* and *tufB* (21). We have fused the gene coding for the photoconvertible fluorescent protein mEos2 to the C-terminus of both endogenous genes within the chromosome in the *E. coli* strain NCM3722 and then moved the fusions to the VH1000 background strain for further study (Table A2.1A). Labeling of all copies of EF-Tu with mEos2 ensures that there is no competition with unlabeled copies. Domain 3 of EF-Tu binds to tRNA and includes the C-terminus, but mEos2 is appended on the face opposite to the tRNA binding site. In “EZ rich, defined medium” (EZRDM), the doubling time at 30°C of the modified strain expressing EF-Tu–mEos2 from the chromosome is 60 ± 3 min, compared with 45 ± 2 min (19) for the unlabeled VH1000 background strain (Fig.

A2.8). Evidently the labeling does not greatly affect the functionality of EF-Tu, an essential protein.

Our goal is to use diffusive properties to distinguish ribosome-bound EF-Tu from EF-Tu not bound to ribosomes. The mass of bare EF-Tu–mEos2 is 69 kDa, 26 kDa of which is due to mEos2. The mass of a typical labeled ternary complex including mEos2 (aa-tRNA–EF-Tu(GTP)–mEos2) is ~95 kDa. We would expect the diffusion coefficient of free ternary complexes (not bound to ribosomes) and of free, bare EF-Tu in the cytoplasm to be similarly fast, perhaps 4–8 μm^2-s^{-1} (22, 23). Short diffusive trajectories with significant localization error will not be able to distinguish free ternary complexes from bare EF-Tu; we use "fast EF-Tu" to denote a composite of these two species. Below we will argue that a large majority of these fast EF-Tu copies are bound within ternary complexes. In contrast, the ribosome mass is ~2.5 MDa (24, 25) and translating 70S ribosomes in exponentially growing *E. coli* exist primarily as polysomes (15, 19, 26). The mean 70S ribosome diffusion coefficient under these fast imaging conditions is ~0.1 μm^2-s^{-1} (Appendix). EF-Tu copies that are bound to translating 70S ribosomes should diffuse similarly slowly.

It was previously shown that in our moderately fast exponential growth conditions, *E. coli* exhibits strong segregation of the two major nucleoid lobes from the 70S ribosomes (19). The projected axial distribution of ribosomes within the cytoplasm typically has three peaks, with the two nucleoid lobes interleaving three "ribosome-rich regions". In contrast, free 30S and 50S subunits readily penetrate the nucleoid regions (15, 19, 27). Segregation of 70S ribosomes from the chromosomal DNA may serve to enhance the efficiency of recycling of 30S and 50S subunits and also the efficiency of the search for transcription initiation sites by RNA polymerase. The slowly diffusing EF-Tu ternary complexes bound to 70S ribosomes should also exhibit a three-

peaked axial distribution, while rapidly diffusing, free EF-Tu should be distributed more uniformly.

We imaged EF-Tu–mEos2 molecules in cells by photoactivating and locating fluorophores, connecting locations over multiple frames to form trajectories of individual molecules (28). Details are provided in Methods and in Appendix. To enable efficient superresolution imaging of rapidly diffusing molecules, the exposure time was 2 ms/frame with continuous laser illumination. The number of switched-on copies per cell was limited to 0-2 molecules per frame to avoid spatial overlap of the single-molecule features.

Several example trajectories from a single cell are shown in Fig. 2.1B. In constructing axial spatial distributions that combine data from many cells, we included only cells which were 4-5 μm in tip-to-tip length to minimize blurring of features. From 201 such cells, we obtained 4221 EF-Tu–mEos2 trajectories which lasted at least 6 steps (7 camera frames, or 12 ms total duration). All localizations were included in the spatial distributions. The axial and radial cell dimensions were normalized and the relative molecular positions were pixelated and plotted to obtain a two-dimensional heat map of the EF-Tu spatial distribution (Fig. 2.1C, top). The map shows that EF-Tu is distributed over the entire cytoplasm, but the distribution is not homogeneous. For comparison, in Fig. 2.1C (bottom) we show the heat map for ribosomes with the 30S subunit labeled by the endogenously expressed S2-mEos2 protein at the C-terminus as before (19) and imaged under the same conditions used for EF-Tu. Again, trajectories of 6 steps or longer in cells of 4-5 μm length were included. As shown qualitatively by the heat maps of Fig. 2.1C and quantitatively in the projected axial distributions of Fig. 2.1D, ribosomes exhibit substantially greater segregation from the nucleoids than EF-Tu. The total EF-Tu distribution does exhibit three peaks, but they are less sharply defined. This

indicates that at a given moment, only a fraction of EF-Tu–mEos2 copies are associated with 70S ribosomes.

2.4.2 Diffusion of EF-Tu

For the diffusion study, we used 1912 trajectories of 6-step duration or longer, obtained from 118 different cells. Longer trajectories were truncated at 6 steps. The exposure time was 2 ms/frame. The mean diffusion coefficient D_{mean} can be estimated from a plot of the two-dimensional mean-square displacement vs lag time, MSD(τ), using the slope of the first two data points. This provides a population-weighted average of diffusion coefficients over the different states of the molecule. The MSD slope accounts for localization error, but does not account for confinement effects. In Fig. 2.2 we compare MSD plots for wild-type (WT) EF-Tu and ribosomes. The mean diffusion coefficients are 2.02 ± 0.19 μm^2/s for EF-Tu and 0.4 ± 0.1 μm^2-s^{-1} for ribosomes. The mean value for EF-Tu is consistent with the existence of at least two diffusive states, a fast, rapidly diffusing EF-Tu state and a slow, ribosome-bound state. The intercept of the MSD plot provides an estimate of the mean localization accuracy σ ~ 60 nm (29).

In order to quantify the fraction of ribosome-bound EF-Tu copies, the same truncated trajectories were divided into individual steps with Δt = 2 ms between camera frames. This attempts to isolate short time intervals during which EF-Tu remains in one particular diffusive state (16). The resulting distribution of experimental single-step displacements, $P_{EF\text{-}Tu}(r)$, is shown for 11,472 individual steps in Fig. 2.3A. We analyze such $P(r)$ distributions by comparison with a large number of simulated random walk trajectories that incorporate dynamic localization error σ and confinement within a spherocylinder that mimics the dimensions of an *E.*

coli cell. Details are provided in Appendix. For each chosen model diffusion coefficient D and measurement error σ, the simulations provide a numerical function we call $P_{model}(r;D)$. We attempt to fit the experimental distribution $P(r)$ using least-squares to a single population or to a weighted average of two static populations. The goodness of each fit was judged by the reduced chi-square statistic χ_v^2, which should be approximately one for an appropriate model function (30). For a one-state model the only fitting parameter is D. For unconstrained models including two static (non-exchanging) states, the fitting function is the linear combination $P_{model}(r) = f_{slow}P(r;D_{slow}) + (1 - f_{slow})P(r;D_{fast})$. Here the three fitting parameters are D_{fast}, D_{slow}, and the fractional population f_{slow}, which in turn fixes $f_{fast} = (1 - f_{slow})$.

One-component fits to the $P_{EF\text{-}Tu}(r)$ were poor, with minimum $\chi_v^2 = 9.7$ (Fig. A2.1B). Fits to two non-exchanging diffusive states were substantially better. The best value of χ_v^2 was 1.24, obtained using model parameters $f_{slow} = 0.60 \pm 0.05$, $D_{slow} = 1.0 \pm 0.2$ μm^2/s, $f_{fast} = 0.40 \pm 0.05$, and $D_{fast} = 4.9 \pm 1.2$ μm^2/s (Table 2.1). The best-fit two-state model result is plotted in Fig. 2.3A and resolved into the two separate contributions. The parameter uncertainties are based on the range of parameters that return reduced chi-square values within 0.5 units of the best value, as detailed in Appendix. Parameter sets with χ_v^2 values still larger were judged by eye to be qualitatively poor. The best two-component constrained fit to $P_{EF\text{-}Tu}(r)$ with D_{slow} fixed at 0.1 μm^2-s^{-1} (to match the slow, 70S component of the ribosome diffusion data) has $\chi_v^2 = 2.5$ (Fig. A2.1A), much worse than the global best-fit value of 1.24. Our constrained search for three-component fits did not reduce χ_v^2 significantly (Appendix, Fig. A2.1C).

While the static two-state model fits the data reasonably well (Fig. 2.3A), if it were completely adequate then a value of χ_v^2 as large as 1.24 would be statistically highly unlikely ($p \sim 0.01$). Here we must recognize that the true diffusive behavior of EF-Tu is surely a

composite of *many* diffusive states: free EF-Tu and free ternary complexes (to which the fast diffusion is assigned), and EF-Tu bound to 70S ribosomes and polysomes of variable length (to which the slow diffusion is assigned). Under our fast imaging conditions, the distribution of measured step lengths for the slower population is dominated by the measurement error, not by true displacement of the tracked species. There is also the likelihood of transitions between these states on the 2-ms timescale of the single-step displacement measurements; see below.

What is robust in the fitting results is the fraction of rapidly diffusing copies having $D_{fast} \sim 4.9\ \mu m^2/s$. The best-fit fraction f_{fast} is 0.40 ± 0.05 in the two-state modeling and 0.35 ± 0.05 in the three-state modeling. Such a fraction of fast molecules is evidently necessary to fit the long tail on the distribution $P_{EF\text{-}Tu}(r)$ (Figs. 2.3A and A2.1C), and that is the part of the distribution least perturbed by measurement error. In addition, the value $D_{fast} \sim 4.9\ \mu m^2/s$ will be confirmed below in studies of cells treated with the drug rifampicin. The main conclusion of this work, that ~60% of EF-Tu copies are *not* in the rapidly diffusing states over the 2-ms frame time of the measurements, appears quite robust. In what follows, we proceed with further analysis of the two-state model results under the assumption that they represent the partitioning into ribosome-bound and unbound EF-Tu copies fairly accurately. Separate axial distributions for slow and fast steps (below) will further corroborate the assignments of the fast and slow components.

The best-fit value $D_{slow} = 1.0 \pm 0.2\ \mu m^2\text{-}s^{-1}$ for EF-Tu is ten times larger than the estimated diffusion coefficient of the slow component of the ribosome distribution $P_{ribo}(r)$, which has a diffusion coefficient of $0.1 \pm 0.1\ \mu m^2\text{-}s^{-1}$ (Fig. A2.2 and Table 2.1). Importantly, fits to two-state model functions with the slow diffusion constrained to match that of the 70S ribosomes were much worse (Fig A2.1A). This suggests to us that the slow component of EF-Tu diffusion is

itself a composite state comprising two sub-states that exchange with each other during the 2-ms camera frame: EF-Tu bound to 70S ribosomes (with mean lifetime τ_{on}) and free EF-Tu or free ternary complexes (with mean lifetime τ_{off}) sequestered in the ribosome-rich regions and diffusing freely between ribosome binding events. Here τ_{on} is the mean time a ternary complex spends bound to a 70S ribosome and τ_{off} is the mean time a ternary complex spends searching for a ribosomal binding site, with both times referring to ternary complexes within the ribosome-rich regions.

If this is essentially correct, then we can infer that $(\tau_{on} + \tau_{off}) \leq 2$ ms. If we assume that $D_{fast} = 4.9\ \mu m^2\text{-}s^{-1}$ applies to the free EF-Tu and ternary complex components in the ribosome-rich regions, then the sequestered EF-Tu copies are spending ~80% of the time actually bound to ribosomes and ~20% of the time in transit between ribosome-binding sites. Those are the population fractions that yield the correct weighted average diffusion coefficient: $D_{slow} = 1.0\ \mu m^2\text{-}s^{-1} = 0.2 \times 4.9\ \mu m^2\text{-}s^{-1} + 0.8 \times 0.1\ \mu m^2\text{-}s^{-1}$. The corresponding lifetime ratio is $\tau_{on}/\tau_{off} \sim 4$. According to this interpretation, within the ribosome-rich region EF-Tu copies are exchanging between the ribosome-bound and free EF-Tu states so fast that our 2-ms camera frames can only report on the average diffusive behavior of the bound and free states. As discussed below, such short on- and off-times make good biochemical sense.

To test the assignment of the slow population to ribosome-bound EF-Tu, we plotted separate axial location distributions for the slowest (step length $r < 0.1$ μm) and fastest ($r > 0.2$ μm) components of $P_{EF\text{-}Tu}(r)$. The arrows in Fig. 2.3A mark these cutoffs. According to the best two-state model, the slow cutoff includes steps of which ~80% belong to the slow population, while the fast cutoff includes steps of which ~90% belong to the fast population. The location of each step was assigned as the midpoint of the first and second locations, and the axial coordinates

were scaled and normalized as before. The results are shown in Fig. 2.3B in comparison with the total ribosome axial distribution. The three-peaked distribution of slow steps extends into the endcaps as the ribosomes do. The distribution of fast steps avoids the ribosome-rich endcaps and is perhaps mildly concentrated in the nucleoid regions. These results are consistent with the slow population preferentially residing within the ribosome-rich regions due to transient binding to 70S and the fast population preferentially residing within the nucleoids.

2.4.3 Effects of Rifampicin

To better characterize the diffusive properties of free EF-Tu/ternary complex, we treated exponentially growing cells with 250 μg/mL of the antibiotic rifampicin (Rif) for three hours prior to plating and imaging of EF-Tu–mEos2. Rif halts transcription and thus effectively stops mRNA production (31, 32). On a timescale of 10 min, the existing mRNA is degraded. Lacking mRNA to translate, the 70S polysomes dissociate into free 50S and 30S subunits. We used 792 trajectories which lasted at least 6 steps or longer from 58 cells to plot the spatial distribution of EF-Tu under Rif treatment. The selected cell lengths varied from 3-4 μm; after Rif treatment, the distribution of cell lengths shifts towards smaller values. The heat map shows a fairly uniform distribution of EF-Tu along the long axis of the cell, but with the endcaps partially excluded (Fig. A2.4A). As shown earlier (31), under Rif treatment the nucleoids expand to fill the cytoplasmic volume fairly homogeneously. The 30S and 50S ribosomal subunits mix with the expanded DNA; they also occupy the cytoplasmic volume fairly uniformly. The EF-Tu distribution is similar.

We used 1181 trajectories from 78 cells for the EF-Tu diffusive state analysis after Rif treatment. All trajectories of 6 steps or longer were truncated at the sixth step as before. The mean EF-Tu diffusion coefficient obtained from the MSD(τ) plot increases to 3.5 ± 0.4 $\mu m^2/s$

(Fig. 2.2). This is larger than that of EF-Tu in normally growing cells, 2.02 ± 0.09 μm^2/s. Accordingly, under Rif treatment the two-state analysis of $P_{EF\text{-}Tu}(r)$ (Fig. A2.4C) finds f_{slow} = 0.35 ± 0.05 of EF-Tu that moves with D_{slow} = 1.5 ± 0.5 μm^2/s, slightly larger than the value of D_{slow} = 1.0 ± 0.2 μm^2-s^{-1} in untreated cells (Fig. 2.3A). A larger fraction f_{fast} = 0.65 ± 0.05 of EF-Tu moves with the same D_{fast} = 4.9 ± 1.5 μm^2/s found for untreated cells. The results after Rif treatment suggest the possibility of some residual binding of EF-Tu/ternary complex to ribosomal subunits, perhaps to the same L7/L12 binding sites on 50S. This is only a suggestion, but it is supported by the results for a mutated variant of EF-Tu presented next.

2.4.4 EF-Tu L148A mutant

Rodnina and co-workers (5) studied the effects of point mutations within the C-terminus of L7/L12 and within helix D of EF-Tu on the kinetics of initial binding of ternary complex to ribosomes. The mutation sites were chosen by analogy to the well characterized structure of the EF-Ts/EF-Tu complex. The mutations that caused a substantial decrease in the association rate constant k_1 were used to model the important contacts in the complex between L7/L12 and EF-Tu. The particular mutation L148A in EF-Tu decreased k_1 by a factor of 5. To probe this interaction *in vivo*, we engineered a plasmid containing the same L148A mutation to EF-Tu appended to a C-terminal mEos2 label (Table A2.1). The mutated protein was expressed in the same background strain VH1000 along with WT protein expressed normally from the chromosome to enable normal cell growth.

We obtained 1160 trajectories of 6 steps or longer from 153 cells to study the diffusion of EF-Tu^{L148A}–mEos2. The mean diffusion coefficient from the MSD plot is 3.1 ± 0.3 μm^2-s^{-1} (Fig. 2.2). This is larger than the mean value 2.02 ± 0.19 μm^2/s for normal EF-Tu–mEos2, consistent with a smaller degree of binding of the mutated protein to ribosomes. Accordingly, the

two-component $P(r)$ analysis of mutant protein diffusion finds $f_{slow} = 0.30 \pm 0.05$ (two-fold smaller than for the normal protein) with $D_{slow} = 1.2 \pm 0.5$ μm^2/s and $f_{fast} = 0.70 \pm 0.05$ with $D_{fast} = 4.5 \pm 1.0$ μm^2/s (Fig. 2.4C). The location heat map and the axial spatial distribution for the EF-Tu^{L148A} mutant (Fig. 2.4A, B) show that the mutated protein is fairly uniformly distributed throughout the cell, with only a hint of three peaks. These results indicate substantially less binding of the EF-Tu^{L148A} mutant to ribosomal sites, in qualitatively agreement with the mutation studies *in vitro* (5). The agreement helps to corroborate our underlying assumption that ternary complexes are binding to L7/L12 ribosomal subunits *in vivo*; see Discussion for a summary of additional biochemical evidence.

To control for possible effects of overexpression of the L148A mutant from the plasmid, we constructed an analogous plasmid that expresses WT EF-Tu–mEos2 and incorporated it into the same VH1000 background strain. The spatial distribution and diffusive properties of the EF-Tu–mEos2 copies expressed from the plasmid were qualitatively similar to those of EF-Tu-mEos2 expressed from the chromosome (Fig. A2.5).

To test for possible binding of the mutant form EF-Tu^{L148A} to free 50S ribosomal subunits, we obtained 993 trajectories of 6 steps or longer from 83 cells after the 3-hr Rif treatment. The slope of the MSD plot increases to 5.2 ± 0.4 μm^2-s^{-1} (Fig. 2.2), compared with 3.5 ± 0.4 μm^2/s for WT EF-Tu after Rif. The $P(r)$ distribution is fit qualitatively by a single population with $D = 5.7 \pm 1.0$ μm^2-s^{-1} ($\chi_\nu^2 = 1.5$). The best two-component fit yielded $f_{slow} = 0.10 \pm 0.05$, $D_{slow} = 1.9 \pm 1.2$ μm^2-s^{-1}, $f_{fast} = 0.90 \pm 0.05$, $D_{fast} = 5.6 \pm 1.2$ μm^2-s^{-1}, and $\chi_\nu^2 = 1.2$. The analysis indicates that after Rif treatment, most EF-Tu^{L148A} is diffusing essentially freely, perhaps primarily as ternary complexes. Evidently the mutant protein exhibits little or no binding to free 30S or 50S subunits.

2.4.5 Numerical estimates and comparisons with theory

The present results can be combined with literature estimates for relative copy numbers of ribosomes, EF-Tu, EF-G, tRNAs, and aa-tRNA synthetases to provide semi-quantitative insight into the partitioning of EF-Tu and tRNA across functional states and the time-averaged stoichiometry of the species bound to a translating ribosome. Under the same growth conditions used here (30°C in EZRDM), we previously estimated ~50,000 30S ribosomal subunits per cell, some 80% of which (~40,000 copies) are engaged as translating, 70S ribosomes (15). Mean copy number estimates for EF-Tu, total tRNA, EF-G, and total aa-tRNA synthetase (Table A2.2) were derived from the ribosome copy number and from literature values of the ratio of each species' copy number to that of ribosomes. It was not possible to match strains, growth conditions, growth rate, and temperature, so we chose to match the growth rate (~1 doubling/hr). We hope these rough estimates will help constrain future models of overall *E. coli* translation rates. Their biological significance will be discussed further below. Details of the calculations and underlying assumptions are provided in Appendix; here we summarize the estimates. The primary assumption is that EF-Tu binds to translating ribosomes via contact with the C-terminus of L7/L12. This is justified in the Discussion.

The time-averaged stoichiometry of EF-Tu and tRNA binding to a translating 70S ribosome can be estimated from the fraction of EF-Tu copies bound to ribosomes combined with copy number estimates from other studies. There are 61 different codons and 43 different aa-tRNA types (43 different ternary complexes) used by *E. coli* (9). Forty-eight codons match only one type of ternary complex, 12 match two types, and one matches three types. This means that the ribosome is usually testing and rejecting non-cognate or near-cognate aa-tRNAs. The A site is

most frequently occupied by an aa-tRNA within its ternary complex, still tethered to L7/L12 (prior to codon selection, GTP hydrolysis, and ejection of EF-Tu) (9).

Under our growth conditions of 30°C in EZRDM, we estimate the following mean copy numbers per cell: ~40,000 translating 70S ribosomes (concentrated in three ribosome-rich regions) (15), ~10,000 free 30S subunits, ~10,000 free 50S subunits, ~350,000 total EF-Tu copies (10, 33), ~350,000 total tRNA copies (34), ~50,000 EF-G copies (which compete with EF-Tu for L7/L12 binding sites) (33), and ~50,000 aa-tRNA synthetases (33). The new data suggest that ~210,000 EF-Tu copies (60%, the "slow" copies) are ternary complexes that occupy the ribosome-rich regions, where they are bound to 70S ribosomes ~80% of the time (~170,000 ribosome-bound ternary complexes plus ~40,000 free ternary complexes). Thus we estimate as many as ~170,000/40,000 = 4 ternary complexes bound to each translating ribosome. This indicates that the four L7/L12 subunits in *E. coli* are essentially saturated with ternary complexes. However, EF-G must also bind to L7/L12 in order to drive translocation on those rare occasions when a cognate aa-tRNA is accommodated in the A site and forms a new peptide bond. In our estimate, we assume the average occupancy of the four L7/L12 units is 3.5 ternary complexes and 0.5 EF-G copies. The remaining ~180,000 EF-Tu copies partition into ~70,000 free ternary complexes plus ~110,000 free (bare) EF-Tu. The overall partitioning of EF-Tu between ternary complexes and free EF-Tu is corroborated by an equilibrium calculation based on the aa-tRNA/EF-Tu binding constant *in vitro* (35).

For partitioning of the ~350,000 total tRNA copies, we estimate that on average each 70S ribosome binds one tRNA at the A site (usually tethered to L7/L12 by a bridging EF-Tu), one in the P-site, one-half tRNA in the E site (an average over "2-1-2" and "2-3-2" models (36, 37)), plus an additional ~2.5 tRNAs bound to the other three L7/L12 sites. Recall that EF-G is

assumed to take up 0.5 L7/L12 binding sites. Thus averaged over time, ~5 tRNAs are bound to each 70S ribosome (~200,000 tRNAs bound to ~40,000 translating ribosomes, comprising ~140,000 tRNA within ternary complexes and ~60,000 tRNA at the P- and E-sites). The remaining ~150,000 tRNA copies not bound to 70S are estimated to partition among three states: ~50,000 copies being recharged by aa-tRNA synthetases, ~100,000 copies within free ternary complexes, and only ~400 free tRNA. These estimates are based in part on an equilibrium calculation using the *in vitro* binding constant of aa-tRNA with EF-Tu (35).

In addition, our new data are in sensible agreement with two rate constants from a model that optimally scaled a detailed set of *in vitro* rate constants to derive a set of theoretical *in vivo* rate constants describing the multi-step process of the elongation cycle (9). Again, details are presented in Appendix. First we use the pseudo-first-order rate τ_{off}^{-1} and the 70S ribosome concentration to estimate a lower limit on the effective bimolecular association rate constant k_1 for binding of a typical non-cognate ternary complex to an L7/L12 subunit of a 70S ribosome within the ribosome-rich regions. The result is $k_1 = \tau_{off}^{-1}/[70S] \geq 4.5 \times 10^7\ M^{-1}s^{-1}$. This is remarkably fast, at least 1/6 of the calculated diffusion-limited rate constant $k_{diff} = 3.2 \times 10^8\ M^{-1}s^{-1}$. As suggested earlier (4), k_1 (which is expressed on a per ribosome basis) may be especially large due to the four L7/L12 binding sites per ribosome and the length and flexibility of the linkages between ribosome and the C-terminal domain of L7/L12. The theoretical *in vivo* estimate for the analogous κ_{on}* (Table 2 of Ref. (9)) at 1.07 doublings/hr and 37°C is $9.4 \times 10^7\ M^{-1}s^{-1}$, twofold larger than our lower limit on k_1.

We can also compute a lower limit on the unimolecular dissociation rate of EF-Tu (usually as part of a ternary complex) from the ribosome, $k_{-1} = \tau_{on}^{-1} \geq 625\ s^{-1}$ at 30°C. The value of k_{-1} is temperature sensitive. If we apply an Arrhenius-based correction factor of 2.1 to our k_{-1} at 30°C

(details in Appendix), the estimated value at 37°C becomes $k_{-1} \geq 1250\ s^{-1}$. This is consistent with the theoretical *in vivo* rate constant for 1.07 doublings/hr at 37°C, $\omega_{off}^* = 1700\ s^{-1}$ (Table 2 of Ref. (9)).

2.4.6 Disagreement with a recent tRNA tracking study

In violation of the standard model of aa-tRNA recruitment, a recent single-tRNA tracking experiment from the Kapanidis lab inferred that a large majority of tRNA copies exist as free tRNA, bound neither to EF-Tu in ternary complexes nor to the aminoacyl-tRNA synthetase (20). They electroporated a small number of tRNA copies fluorescently labeled with Cy5 dye into *E. coli* and tracked the motion of single molecules. A large fraction (70-90%) of the tRNA-Cy5 copies diffused very rapidly (corrected $D_{tRNA} \sim 8\ \mu m^2\text{-}s^{-1}$). These copies were attributed to free tRNA (not bound within ternary complexes). The conclusion was that diffusion of free aa-tRNA, not ternary complexes, must be the primary means of delivery of aa-tRNA to the ribosomal A site. The remarkably large fraction of free tRNA copies was deemed possible based on the assumption that *only two* tRNA copies are bound to each ribosome (one each in the A and P sites). The rationale given for the small estimated fraction of ternary complexes (20) was that EF-Tu can bind to membrane-bound MreB, as evidently occurs in both *B. subtilis* and *E. coli* (38-40). This would remove EF-Tu from the cytoplasm and make it less available for ternary complex formation. However, the EF-Tu copy number is about 100 times larger than that of MreB (33). In addition, we find no evidence in our EF-Tu spatial distribution of significant binding to the cytoplasmic membrane, where MreB resides. In contrast, our numerical estimates based on an average of ~3.5 ternary complexes bound to the four L7/L12 sites indicate ~5 bound tRNA per ribosome. Finally, our equilibrium calculations suggest that only ~1% or less of total tRNA should exist as free tRNA.

One potential weakness of the electroporation method (20) is that the few labeled tRNA copies in each cell must compete with the 350,000 endogenous tRNA copies for aminoacylation, ternary complex formation, and binding and processing by the ribosome. Although the labeled tRNA-Cy5 species was shown to be functional *in vitro*, it is difficult to know how well tRNA-Cy5 copies compete with endogenous copies in each functional step *in vivo.* It seems possible that the synthetase recognizes tRNA–Cy5 poorly, or that aa-tRNA–Cy5 forms ternary complexes poorly *in vivo*, or that these complexes bind 70S ribosomes weakly, or that Cy5 fluorescence is somehow quenched in ternary complexes so that they are not detected.

2.5 Discussion

2.5.1 Rapid testing of aa-tRNA copies for a codon-anticodon match

In rapidly growing *E. coli*, the mean protein elongation rate can be as fast as 20 aa/s. Single elongation cycles must be carried out in less than ~50 ms (7). There are 61 different codons and 43 different aa-tRNA types (43 different ternary complexes) (9). Forty-eight codons match only one type of ternary complex, 12 match two types, and one matches three types. Fully 40 unique codons are used with at least 1% frequency (41). For a given mRNA codon poised at the 30S decoding site, the average chance that a particular ternary complex carries a cognate (completely matching) aa-tRNA anticodon is roughly 1 in 40. This means that on average, approximately 40 different ternary complexes must be sampled before a cognate aa-tRNA is found. (See Appendix for the probabilistic calculation.) Sampling and testing of these complexes must occur faster than the complete elongation cycle time of 50 ms, suggesting an upper limit of ~1 ms on the average time taken for ternary complex evaluation.

Selection for cognate aa-tRNA is a two-stage process (1, 9). Essentially all non-cognate ternary complexes and a large majority of near-cognate ternary complexes dissociate from L7/L12 in the initial recognition stage, prior to GTP hydrolysis by EF-Tu. This can be seen from the "theoretical *in vivo*" rate constants of Lipowsky and co-workers (9). Those events should dominate our single-molecule observations. The small fraction of near-cognate ternary complexes that pass through the initial stage are efficiently rejected in the proofreading stage, which occurs after GTP hydrolysis (9). Only cognate aa-tRNAs move forward rapidly through both stages, efficiently achieving A-state accommodation.

Our single-molecule tracking study provides some new insight into the spatial distribution and timescale of binding and unbinding events between EF-Tu (ternary complexes) and translating ribosomes in *E. coli*. These methods cannot dissect binding events for cognate vs near-cognate vs non-cognate ternary complexes. Instead, the measurements probe the timescale of the initial, codon-independent binding and unbinding with L7/L12. The new *in vivo* results corroborate several mechanistic inferences previously gleaned from a large body of *in vitro* kinetics measurements (1). Evidently the high concentration of ternary complexes, the segregation of 70S ribosomes in the ribosome-rich regions of the cytoplasm, the presence of four L7/L12 binding sites per 70S ribosome, and the flexible attachment of the L7/L12 binding sites to the ribosome all combine to enable extremely rapid sampling of aa-tRNA copies by the 70S ribosome.

Our interpretation of D_{slow} = 1 μm^2-s^{-1} as arising from a composite state involving rapid exchange between 80% ribosome-bound ternary complexes (τ_{on}) and 20% free ternary complexes (τ_{off}) within the ribosome-rich regions led to the inequality ($\tau_{on} + \tau_{off}$) $\leq$ 2 ms. This result is consistent with the requisite fast sampling and rejection of ternary complexes required

by the predominance of non-cognate and near-cognate aa-tRNAs. The estimated lower bounds on the bimolecular binding rate constant k_1 and the unimolecular dissocation rate k_{-1} are consistent with recent theoretical estimates of the analogous *in vivo* rate constants (9). The novel method used for scaling of *in vitro* rates to find the optimal set of *in vivo* rates that match the overall *E. coli* translation rate seems remarkably successful.

2.5.2 Ribosomal L7/L12 sites bind multiple ternary complexes simultaneously

The new data provide strong evidence that *multiple* ternary complexes bind *simultaneously* to the four L7/L12 sites on the 50S subunit of translating ribosomes. Our partitioning analysis suggests that the four L7/L12 sites may be saturated with ternary complexes on average. Such a high local concentration of tethered aa-tRNAs would greatly facilitate the rapid sampling required for efficient protein elongation, as previously suggested (4). The enhanced sampling rate would arise from two effects. During the same time interval in which one of the bound ternary complexes is being tested, any open L7/L12 site can be replenished with a fresh ternary complex. This saves time. In addition, when an A-site comes open after a codon match and translocation or (more typically) after rejection of a non-cognate aa-tRNA, the diffusive search for the open A site by a new ternary complex would be more rapid due to the high local concentration and the spatial constraints imposed by the tethering.

There is extensive biochemical evidence *in vitro* supporting our underlying assumption that ternary complexes aa-tRNA–EF-Tu(GTP) bind the ribosome via contact between L7/L12 and EF-Tu. A comprehensive summary is provided in Ref. (4). As shown schematically in Fig. 2.1A, L7/L12 comprises an N-terminal dimerization module and a globular C-terminal domain (CTD), connected by a flexible hinge. In *E. coli*, four copies of L7/L12 are bound to L10, which is itself flexible. An early chemical crosslinking and fluorescence study implicated L7/L12 in the binding

of EF-Tu to the ribosome (6). Subsequent extraction/complementation experiments showed that the presence of L7/L12 was required for binding of both EF-Tu and EF-G to the ribosome (42). Specific point mutations in the L7/L12 CTD and in the G domain of EF-Tu affected binding of ternary complexes to the ribosome (5). In addition, there is homology between the proposed L7/L12 binding interface to EF-Tu and the well characterized structure of the EF-Ts/EF-Tu complex. The L7/L12 subunits do not appear in crystal structures of 70S ribosomes (2, 43). However, the biochemical evidence is corroborated by an early reconstruction from cryo-EM data with 1.8 nm resolution that shows density connecting the G domain of EF-Tu within a ternary complex to the L7/L12 stalk of the ribosome (13). Finally, the correspondence between the diminished binding of the mutant form EF-Tu^{L148A} *in vitro* (5) and in live *E. coli* (Fig. 2.4) corroborates the assertion that we are probing ternary complex binding to L7/L12.

Wahl and co-workers (4) combined biochemical and additional structural evidence to propose the model of the stalk that we reproduce schematically in Fig. 2.1A. The schematic shows four ternary complexes bound to the ribosome via the four L7/L12 CTDs. One ternary complex is undergoing codon testing at the A site, while the other three are tethered and awaiting testing. The flexible attachment of the four L7/L12 to the ribosome is likely to facilitate efficient capture of ternary complexes. The long, flexible linkers may enable the CTDs to "reach out and catch" ternary complexes that come into near proximity of the ribosome body (4, 44). Although there is no detailed structural evidence supporting the simultaneous binding of four ternary complexes, the concept is supported by our stoichiometric estimates *in vivo*. It is also supported by the remarkably large bimolecular rate constant for ternary complex binding, measured earlier *in vitro* and now estimated *in vivo.*

2.6 Conclusions

The present work provides strong evidence that multiple ternary complexes bind the four L7/L12 initial binding sites on the 50S subunit of the 70S ribosome simultaneously. We also provide a new estimate of ~1–2 ms or less for the *in vivo* timescale of binding and unbinding of non-cognate ternary complexes during the initial anticodon test. Semi-quantitative estimates of the partitioning of EF-Tu and tRNA among different binding states should help constrain models of translation in *E. coli*. In future work, tracking studies of EF-G could provide an independent estimate of the fraction of EF-G bound to 70S ribosomes at a given moment in time. That would shed light on the competition *in vivo* between EF-Tu and EF-G for L7/L12 binding sites on the 70S ribosome.

2.7 Materials and Methods

2.7.1 Bacterial strains

We chose 30°C for this study because the mEos2 labels fluoresce poorly at 37°C; also, 30°C matches the conditions of our earlier study of ribosome copy number, a result used here (19). Strains, doubling times, and oligonucleotides used are detailed in Table A2.1. In *E. coli* EF-Tu is expressed from two essentially identical genes: *tufA* and *tufB.* Both of these genes were first labeled endogenously via the lambda red technique (45) in the background strain NCM3722. The photoconvertible fluorescent protein mEos2 was covalently bound to the C-terminus of EF-Tu. These genes were then transferred to the VH1000 background strain using P1 transduction. For studies of the mutated protein EF-Tu^{L148A}, the *tufA* gene was point mutated from Leu to Ala at the 148th residue in a plasmid pASK-IBA3+ having ampicillin resistance. The plasmid mutation included a fusion of the same mEos2, again at the C-terminus of the

protein. To control for possible effects of overexpression, we also prepared a strain including a completely analogous plasmid, except that it lacked the point mutation. The 30S ribosomal subunits were labeled by expression of the protein S2-mEos2 from the chromosome.

In "EZ rich, defined medium" (EZRDM) at 30°C, the doubling time of the endogenously labeled *tufA* and *tufB* strain is 60 ± 3 min (Table A2.1A and Fig. A2.8). This is ~1.3 times longer than the doubling time of the VH1000 background strain, which is 45 ± 2 min, indicating that the mEos2 label enables fairly normal functionality of EF-Tu. The L148A mutant strain has a doubling time of 46 ± 4 min.

2.7.2 Cell growth and preparation for imaging

Bulk cultures from frozen glycerol stock solution and subcultures for imaging were grown overnight at 30°C with continuous shaking in EZRDM, which is a MOPS-buffered solution with supplemental metal ions (M2130; Teknova), glucose (2 mg/mL), supplemental amino acids and vitamins (M2104; Teknova), nitrogenous bases (M2103; Teknova), 1.32 mM K_2HPO4, and 76 mM NaCl. The next day the stationary phase culture was diluted 100-fold in fresh EZRDM and grown again to exponential phase (OD = 0.2-0.5). Cells were then plated on a polylysine coated coverslip that formed the floor of a CoverWell perfusion chamber (Invitrogen, Carlsbad, CA) with a well volume of 140 µL.

For the L148A mutant strain, when the culture reached exponential phase it was treated with anhydrous tetracycline (final concentration 45 nM) to induce expression of EF-Tu^{L148A}–mEos2 from the plasmid. Tetracycline was washed away after 5 min of induction and the cells were grown for 30 min more in fresh medium prior to plating and imaging. To test for the effects of treatment by rifampicin (Rif), cells were grown to exponential phase after which Rif was added

to a final concentration of 250 µg/mL. The culture remained at 30°C for 3 hr, after which cells were plated and imaged.

2.7.3 Superresolution imaging of live *E. coli* cells

Imaging of cells began within 5 min of plating. Individual fields of view were imaged no longer than 20 s to minimize laser damage. Each prepared sample was imaged for no longer than 30 min, during which time cells continued to grow normally. Cells were imaged on an inverted microscope (Nikon Instruments, model Eclipse-Ti, Melville, NY) equipped with an oil immersion objective (CFI Plan Apo Lambda DM 100x Oil, 1.45 NA; Nikon Instruments), a 1.5x tube lens, and the Perfect Focus System (Nikon Instruments, Melville, NY). The fluorescence images were recorded on a back-plane illuminated electron-multiplying charge-coupled device (EMCCD) camera (Andor Technology, iXon DV-887, South Windsor, CT) at the rate of 485 Hz (~2 ms/frame). The camera chip consisted of 128 x 128 pixels, each 24 µm x 24 µm. The fluorescent protein mEos2 was activated using a 405 nm laser (CrystalLaser, Reno, Nevada, CW laser); the photoswitched state was subsequently excited with a 561 nm laser (Coherent Inc., Sapphire CW laser, Bloomingfield, CT). Both lasers illuminated the sample for the entire duration of image acquisition. Emission was collected through a 617/73 bandpass filter (bright line 617/73-25; Semrock, Rochester, NY). The 405 nm power density at the sample was ~5-10 W/cm^2, which kept the number of activated molecules less than two in each camera frame. The 561 nm laser power density at the sample was ~8 kW/cm^2.

2.7.4 Single-molecule image analysis

The fluorescent images were analyzed using a MATLAB GUI developed in our lab (23). Noise was attenuated using 2 different digital filters. After filtering, fluorescent signals were identified using a peak finding algorithm with a user defined intensity threshold with pixel level

accuracy. A particle is identified if the local intensity maximum is higher than the threshold. The threshold is carefully chosen large enough so that the algorithm can distinguish between background and signal and small enough to avoid cutting trajectories unduly short.

A centroid algorithm was used to locate the identified particles with sub-pixel resolution (23). Rapidly moving molecules have images that are blurred asymmetrically due to diffusion during the camera frame. Centroid fitting can locate the particles with better accuracy than Gaussian fitting. The centroid algorithm is also faster computationally. A 7 x 7 pixel box was drawn around the intensity maxima and the centroid of all the pixel intensities within the box was calculated. The centroid positions from successive frames were connected to form a trajectory only if they lie within 3 pixel = 480 nm of each other. A modified MATLAB version of the tracking program written by Crocker and Grier (46) was used.

2.7.5 Analysis of diffusive behavior

Details of spatial distribution, mean-square displacement plots, trajectory simulations, two-state modeling of $P(r)$ distributions, and estimation of uncertainties in fitting parameters are provided in Appendix.

2.8 Tables and Figures

Table 2.1. Summary of best-fit diffusion coefficients and fractional populations.

Species (treatment) [a]	D_{mean} (μm^2/s) [b]	f_{slow} [c]	D_{slow} (μm^2/s)	D_{fast} (μm^2/s)
EF-Tu WT [d]	2.02 ± 0.19	0.60 ± 0.05	1.0 ± 0.2	4.9 ± 1.2
Ribosome WT [e]	0.4 ± 0.1	0.7 ± 0.05	0.1 ± 0.1	1.2 ± 0.5
EF-Tu^{L148A} mutant [d]	3.1 ± 0.3	0.3 ± 0.05	1.2 ± 0.5	4.5 ± 1.0
EF-Tu (after Rif) [d]	3.5 ± 0.4	0.35 ± 0.05	1.5 ± 0.5	4.9 ± 1.5
EF-Tu^{L148A} mutant (after Rif) [d]	5.2 ± 0.4	0.1 ± 0.05	1.9 ± 1.2	5.6 ± 1.2

[a] Normal growth conditions, except for measurements after rifampicin treatment as noted.

[b] Mean diffusion coefficient estimated from first two points of MSD plot (Fig. 2.2).

[c] Best-fit fractional population of the more slowly diffusing state. The fractional population of the more rapidly diffusing state is $f_{fast} = 1 - f_{slow}$.

[d] C-terminus labeling with mEos2.

[e] 30S subunits labeled by expression of the ribosomal protein S2–mEos2.

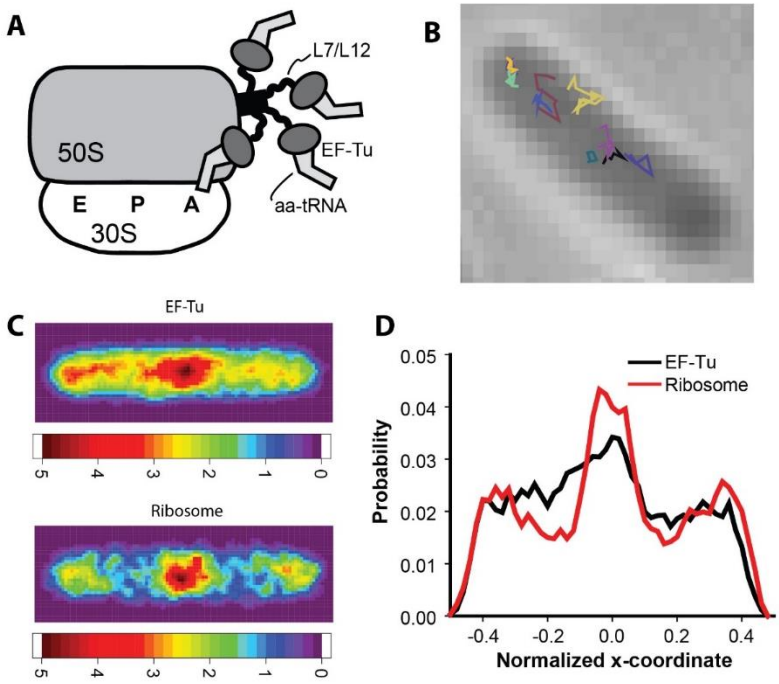

Figure 2.1. A) Schematic diagram showing four ternary complexes bound to the four L7/L12 units on the stalk of a 70S ribosome. One of the ternary complexes is also bound to the A site for codon testing. Based on the model of Ref. (4). We emphasize that while biochemical studies support binding of the ternary complex to L7/L12, the stalk is highly mobile in all structural studies to date (2). **B)** Several single-molecule trajectories of EF-Tu–mEos2 plotted in different colors and superimposed on the phase contrast image of the same cell. **C)** *Top:* Composite spatial distribution heat map of EF-Tu–mEos2 for 4221 localizations from 201 *E. coli* cells of length 4-5 µm. Pixels are ~ 45 nm x 45 nm. The intensity scale shows relative counts per pixel. *Bottom:* Composite spatial distribution heat map of ribosomes (30S–mEos2 labeling) for 1967 localizations from 108 *E. coli* cells of length 4-5 µm. **D)** The projected axial distribution of EF-Tu–mEos2 and ribosomes (30S–mEos2) for the same sets of cells used in panels C and D. The distributions are normalized to the same area and plotted on a relative scale of –0.5 to +0.5 for the long axis.

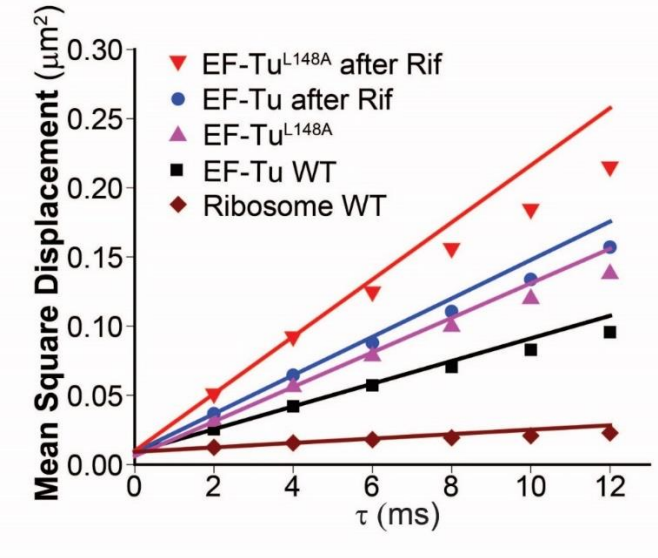

Figure 2.2. Mean-square displacement (MSD) plots for WT EF-Tu, the mutant form EF-Tu^{L148A}, and ribosomes under normal growth and Rif treatment as indicated. Slopes from the first two points yield population-averaged diffusion coefficient estimates as follows.

WT EF-Tu: 2.02 ± 0.19 μm^2/s; WT EF-Tu after Rif treatment: 3.5 ± 0.4 μm^2/s;

mutant EF-Tu^{L148A}: 3.1 ± 0.3 μm^2/s; mutant EF-Tu^{L148A} after Rif treatment: 5.2 ± 0.4 μm^2/s;

ribosomes (30S–mEos2 labeling): 0.4 ± 0.1 μm^2/s.

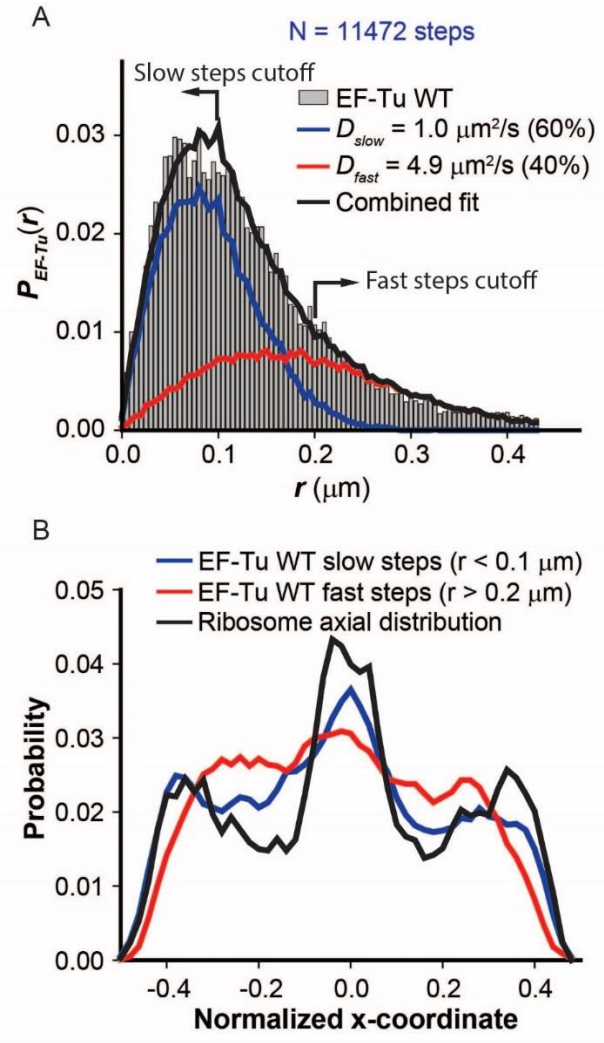

Figure 2.3. A) The experimental distribution of single-step displacements $P_{EF\text{-}Tu}(r)$ (grey histogram) for 11,472 2-ms steps for WT EF-Tu. Solid black line shows best-fit model using two static states: "slow" (blue) and "fast" (red). Model parameters: f_{slow} = 0.6, D_{slow} = 1.0 μm^2/s), f_{fast} = 0.4, D_{fast} = 4.9 μm^2/s. **B)** Axial distributions of predominantly slow (blue) and fast (red) single-step displacements of WT EF-Tu in comparison with ribosome axial distribution (30S–mEos2 labeling, black). The cutoffs chosen to separate slow (<0.1 μm) and fast (>0.2 μm) single step displacements are indicated by the arrows in panel A. The distributions are normalized to the same area and plotted on a relative scale of –0.5 to +0.5 for the long axis.

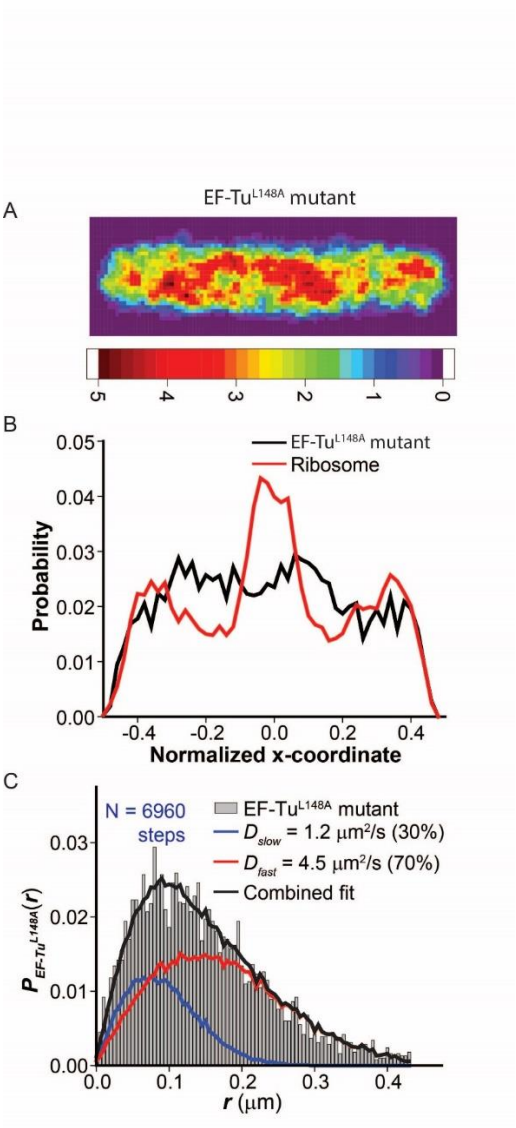

Figure 2.4. A) Composite spatial distribution heat map of the mutant form EF-Tu^{L148A}–mEos2 for 792 localizations from 123 *E. coli* cells of length 4-5.5 µm. Pixels are ~ 45 nm x 45 nm. The intensity scale shows relative counts per pixel. **B)** Axial distributions of EF-Tu^{L148A} mutant (black) in comparison with ribosomes (30S–mEos2 labeling, red). The distributions are normalized to the same area and plotted on a relative scale of –0.5 to +0.5 for the long axis. **C)** Distribution of single-step displacements $P(r)$ (grey histogram) for 6960 steps of the EF-Tu^{L148A} mutant. Solid black line shows best-fit model using two static states: "slow" (blue) and "fast" (red). Model parameters: f_{slow} = 0.3, D_{slow} = 1.2 µm^2/s, f_{fast} = 0.7, D_{fast} = 4.5 µm^2/s.

2.9 References:

1. Wohlgemuth I, Pohl C, Mittelstaet J, Konevega AL, Rodnina MV. 2011. Evolutionary optimization of speed and accuracy of decoding on the ribosome. Philos Trans R Soc Lond B Biol Sci 366:2979-86.

2. Voorhees RM, Ramakrishnan V. 2013. Structural basis of the translational elongation cycle. Annu Rev Biochem 82:203-36.

3. Carvalho MD, Carvalho JF, Merrick WC. 1984. Biological characterization of various forms of elongation factor 1 from rabbit reticulocytes. Arch Biochem Biophys 234:603-11.

4. Diaconu M, Kothe U, Schlunzen F, Fischer N, Harms JM, Tonevitsky AG, Stark H, Rodnina MV, Wahl MC. 2005. Structural basis for the function of the ribosomal L7/12 stalk in factor binding and GTPase activation. Cell 121:991-1004.

5. Kothe U, Wieden HJ, Mohr D, Rodnina MV. 2004. Interaction of helix D of elongation factor Tu with helices 4 and 5 of protein L7/12 on the ribosome. J Mol Biol 336:1011-21.

6. Traut RR, Dey D, Bochkariov DE, Oleinikov AV, Jokhadze GG, Hamman B, Jameson D. 1995. Location and domain structure of Escherichia coli ribosomal protein L7/L12: site specific cysteine crosslinking and attachment of fluorescent probes. Biochem Cell Biol 73:949-58.

7. Dennis PP, Bremer H. 1974. Differential rate of ribosomal protein synthesis in *Escherichia coli* B/r. J Mol Biol 84:407-422.

8. Young R, Bremer H. 1976. Polypeptide-chain-elongation rate in *Escherichia coli* B/r as a function of growth rate. Biochem J 160:185.

9. Rudorf S, Thommen M, Rodnina MV, Lipowsky R. 2014. Deducing the kinetics of protein synthesis in vivo from the transition rates measured in vitro. PLoS Comput Biol 10:e1003909.

10. Klumpp S, Scott M, Pedersen S, Hwa T. 2013. Molecular crowding limits translation and cell growth. Proc Natl Acad Sci U S A 110:16754-9.

11. Blanchard SC, Gonzalez RL, Kim HD, Chu S, Puglisi JD. 2004. tRNA selection and kinetic proofreading in translation. Nat Struct Mol Biol 11:1008-1014.

12. Geggier P, Dave R, Feldman MB, Terry DS, Altman RB, Munro JB, Blanchard SC. 2010. Conformational sampling of aminoacyl-tRNA during selection on the bacterial ribosome. J Mol Biol 399:576-95.

13. Stark H, Rodnina MV, Rinke-Appel J, Brimacombe R, Wintermeyer W, Heel Mv. 1997. Visualization of elongation factor Tu on the *Escherichia coli* ribosome. Nature 389:403-406.

14. Biteen JS. 2013. Intracellular dynamics of bacterial proteins are revealed by super-resolution microscopy. Biophys J 105:1547-8.

15. Bakshi S, Choi H, Weisshaar JC. 2015. The spatial biology of transcription and translation in rapidly growing *Escherichia coli*. Front Microbiol 6:636.

16. Mohapatra S, Choi H, Ge X, Sanyal S, Weisshaar JC. 2017. Spatial Distribution and Ribosome-Binding Dynamics of EF-P in Live Escherichia coli. MBio 8.

17. English BP, Hauryliuk V, Sanamrad A, Tankov S, Dekker NH, Elf J. 2011. Single-molecule investigations of the stringent response machinery in living bacterial cells. Proc Natl Acad Sci USA 108:E365-E373.

18. McKinney SA, Murphy CS, Hazelwood KL, Davidson MW, Looger LL. 2009. A bright and photostable photoconvertible fluorescent protein for fusion tags. Nat Methods 6:131-133.

19. Bakshi S, Siryaporn A, Goulian M, Weisshaar JC. 2012. Superresolution imaging of ribosomes and RNA polymerase in live *Escherichia coli* cells. Mol Microbiol 85:21-38.

20. Plochowietz A, Farrell I, Smilansky Z, Cooperman BS, Kapanidis AN. 2016. In vivo single-RNA tracking shows that most tRNA diffuses freely in live bacteria. Nucleic Acids Res doi:10.1093/nar/gkw787.

21. Furano AV. 1977. The elongation factor Tu coded by the *tufA* gene of *Escherichia coli* K-12 is almost identical to that coded by the *tufB* gene. J Biol Chem 252:2154-7.

22. Nenninger A, Mastroianni G, Mullineaux CW. 2010. Size dependence of protein diffusion in the cytoplasm of *Escherichia coli*. J Bacteriol 192:4535-40.

23. Bakshi S, Bratton BP, Weisshaar JC. 2011. Subdiffraction-limit study of Kaede diffusion and spatial distribution in live *Escherichia coli*. Biophys J 101:2535-44.

24. Ban N, Freeborn B, Nissen P, Penczek P, Grassucci RA, Sweet R, Frank J, Moore PB, Steitz TA. 1998. A 9 A resolution X-ray crystallographic map of the large ribosomal subunit. Cell 93:1105-15.

25. Clemons WM, May JLC, Wimberly BT, McCutcheon JP, Capel MS, Ramakrishnan V. 1999. Structure of a bacterial 30S ribosomal subunit at 5.5 Å resolution. Nature 400:833-840.

26. Brandt F, Etchells SA, Ortiz JO, Elcock AH, Hartl FU, Baumeister W. 2009. The native 3D organization of bacterial polysomes. Cell 136:261-71.

27. Sanamrad A, Persson F, Lundius EG, Fange D, Gynnå AH, Elf J. 2014. Single-particle tracking reveals that free ribosomal subunits are not excluded from the *Escherichia coli* nucleoid. Proc Natl Acad Sci USA 111:11413-11418.

28. Manley S, Gillette JM, Patterson GH, Shroff H, Hess HF, Betzig E, Lippincott-Schwartz J. 2008. High-density mapping of single-molecule trajectories with photoactivated localization microscopy. Nat Methods 5:155-157.

29. Michalet X. 2010. Mean Square Displacement Analysis of Single-Particle Trajectories with Localization Error: Brownian Motion in Isotropic Medium. Phys Rev E Stat Nonlin Soft Matter Phys 82:041914-041914.

30. Press WH, Teukolsky SA, Vetterling WT, Flannery BP. 2007. Numerical Recipes 3rd Edition: The Art of Scientific Computing. Cambridge University Press.

31. Bakshi S, Choi H, Mondal J, Weisshaar JC. 2014. Time-dependent effects of transcription- and translation-halting drugs on the spatial distributions of the *E. coli* chromosome and ribosomes. Mol Microbiol 94:871-887.

32. Cabrera JE, Cagliero C, Quan S, Squires CL, Jin DJ. 2009. Active transcription of rRNA operons condenses the nucleoid in Escherichia coli: examining the effect of transcription on nucleoid structure in the absence of transertion. J Bacteriol 191:4180-5.

33. Schmidt A, Kochanowski K, Vedelaar S, Ahrne E, Volkmer B, Callipo L, Knoops K, Bauer M, Aebersold R, Heinemann M. 2016. The quantitative and condition-dependent *Escherichia coli* proteome. Nat Biotechnol 34:104-10.

34. Dong H, Nilsson L, Kurland CG. 1996. Co-variation of tRNA Abundance and Codon Usage in *Escherichia coli* at Different Growth Rates. J Mol Biol 260:649-663.

35. Abdulkarim F, Ehrenberg M, Hughes D. 1996. Mutants of EF-Tu defective in binding aminoacyl-tRNA. FEBS Letters 382:297-303.

36. Uemura S, Aitken CE, Korlach J, Flusberg BA, Turner SW, Puglisi JD. 2010. Real-time tRNA transit on single translating ribosomes at codon resolution. Nature 464:1012-7.

37. Chen C, Stevens B, Kaur J, Smilansky Z, Cooperman BS, Goldman YE. 2011. Allosteric vs. spontaneous exit-site (E-site) tRNA dissociation early in protein synthesis. Proc Natl Acad Sci U S A 108:16980-5.

38. Defeu Soufo HJ, Reimold C, Linne U, Knust T, Gescher J, Graumann PL. 2010. Bacterial translation elongation factor EF-Tu interacts and colocalizes with actin-like MreB protein. Proc Natl Acad Sci U S A 107:3163-8.

39. Graumann PL. 2007. Cytoskeletal elements in bacteria. Annu Rev Microbiol 61:589-618.

40. Liu Z, Xing D, Su QP, Zhu Y, Zhang J, Kong X, Xue B, Wang S, Sun H, Tao Y, Sun Y. 2014. Super-resolution imaging and tracking of protein-protein interactions in sub-diffraction cellular space. Nat Commun 5:4443.

41. Maloy S, V. Stewart, and R. Taylor. 1996. Genetic analysis of pathogenic bacteria. Cold Spring Harbor Laboratory Press, NY.

42. Wahl MC, Moller W. 2002. Structure and function of the acidic ribosomal stalk proteins. Curr Protein Pept Sci 3:93-106.

43. Schmeing TM, Voorhees RM, Kelley AC, Gao Y-G, Murphy FV, Weir JR, Ramakrishnan V. 2009. The Crystal Structure of the Ribosome Bound to EF-Tu and Aminoacyl-tRNA. Science 326:688.

44. Rodnina MV, Pape T, Fricke R, Kuhn L, Wintermeyer W. 1996. Initial Binding of the Elongation Factor Tu·GTP·Aminoacyl-tRNA Complex Preceding Codon Recognition on the Ribosome. J Biol Chem 271:646-652.

45. Thomason LC, Sawitzke JA, Li X, Costantino N, Court DL. 2014. Recombineering: genetic engineering in bacteria using homologous recombination. Curr Protoc Mol Biol 106:1.16.1-39.

46. Crocker JC, Grier DG. 1996. Methods of digital video microscopy for colloidal studies. J Colloid Interface Sci 179:298-310.

2.10 Appendix:

A2.1 Bacterial strains and oligonucleotides used in this work

See Tables A2.1A and A2.1B below. Growth curves in Fig. A2.8.

A2.2 Analysis of diffusive behavior

A2.2.1 *Mean-square displacement plots MSD*(τ)

The MSD as a function of lag time τ is given by $MSD(\tau) = < (\boldsymbol{r}(t+\tau) - \boldsymbol{r}(t))^2 >$, where $\boldsymbol{r}(t)$ is the two-dimensional location of the particle at time t, τ is the lag time, and the average is taken over all times t and over many trajectories. MSD(τ) plots for the different species and imaging conditions are shown in Fig. 2.2. The slope of the first two points of an MSD(τ) plot provides a first estimate of the mean diffusion coefficient: D = slope/4. The MSD slope takes account of the localization error σ (1), but does not account for confinement effects. Even for 6 x 2 ms = 12 ms long trajectories, for rapidly diffusing species with $D \sim 5$ μm^2-s^{-1} confinement restricts diffusive trajectories and causes curvature of the MSD plot. This makes the diffusion coefficient from the two-point slope a lower bound on the true mean D. The trajectory analysis presented below is more accurate.

A2.2.2 *Estimation of dynamic localization error σ_{fast} and σ_{slow} for fast and slow EF-Tu molecules*

Localization error in the single-step $P(r)$ distributions arises from the point-spread function (PSF) of the microscope, the finite number of photons detected per camera frame, and blurring of the images due to diffusive motion during each 2 ms camera frame (1, 2). While ribosomes and slow EF-Tu copies experience little diffusive blurring, the fast EF-Tu copies are blurred substantially. We reasoned that model Monte Carlo diffusive trajectories should involve larger dynamic localization error for fast EF-Tu copies than for slow EF-Tu copies.

This problem has been addressed in detail by Michalet (1). Suppose the best fit to the first two experimental points of a two dimensional mean-square displacement plot is given by the equation MSD(τ) = $a + b\tau$, with b the slope and a the extrapolated intercept at lag time $\tau = 0$. Then the best estimate of the diffusion coefficient is $D = b/4$ and the best estimate of the dynamic localization error is $\sigma = \frac{1}{2}\,(a + 4Dt_E/3)^{1/2}$, where t_E is the exposure time per camera frame. We estimate that the diffusion coefficient of the fast (non-ribosome-bound) EF-Tu copies should be about 5 μm^2-s^{-1} (3, 4) and that of the ribosome-bound copies should be about 0.2 μm^2-s^{-1} (5). If so, the root-mean-square displacement in two dimensions of a fast EF-Tu copy during the 2-ms camera frame is ~200 nm, substantially larger than typical static localization errors in live *E. coli* single-molecule studies of slowly moving species labeled with fluorescent proteins. The rms displacement of a ribosome-bound EF-Tu copy is only ~60 nm, comparable to typical static localization errors.

For WT EF-Tu, the intercept of the MSD plot yields a mean localization error σ = 60 nm. To estimate the dynamic localization errors σ_{fast} and σ_{slow} for EF-Tu, we simulated six-step (6 x 2 ms) Monte Carlo diffusive trajectories in a model spherocylinder. One batch of 5000 trajectories had D_{slow} = 0.2 $\mu m^2/s$ and the other 5000 trajectories had D_{fast} = 5 $\mu m^2/s$; both used the mean localization error of 60 nm. These simulated trajectories were used to form the distribution of the mean of six one-step estimates of D:

$< D >_{6-step} = \frac{1}{24\tau}\sum_{i=1}^{6}\sqrt{(x_{i+1}-x_i)^2 + (y_{i+1}-y_i)^2}$, where (x_{i+1}, y_{i+1}) and (x_i, y_i) are the coordinates of final and initial positions of each step. This distribution is shown in Fig. A2.6A. For WT EF-Tu, the analogous experimental distribution of $<D>_{6\text{-step}}$ is shown in Fig. A2.6B. The simulated distributions guided the choice of cutoffs that approximately distinguish slow from fast copies: <2.25 $\mu m^2/s$ for slow copies and >3.25 $\mu m^2/s$ for fast copies. Separate MSD plots for

these slow and fast experimental trajectories are shown in Fig. A2.6C. The intercepts of the linear fits to the first two data points gives the estimates $\sigma_{slow} \sim 40$ nm and $\sigma_{fast} \sim 80$ nm. These values were used to simulate trajectories for fitting the $P_{EF\text{-}Tu}(r)$ distributions to two static populations.

A2.3 Monte Carlo simulations of diffusive trajectories

Many previous studies of single-molecule diffusion fit the experimental $P(r)$ distribution to a sum of analytical functions, with each component describing diffusion of the species in free space (6, 7). However, molecules diffusing rapidly in the *E. coli* cytoplasm suffer from confinement due to the spherocylindrical cell boundaries, a problem for which there is no analytical solution. Therefore, we simulated the behavior of each diffusive component from a large number of random walk trajectories that incorporate the dynamic localization error σ_{slow} or σ_{fast} and confinement effects within a model spherocylinder that mimics the dimensions of a typical *E. coli* cell in our growth conditions (tip-to-tip cell length = 4.3 μm and cell diameter = 0.9 μm). Each set of simulations models one diffusive state, with values of D and σ fixed. At $t = 0$, 5000 particles were randomly distributed within the cell volume. Each particle undergoes a random walk independent of other particle positions. To model each 2-ms camera image, three-dimensional microtrajectories (1000 steps of 2 μs each) were generated. At each time step, each particle chooses a displacement in each of three Cartesian directions. These displacements are chosen from a Gaussian distribution whose standard deviation corresponds to the state's three-dimensional diffusion coefficient D. In the rare event that a particle attempts to step outside of the cell boundaries, the displacement for that microstep is taken to be zero. The location of each particle during each camera frame is obtained as the centroid of the model microtrajectories in order to mimic the analysis procedure used for the experimental images. The

appropriate dynamic localization error σ was then applied to each centroid location in both *x* and *y* coordinates by sampling a Gaussian distribution with standard deviation σ. By adding the error to the centroid position we obtain the model "measured" location for each 2 ms camera frame. The *x* and *y* coordinates of each measured location are stored for further analysis. For the next model camera frame, each particle continues to make microsteps in 3D starting from the endpoint of the previous camera frame. Model trajectories for EF-Tu use the appropriate estimated value of σ_{slow} or σ_{fast}, determined as described above.

By connecting the sequence of simulation locations over seven frames, we form 5000 model trajectories for each relevant value of *D*. These trajectories are used to compute model-based, numerical one-step probability distributions $P_{model}(r;D)$ that are the model functions for the least-squares analysis of the corresponding experimental distributions.

A.2.3.1 ***Fitting of single-step P(r) distributions to static, two-state models***

For each species in each experimental condition, a large set of trajectories that lasted for 6 steps or longer were selected for analysis. Longer trajectories were truncated to 6 steps. The 6-step trajectories were then sliced into individual steps. The single-step displacements $r_i = \sqrt{(x_{i+1} - x_i)^2 + (y_{i+1} - y_i)^2}$ were pooled to form the distribution $P(r)$, as in Figs. 2.3A and 2.4C. We typically attempt to fit the experimental distribution $P(r)$ in a least-squares sense to a single population or to a weighted average of two static populations. For a one-state model the only fitting parameter is *D*. For unconstrained models including two static (non-exchanging) states, the fitting function is the linear combination $P_{model}(r) = f_{slow}P(r;D_{slow}) + (1 - f_{slow})P(r;D_{fast})$. Here the three fitting parameters are D_{fast}, D_{slow}, and the fractional population f_{slow}, which in turn fixes $f_{fast} = (1 - f_{slow})$. For all our fitting procedures, D_{fast} ranged from 0.1 to 12 μm^2/s with interval of 0.1 μm^2/s and D_{slow} ranged from 0.05 to 3 μm^2/s with interval of 0.05 μm^2/s.

We judge the goodness of fit by evaluating the reduced chi-square statistic: $\chi_\nu^2 = \frac{1}{(N-\alpha)} \sum_{j=1}^{N} \frac{(h_j - y_j)^2}{s_j^2}$. Here j labels the N bins in the (unnormalized) $P(r)$ and $P_{model}(r)$ histograms, h_j is the number of experimental counts in bin j, y_j is the number of counts in bin j of the simulated $P_{model}(D_i)$ histogram, s_j^2 is the variance of the value in bin j, and α is the number of fitted parameters. We take $s_j^2 = h_j$ as the estimate of the variance, assuming Poisson statistics. A good fit to an adequately flexible *analytical* model function should have $\chi_\nu^2 \sim 1$. In our numerical procedure, both the experimental distribution $P(r)$ and the fitting function $P_{model}(r)$ have noise, so we would expect good fits to have χ_ν^2 values somewhat larger than 1. The fitting results for each species in various conditions are summarized in the main text and in Table 2.1.

To estimate the uncertainty in the model parameters for two-state fits, we examined the 3D grid of χ_ν^2 values generated from the unconstrained fits that varied all three parameters D_{fast}, f_{slow}, and D_{slow}. For WT EF-Tu, three two-dimensional planes passing through the values D_{fast} = 4.9 μm^2-s^{-1}, f_{slow} = 0.60, and D_{slow} = 1.0 μm^2-s^{-1} are shown in Fig. A2.7. We judged the fits to be qualitatively poor whenever the value of χ_ν^2 exceeded the minimum value by 0.5 units or more (Fig. A2.7). The parameter error estimates in Table 2.1 cover this range of χ_ν^2 values in each case.

A2.3.2 *Fitting of single-step $P_{EF\text{-}Tu}(r)$ distributions to static, three-state models*

We briefly explored three-state models (slow, fast, and medium) of the WT EF-Tu $P(r)$ distribution of Fig. 2.3A. To make the search tractable, the slow and fast diffusion coefficients were fixed to 0.1 and 4.9 μm^2/s, mimicking ribosome-bound and free EF-Tu states. The slow and the medium fractions were varied in intervals of 0.05 and the medium fraction diffusion

coefficient D_{medium} from 0.1-5 μm^2/s in intervals of 0.1 μm^2/s. The fast fraction was determined as $f_{fast} = 1 - f_{slow} - f_{medium}$. The best fit parameters were $f_{slow} = 0.20 \pm 0.05$, $f_{medium} = 0.45 \pm 0.05$, and $D_{medium} = 1.8 \pm 0.5$ μm^2/s, with $f_{fast} = 0.35 \pm 0.05$ and $\chi_v^2 = 1.25$ (Fig. A2.1C). This is no better fit than the best two-state model, which returned $\chi_v^2 = 1.24$. For the three-state fit, $f_{slow} + f_{medium} = 0.65$ is in sensible agreement with the two-state result $f_{slow} = 0.60$. These fits are not very different in content. The sum of the slow and medium components in the best three-state fit is quite similar to the slow component of the best two-state fit.

A2.4 Statistics of aa-tRNA sampling

The time-averaged stoichiometry of EF-Tu and tRNA binding to a translating 70S ribosome can be estimated from the fraction of EF-Tu copies bound to ribosomes combined with copy number estimates from other studies. There are 61 different codons and 43 different aa-tRNA types (43 different ternary complexes) used by *E. coli* (8). Forty-eight codons match only one type of ternary complex, 12 match two types, and one matches three types. This means that the ribosome is usually testing and rejecting non-cognate or near-cognate aa-tRNAs. In turn, this means the A site is most frequently occupied by an aa-tRNA within its ternary complex, still tethered to L7/L12 (prior to GTP hydrolysis and ejection of EF-Tu).

Fully 40 unique codons are used with at least 1% frequency (9). For a given mRNA codon poised at the 30S decoding site, the average chance that a particular ternary complex carries a cognate (completely matching) aa-tRNA anticodon is roughly 1 in 40. How many different ternary complexes must be sampled before a cognate aa-tRNA is found? For simplicity, we assume that there are N different aa-tRNA types (N different anti-codons) all required with equal probability in the transcriptome and all equally represented in the pool of aa-tRNA. This enables calculation of a closed form for the mean number of trials required to find an anti-codon that

matches the current mRNA codon at the ribosome A site. Let $p = 1/N$ be the probability of a match on a given trial. The index k denotes the number of individual trials required to achieve a codon match. If the sampling of the pool is random, then the probability $P(k)$ of finding the first match on the kth trial is the probability of failing to find a match for $(k-1)$ successive trials, which is $(1-p)^{k-1}$, times the probability of finding a match on the kth trial: $P(k) = (1-p)^{k-1} p$. The average number of trials required to find a match is:

$$< k > = \sum_{k=1}^{\infty} kP(k) = \sum_{k=1}^{\infty} k(1-p)^{k-1} p$$

$$= p\sum_{k=1}^{\infty} k(1-p)^{k-1} .$$

Let $x = (1-p)$. Then:

$$< k > = (1-x)\sum_{k=1}^{\infty} kx^{k-1}$$

$$= (1-x)\frac{d}{dx}\sum_{k=1}^{\infty} x^k$$ This is the derivative of a geometric series, which can be summed:

$$= (1-x)\frac{d}{dx}\frac{x}{1-x} = \frac{1}{1-x} = \frac{1}{p} .$$

For $p = 1/N$, the mean number of trials required to find a match is N. If $N \sim 40$, on average roughly 40 ternary complexes must be sampled before finding a cognate codon.

A2.5 Estimates of copy numbers and partitioning of EF-Tu and tRNA

Under the same growth conditions used here (30°C in EZRDM), we previously estimated ~50,000 30S ribosomal subunits per cell, some 80% of which (~40,000 copies) are engaged as translating, 70S ribosomes (10). Mean copy number estimates for EF-Tu, total tRNA, EF-G, and total aa-tRNA synthetase (Table A2.2) were derived from the ribosome copy number and from literature values of the ratio of each species' copy number to that of ribosomes. It was not possible to match strains, growth conditions, growth rate, and temperature, so we chose to match the growth rate (~1 doubling/hr).

EF-Tu is the most abundant protein in *E. coli*, about 7-fold more abundant than ribosomes (11, 12) (~350,000 total EF-Tu copies). The two-state analysis of $P_{EF\text{-}Tu}(r)$ in Fig. 2.3A combined with the axial distribution of these slowly diffusing copies indicates that ~60% of EF-Tu copies (~210,000) locate in the 70S-rich regions of space, where they undergo rapid exchange between the ribosome-bound state (80% of the time) and rapidly diffusing state (20% of the time) on a timescale of ~2 ms or less. At a given moment, this corresponds to ~170,000 ribosome-bound EF-Tu copies (0.8 x 0.6 x 350,000). The remaining ~180,000 EF-Tu copies comprise free ternary complexes and bare EF-Tu seeking an aa-tRNA partner. The ~170,000 ribosome-bound EF-Tu copies is four times the estimated number of translating, 70S ribosomes. In *E. coli*, there are four L7/L12 sites per 50S subunit (13, 14). Under the assumption that ternary complexes bind to the ribosome only when interacting with L7/L12 N-terminal domains (further justified below), we infer that the four L7/L12 sites are essentially saturated with EF-Tu copies. An equilibrium binding calculation (below) corroborates this conclusion.

This analysis ignores the fact that each time a cognate aa-tRNA binds to the A site and transfers its aminoacyl group to the growing peptide chain, elongation factor G (EF-G) must bind to the A site and hydrolyze GTP in order to drive translocation of the A site tRNA to the P site and the P site tRNA to the E site. EF-G uses the same ribosomal L7/L12 sites as EF-Tu for its initial binding step (15). A tethered EF-G presumably samples the A site in much the same way as a tethered ternary complex. The estimated copy number of EF-G is 6-7 times smaller than that EF-Tu (11), *i.e.*, the EF-G copy number is similar to that of the ribosomes. *In vitro* studies found that EF-Tu and EF-G have comparable binding constants to L7/L12 units (16). Accordingly, we suggest that the mean occupancy of the four L7/L12 sites is ~3.5 EF-Tu copies (7/8 x 4) and ~0.5 EF-G copies (1/8 x 4). This seems a reasonable fractional occupancy of EF-G to ensure that a

cognate aa-tRNA at the A site need not wait long for the arrival of an EF-G(GTP) copy to drive translocation. There is only one type of EF-G vs 43 types of ternary complex, so each EF-G visit to an L7/L12 site will be much more effective than each ternary complex visit.

So far, we have estimated that averaged over time, each ribosome binds ~3.5 ternary complexes (3.5 EF-Tu and 3.5 tRNA) and 0.5 EF-G copies, all tethered to L7/L12 subunits. One of the ternary complexes typically occupies the A site. Next we estimate the partitioning of total tRNA among different species. The total tRNA copy number in *E. coli* growing at 1–2 doublings/hr is ~7-fold larger than the ribosome copy number (17). This implies ~7 x 50,000 = 350,000 total tRNA per cell in our growth conditions, the same as the estimated EF-Tu copy number. We estimate that averaged over time, each translating ribosome binds one tRNA in the A site (usually tethered to an L7/L12 via an EF-Tu bridge), one in the P site, perhaps one-half copy in the E site (a compromise between "2-1-2" and "2-3-2" elongation models (18, 19)), and an additional 2.5 copies bound as ternary complexes to the other three L7/L12 sites. Thus the time-averaged number of tRNA copies bound to each translating ribosomes is about 5. The ~40,000 translating ribosomes per cell in our growth conditions would then bind ~200,000 tRNA copies at a given moment in time (~57% of all copies). On average, 3.5 of these 5 copies (140,000) are associated with EF-Tu as ternary complexes and the other 1.5 copies (60,000) are ribosome-bound at the P and E sites and not associated with EF-Tu. The remaining ~150,000 tRNA copies (~43%) are not ribosome-bound and should partition among three diffusive states: free tRNA shortly after leaving the ribosomal E site, tRNA being recharged by aa-tRNA synthetase, and tRNA within ternary complexes.

A simple equilibrium calculation indicates that a large majority of the 290,000 tRNA copies not engaged at the ribosomal P and E sites should form ternary complexes and that most of the

350,000 EF-Tu copies also occur as ternary complexes. The binding constant *in vitro* between tRNA and EF-Tu has been measured to be K_b = 7.5 μM^{-1} (20). Binding constants are expected to be larger in the crowded cytoplasm than in buffer solution (21). The volume of an average, ~4 μm long, 0.9 μm diameter spherocylindrical cell is V_{cell} = 2.35 μm^3. For that volume, each 1000 copies corresponds to a concentration of 0.71 μM. As an illustrative calculation, suppose we mixed 350,000 free EF-Tu copies (248 μM) with 290,000 free tRNA copies (206 μM) in the cytoplasm. The solution-phase binding constant then predicts that at equilibrium, there will be 289,000 ternary complexes (accounting for 82% of all EF-Tu), 60,000 free EF-Tu copies, and only 1,000 free tRNA copies. However, that calculation neglects the tRNA copies that are bound to the 20 types of aa-tRNA synthetase, whose aggregate copy number is ~50,000 (11). In the limit of saturation of the synthetases with tRNA, only 240,000 tRNA copies would be available for binding with EF-Tu to form ternary complexes. At equilibrium, a mixture of 350,000 EF-Tu with 240,000 tRNA would yield 240,000 ternary complexes and 110,000 free EF-Tu. Roughly 70% of the EF-Tu would still exist as ternary complexes. The tRNA copies would then occur as 240,000 ternary complexes, 60,000 P- and E-site copies, 50,000 complexes with the synthetase, and only 400 free tRNA copies. This is the estimate used in the main text. Free tRNA is a small minority population in either equilibrium estimate.

Assuming the smaller estimate of 240,000 ternary complexes, we can use a second binding equilibrium calculation to estimate the average number of ternary complexes bound to the four L7/L12 units on each translating ribosome. *In vitro*, the binding constant between a single L7/L12 unit and a ternary complex is K_b = 0.1 μM^{-1} (16). Again, this likely underestimates the binding constant *in vivo*. Assume the cytoplasm initially contained 240,000 ternary complexes (170 μM) and 40,000 translating ribosomes (28 μM). Further assume independent binding

(no cooperativity) of four ternary complexes to the four L7/L12 units on each 70S ribosome (22). Then at equilibrium the average number of ternary complexes bound to each 70S ribosome is 3.8 out of a maximum of 4.

The binding model goes as follows. Let *R* stand for a 70S ribosome and *X* stand for a ternary complex. Equilibrium concentrations are denoted by square brackets; for simplicity, $x = [X]$. There are four sequential binding equilibria, each with the same binding constant *K* and its own equilibrium equation:

$$R + X \leftrightarrow RX, \qquad [RX] = [R]\,K\,x \tag{1}$$

$$RX + X \leftrightarrow RX_2, \qquad [RX_2] = [RX]\,K\,x = [R]\,K^2\,x^2 \tag{2}$$

$$RX_2 + X \leftrightarrow RX_3, \qquad [RX_3] = [RX_2]\,K\,x = [R]\,K^3\,x^3 \tag{3}$$

$$RX_3 + X \leftrightarrow RX_4, \qquad [RX_4] = [RX_3]\,K\,x = [R]\,K^4\,x^4. \tag{4}$$

Let R_0 be the total ribosome concentration and X_0 be the total ternary complex concentration:

$$R_0 = [R] + [RX] + [RX_2] + [RX_3] + [RX_4] \tag{5}$$

$$X_0 = x + [RX] + 2[RX_2] + 3[RX_3] + 4[RX_4] \tag{6}$$

Substituting Eqs. 1-4 into equations 5 and 6 and solving for $[R]$ and for $(X_0 - x)$ yields two expressions for $[R]$:

$$[R] = R_0 / (1 + Kx + K^2x^2 + K^3x^3 + K^4x^4) \quad \text{and} \tag{7}$$

$$[R] = (X_0 - x) / (Kx + 2K^2x^2 + 3K^3x^3 + 4K^4x^4) \tag{8}$$

For given values of *K* and the initial concentrations R_0 and X_0, equations 7 and 8 can be set equal to each other and solved for *x*, whose value then determines all the equilibrium concentrations. In practice, we solved the equation by trial and error using an Excel spreadsheet.

These rough estimates based on solution-phase binding constants may well underestimate the extent of complex formation, both for formation of ternary complexes from EF-Tu and aa-tRNA and for binding of ternary complexes to L7/L12 units. The estimates help to justify the

assertion that at a given moment most EF-Tu copies exist as ternary complexes. They are also consistent with the assertion that the four L7/L12 sites on each 70S ribosome are essentially saturated with ~4 bound ternary complexes. Finally, they predict that only a very small fraction of tRNA, perhaps 1% or less, exists as the free, unbound species.

A2.6 *In vivo* rate constants for binding and unbinding of ternary complexes

Finally, we can estimate two *in vivo* rate constants for direct comparison with the recent set of theoretical *in vivo* rate constants derived from a large set of *in vitro* measurements obtained under standardized experimental buffer conditions and temperature. Our interpretation of the value D_{slow} = 1.0 μm^2-s^{-1}, as a composite of 80% ribosome-bound copies and 20% free copies, suggests that the timescale for bound-free exchange *within the ribosome-rich regions* must be 2 ms or less. This constrains the ratio $\tau_{on}/\tau_{off} = 4$ and the sum $(\tau_{on} + \tau_{off}) \leq 2$ ms. For concreteness, assume that $(\tau_{on} + \tau_{off}) = 2$ ms, which yields the values $\tau_{off} = 0.4$ ms and $\tau_{on} = 1.6$ ms. The time τ_{off} is the mean search time for a ternary complex to find an empty L7/L12 site within the ribosome-rich regions.

First we use the pseudo-first-order rate τ_{off}^{-1} and the 70S ribosome concentration to estimate the effective bimolecular association rate constant k_1 for binding of a typical non-cognate ternary complex to an L7/L12 subunit of a 70S ribosome within the ribosome-rich regions. Suppose the 40,000 70S ribosomes occupy roughly half of the 2.4 μm^3 volume of the average cell; then the concentration of translating ribosomes within the ribosome-rich regions is [70S] ~ 55 μM. The effective bimolecular rate constant becomes $k_1 = \tau_{off}^{-1}/[70S] = 4.5 \times 10^7$ $M^{-1}s^{-1}$. This is remarkably fast, and if $(\tau_{on} + \tau_{off})$ were <2 ms, the estimate would be even larger. For comparison, the diffusion-limited bimolecular rate constant for ribosomal spheres of radius R_{ribo}

= 10 nm and diffusion coefficient D_{ribo} = 0.1 $\mu m^2/s$ colliding with ternary complex spheres with R_{TC} = 2 nm and D_{TC} = 5 $\mu m^2/s$ is $k_{diff} = 4\pi N_0(R_{ribo} + R_{TC})(D_{ribo} + D_{TC}) = 3.2 \times 10^8\ M^{-1}s^{-1}$, only sixfold larger than our estimated k_1. Roughly one in six close encounters between a ternary complex and a 70S ribosome, leads to a binding event. As suggested earlier (13), k_1 may be very fast due to the presence of four L7/L12 binding sites per ribosome and the flexibility of the linkages between ribosome and the C-terminal domain of L7/L12. We call k_1 an effective rate constant because in many close encounters the ternary complex will find most L7/L12 binding sites already occupied by a ternary complex or an EF-G, unlike pseudo-first-order conditions used in kinetics assays. The theoretical *in vivo* estimate for κ_{on}* (Table 2 of Ref. (8)) at 1.07 doublings/hr and 37°C is $9.4 \times 10^7\ M^{-1}s^{-1}$, twofold larger than our lower limit on k_1.

We can also compute the unimolecular dissociation rate of EF-Tu (typically part of a ternary complex) from the ribosome, $k_{-1} = \tau_{on}^{-1} \geq 625\ s^{-1}$ at 30°C with the theoretical *in vivo* rate for 1.07 doublings/hr at 37°C. The latter is $\omega_{off}^* = 1700\ s^{-1}$ (Table 2 of Ref. (8)). Correcting from our 30°C to 37°C increases k_{-1} by a factor of 2.1: $k_{-1}(37°C) = 2.1\ k_{-1}(30°C) \geq 1250\ s^{-1}$. The effects of temperature on k_{-1} were derived from the T-dependence of the experimental *in vitro* rate constants in Table 1 of Ref. (8): $k_{-1} = 85\ s^{-1}$ at 20°C and $700\ s^{-1}$ at 37°C. We assumed the Arrhenius temperature dependence with A-factor independent of T: $k_{-1}(T) = A \exp[-E_a/RT]$, with E_a the activation energy and R the gas constant.

Table A2.1A. Bacterial strains used; background strain is *E. coli* – VH1000.

Strain label	Description	Doubling time (min)
tufAB	Both *tufA* and *tufB* chromosomally labeled with mEos2 at C-terminus	60 ± 3
MM7	*tufA* labeled with mEos2, expressed from a plasmid – pASK-IBA3+	47 ± 1
MM9	$tufA^{L148A}$ mutant labeled with mEos2, expressed from a plasmid – pASK-IBA3+	46 ± 4
MSG196	*rpsB* (ribosome S2 protein) chromosomally labeled with mEos2	49 ± 2
VH1000	Background parent strain	45 ± 2

Table A2.1B. Oligonucleotides used.

Oligonucleotide	Sequence, 5′- 3′
F-EcoRI-tufA_mEos2	**GCAT *GAATTC* CAGGCCGTAATTGAAGC**
R-HinDIII-tufA-mEos2	**GCAT *AAGCTT* TTAGCGACGAGCATTATCC**
F-tufA_L148A_mut	**GCTGCTGGAA *GCA* GTTGAAATGGAAG**
R-tufA_L148A_mut	**TCTTCGTCATCAACCATG**

Table A2.2. Sources of copy number estimates relative to ribosomes.[1]

Measured species (references)	**Ratio to ribosome copy number**	***E. coli* strain**	**Growth conditions**
total EF-Tu (12, 23)	7	NC3	MOPS with 0.4% glucose (w/v) at 37˚C (~1 db/hr)
total tRNA (17)	7	W1845 (K12 derivative)	MOPS with 0.4% glucose (w/v) at 37˚C (~1 db/hr)
EF-G (23)	~1	MG1655	M9 with glucose at 37˚C
total tRNA synthetase (23)	~1	MG1655	M9 with glucose at 37˚C

[1] Estimates of mean copy number per cell in main text are taken as the mean ribosome copy number of 50,000 (from Ref. 11 below) times the ratio in this table.

Figures:

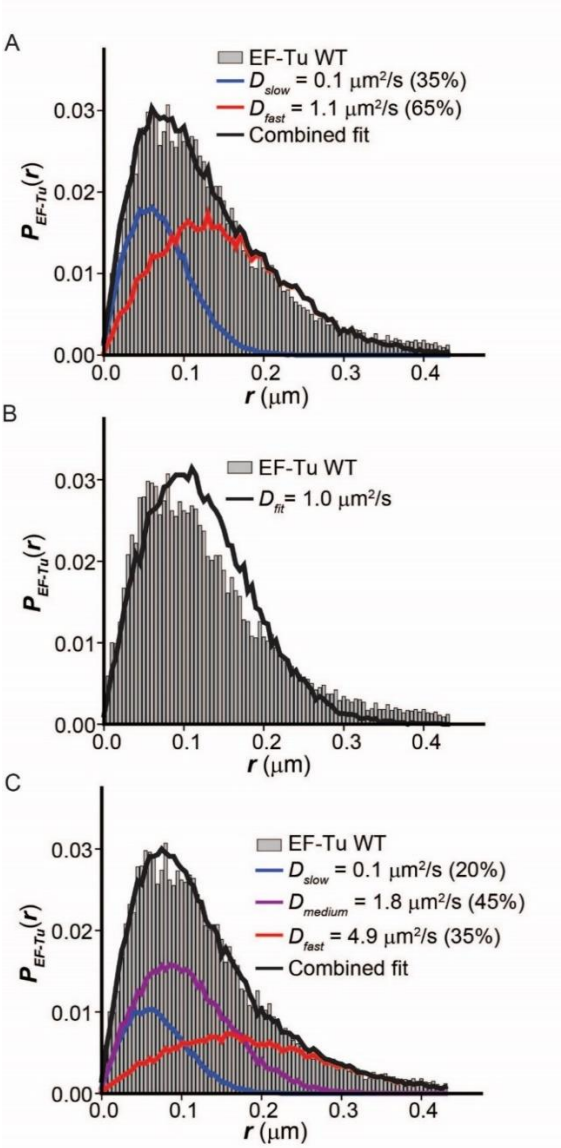

Figure A2.1. Different fitting models for WT EF-Tu single-step displacement probability distribution $P_{EF\text{-}Tu}(r)$. **A)** Two static states with D_{slow} fixed at 0.1 μm^2/s (corresponding to the estimated 70S ribosome diffusion coefficient). Best-fit D_{fast} and fractions as shown yield χ_v^2 = 2.5, indicating a very poor fit. **B)** Single static state. The minimum χ_v^2 is 9.7, corresponding to D_{fit} = 1.0 μm^2/s. **C)** Three static states D_{slow} and D_{fast} fixed at 0.1 and 4.9 μm^2/s respectively. Best-fit D_{medium} and fractions as shown. The minimum χ_v^2 is 1.25, which is not an improvement over the best two-state model of Fig. 2.3.

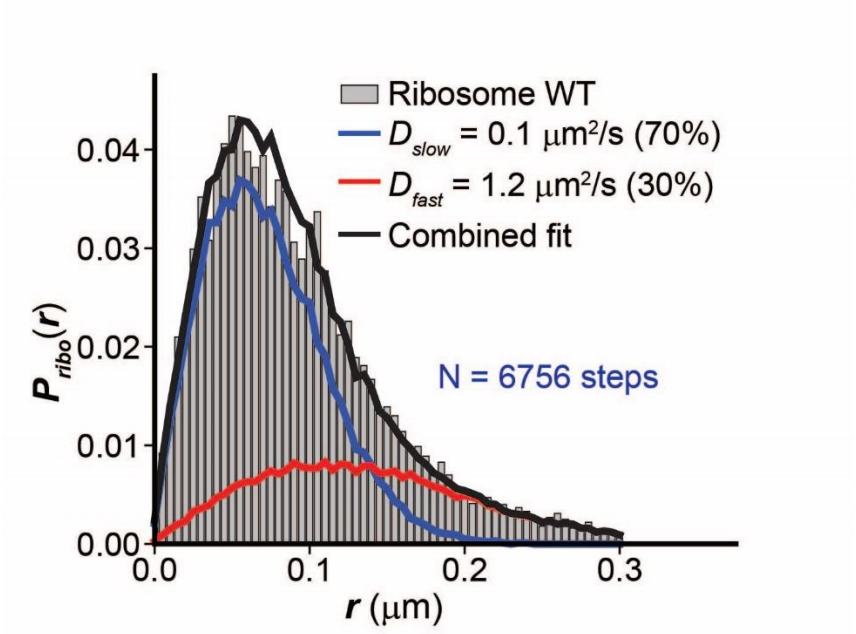

Figure A2.2. The single-step displacement probability distribution $P_{ribo}(r)$ for 30S ribosomal subunits labeled by the protein S2–Eos2. Best-fit model of two static states as shown. The slow fraction (blue; f_{slow} = 0.7, D_{slow} = 0.1 μm^2/s) is assigned to translating 70S ribosomes. The fast fraction (red; f_{fast} = 0.3, D_{fast} = 1.2 μm^2/s) is assigned to free 30S subunits.

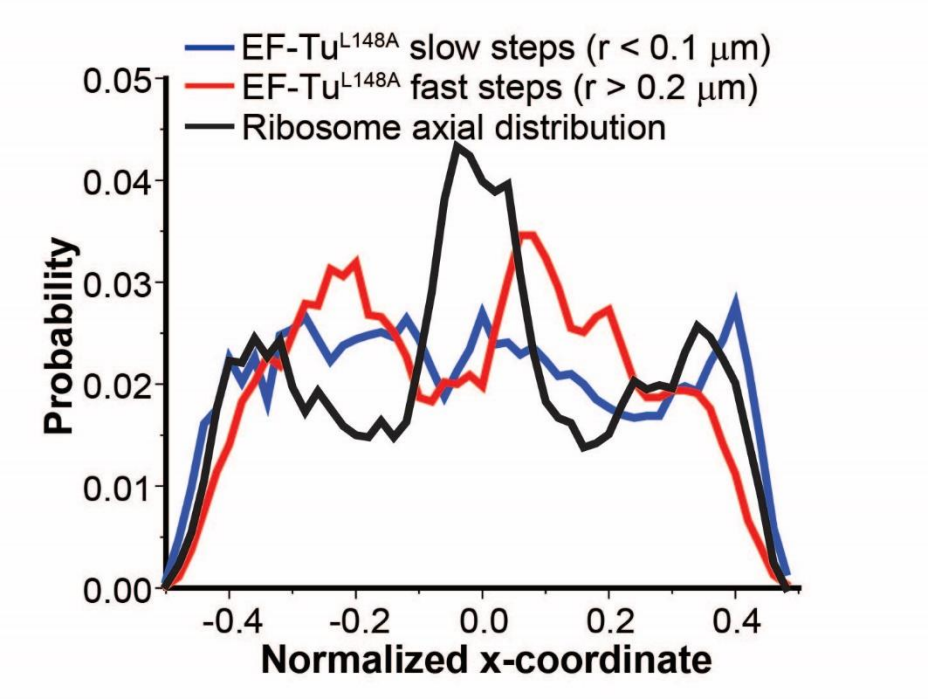

Figure A2.3. The axial distribution of slow and fast single steps for mutant protein EF-Tu^{L148A}. Slow and fast steps are based on the same cutoffs used for WT EF-Tu. The axial coordinates are normalized to -0.5 to 0.5. The slow distribution (blue; r < 0.1 μm) seems fairly homogeneous but the fast distribution (red; r > 0.2 μm) shows two distinct peaks near the DNA regions. The ribosome axial distribution (black) is also plotted for comparison.

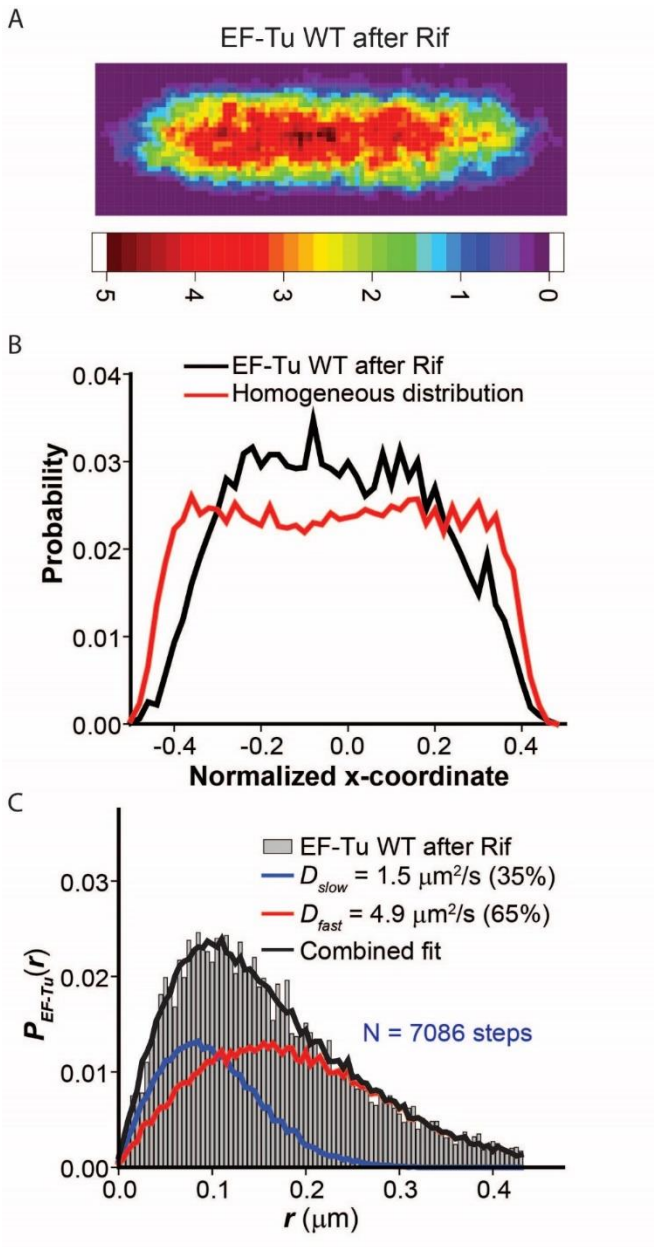

Figure A2.4. A) The spatial distribution heat map of EF-Tu after Rif treatment is shown for *E. coli* cells of 3-4 μm length. Scale is proportional to the counts per pixel. **B)** Axial distribution of EF-Tu after Rif treatment (black) along with a simulated homogeneous distribution (red). **C)** $P_{EF\text{-}Tu}(r)$ distribution of 7086 steps for EF-Tu after Rif treatment, along with the best-fit parameters for a model of two static states.

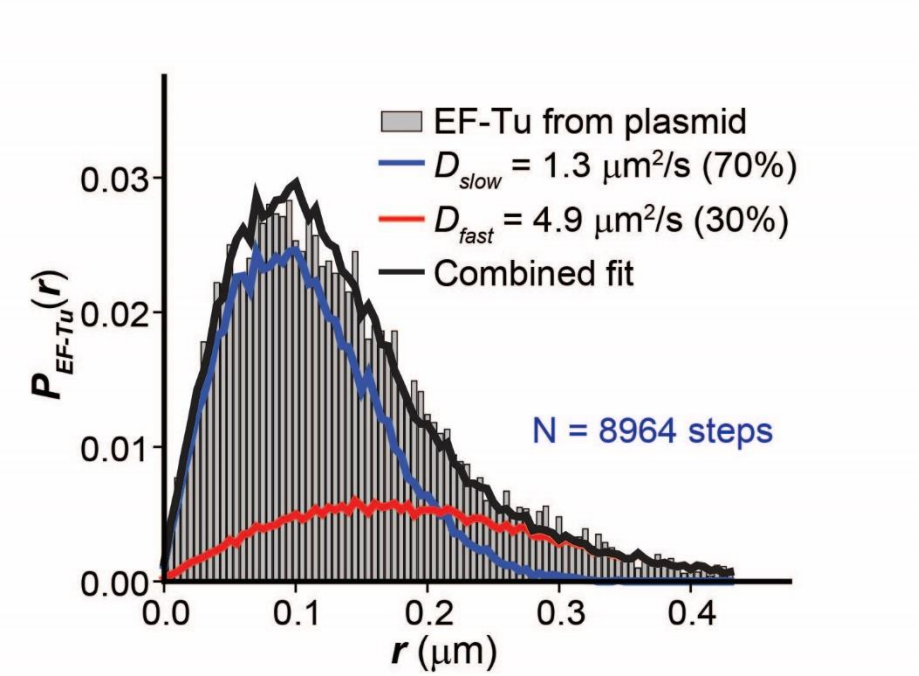

Figure A2.5. Single-step displacement probability distribution $P_{EF\text{-}Tu}(r)$ for EF-Tu expressed from a plasmid. The best-fit two-state model parameters are: (blue curve) f_{slow} = 0.7, D_{slow} = 1.3 μm^2/s; (red curve) f_{fast} = 0.3, D_{fast} = 4.9 μm^2/s. The diffusion of WT EF-Tu expressed from a plasmid is similar to the diffusion of WT EF-Tu expressed from the chromosome (Fig. 2.3).

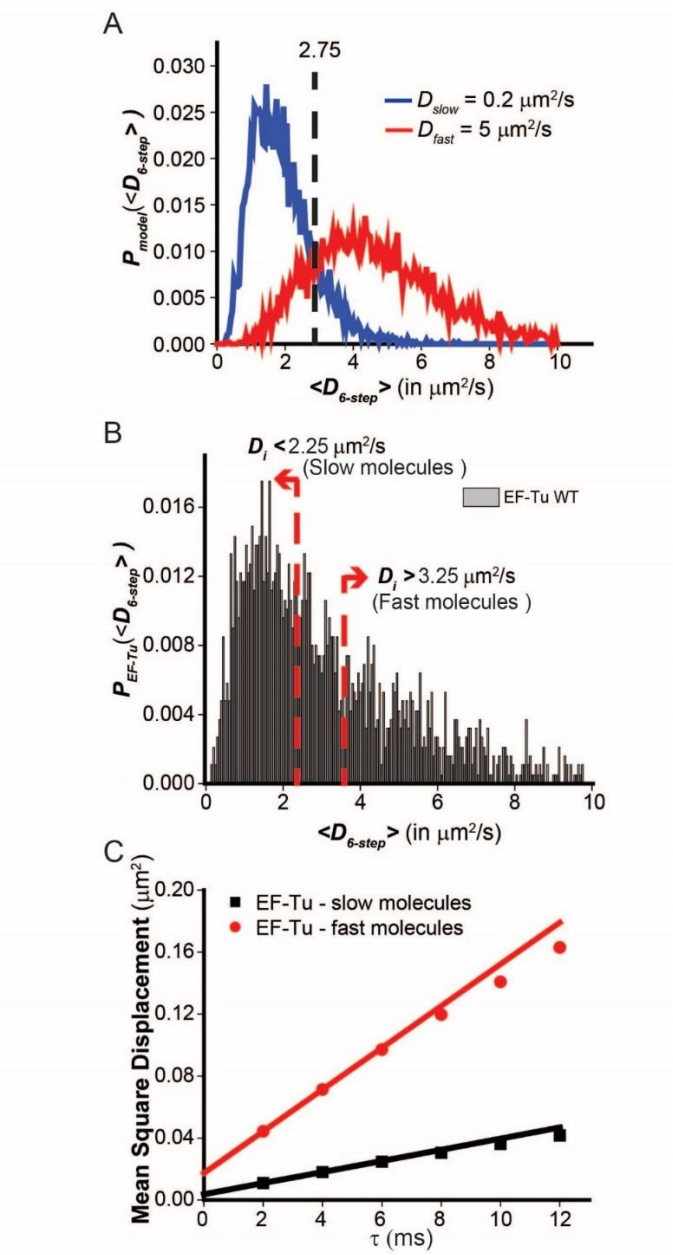

Figure A2.6. A) Simulated distributions of the mean of six single-step estimates of the diffusion coefficient, $P_{model}(D_i)$ for two diffusion coefficients, D_{slow} and D_{fast} as indicated. These distributions were used to estimate cutoff values for slow and fast copies of EF-Tu, whose experimental distribution is shown in panel **B). C)** Separate MSD plots for slow and fast EF-Tu copies. Intercepts were used to set different values of localization error: σ_{slow} = 40 nm and σ_{fast} = 80 nm.

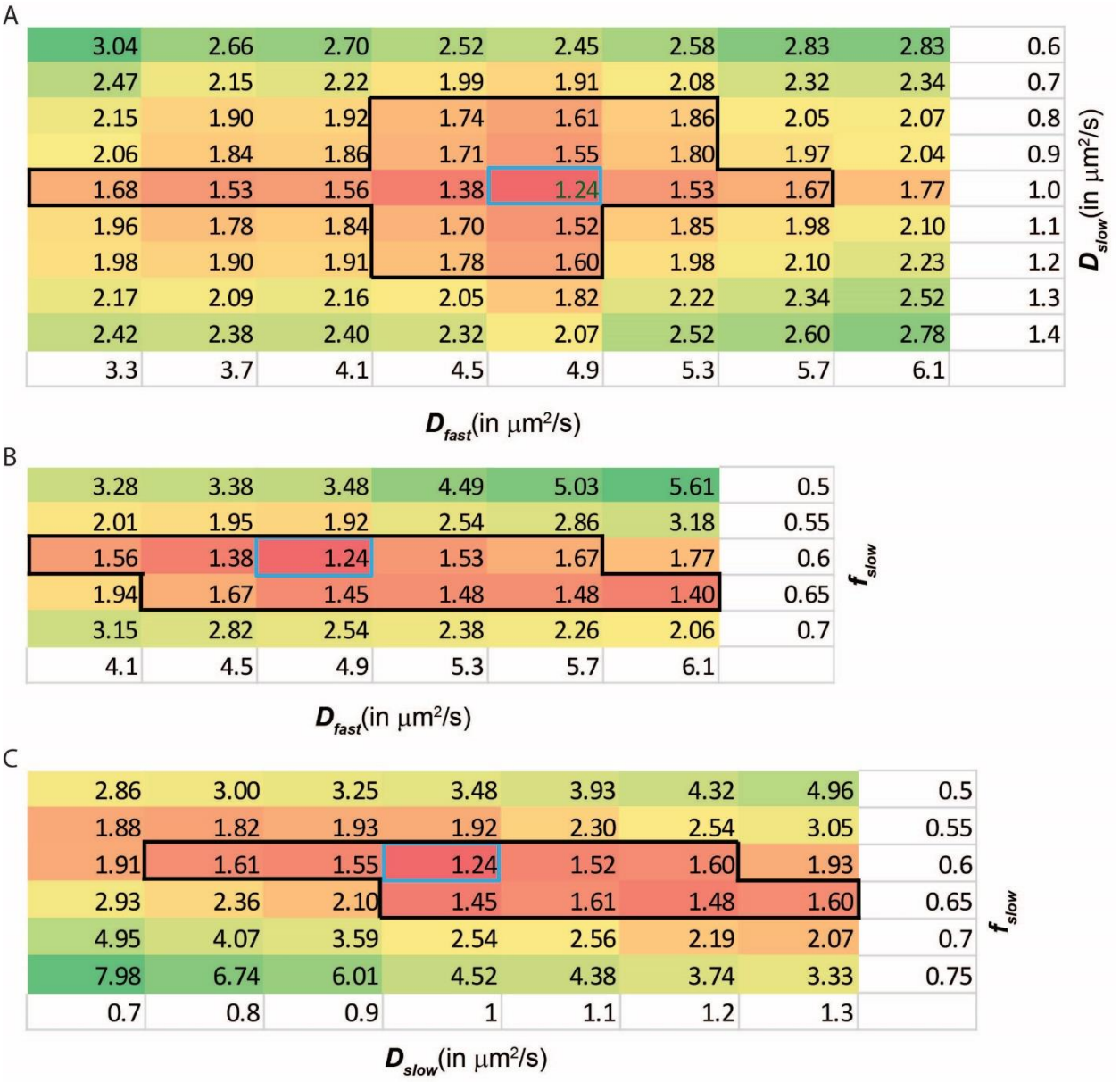

Figure A2.7. Planes passing through the three-dimensional grid search for the best χ_v^2 value for the two-state fits to WT EF-Tu distribution $P_{EF\text{-}Tu}(r)$ of Fig. 2.3. Each slice shows a plane passing through the global minimum parameter set: **A)** f_{slow} is fixed at 0.60. **B)** D_{slow} is fixed at 1.0 μm^2/s. **C)** D_{fast} is fixed at 4.9 μm^2/s. The uncertainty estimate for each parameter was chosen to enclose all values of χ_v^2 within 0.5 units of the minimum value, as shown by the boxed-in regions of each plane. Fits with still larger values of χ_v^2 were judged to be qualitatively poor.

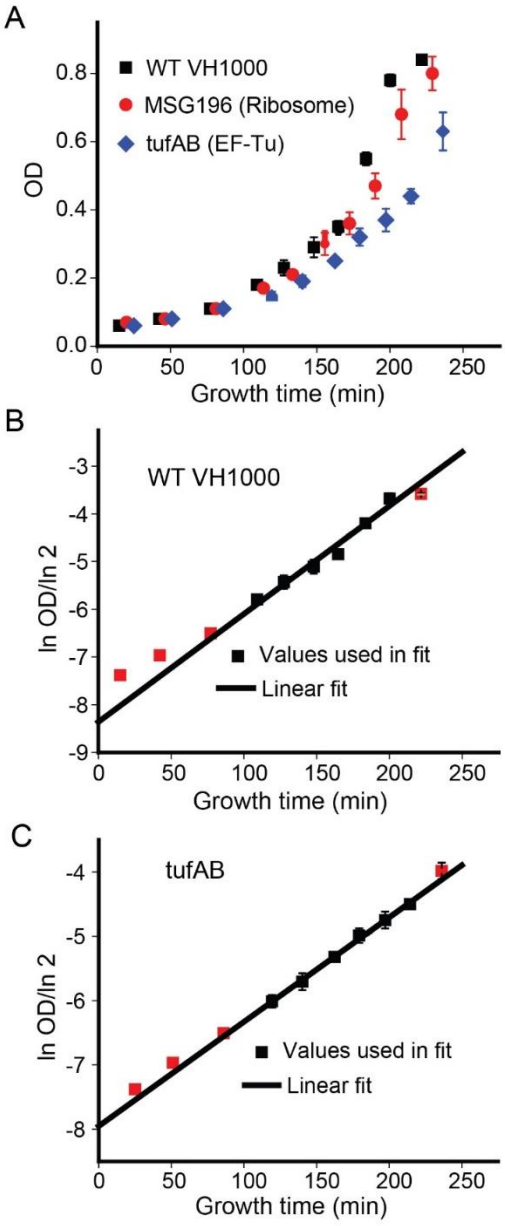

Figure A2.8. A) Growth curves in EZRDM at 30°C for three different strains: VH1000 (WT parent strain, no labeling), MSG195 (VH1000 with ribosomal protein S2 labeled with mEos2), and tufAB (*tufA* and *tufB* both labeled with mEos2). The exponential phase data points are used to calculate the doubling times. **B)** and **C)** Plots of ln OD/ln 2 vs time for the VH1000 and tufAB strains, respectively. The exponential phase data points are fitted to a straight line whose inverse slope yields the doubling times of 45 ± 2 min for VH1000 and 60 ± 3 min for tufAB.

Supplemental References

1. Michalet X. 2010. Mean Square Displacement Analysis of Single-Particle Trajectories with Localization Error: Brownian Motion in Isotropic Medium. Phys Rev E Stat Nonlin Soft Matter Phys 82:041914-041914.

2. Thompson RE, Larson DR, Webb WW. 2002. Precise nanometer localization analysis for individual fluorescent probes. Biophys J 82:2775-2783.

3. Nenninger A, Mastroianni G, Mullineaux CW. 2010. Size dependence of protein diffusion in the cytoplasm of *Escherichia coli*. J Bacteriol 192:4535-40.

4. Bakshi S, Bratton BP, Weisshaar JC. 2011. Subdiffraction-limit study of Kaede diffusion and spatial distribution in live *Escherichia coli*. Biophys J 101:2535-44.

5. Mohapatra S, Choi H, Ge X, Sanyal S, Weisshaar JC. 11 May 2017. Spatial Distribution and Ribosome-binding Dynamics of EF-P in Live *E. coli*. mBio doi:10.1128/mBio.00300-17.

6. Chen T-Y, Santiago AG, Jung W, Krzemiński Ł, Yang F, Martell DJ, Helmann JD, Chen P. 2015. Concentration- and chromosome-organization-dependent regulator unbinding from DNA for transcription regulation in living cells. Nat Commun 6:7445.

7. Plochowietz A, Farrell I, Smilansky Z, Cooperman BS, Kapanidis AN. 2017. In vivo single-RNA tracking shows that most tRNA diffuses freely in live bacteria. Nucleic Acids Res 45:926-937.

8. Rudorf S, Thommen M, Rodnina MV, Lipowsky R. 2014. Deducing the kinetics of protein synthesis in vivo from the transition rates measured in vitro. PLoS Comput Biol 10:e1003909.

9. Maloy S, V. Stewart, and R. Taylor. 1996. Genetic analysis of pathogenic bacteria. Cold Spring Harbor Laboratory Press, NY.

10. Bakshi S, Choi H, Weisshaar JC. 2015. The spatial biology of transcription and translation in rapidly growing *Escherichia coli*. Front Microbiol 6:636.

11. Schmidt A, Kochanowski K, Vedelaar S, Ahrne E, Volkmer B, Callipo L, Knoops K, Bauer M, Aebersold R, Heinemann M. 2016. The quantitative and condition-dependent *Escherichia coli* proteome. Nat Biotechnol 34:104-10.

12. Klumpp S, Scott M, Pedersen S, Hwa T. 2013. Molecular crowding limits translation and cell growth. Proc Natl Acad Sci U S A 110:16754-9.

13. Diaconu M, Kothe U, Schlunzen F, Fischer N, Harms JM, Tonevitsky AG, Stark H, Rodnina MV, Wahl MC. 2005. Structural basis for the function of the ribosomal L7/12 stalk in factor binding and GTPase activation. Cell 121:991-1004.

14. Voorhees RM, Ramakrishnan V. 2013. Structural basis of the translational elongation cycle. Annu Rev Biochem 82:203-36.

15. Savelsbergh A, Mohr D, Kothe U, Wintermeyer W, Rodnina MV. 2005. Control of phosphate release from elongation factor G by ribosomal protein L7/12. EMBO J 24:4316-4323.

16. Savelsbergh A, Mohr D, Wilden B, Wintermeyer W, Rodnina MV. 2000. Stimulation of the GTPase Activity of Translation Elongation Factor G by Ribosomal Protein L7/12. J Biol Chem 275:890-894.

17. Dong H, Nilsson L, Kurland CG. 1996. Co-variation of tRNA Abundance and Codon Usage in *Escherichia coli* at Different Growth Rates. J Mol Biol 260:649-663.

18. Uemura S, Aitken CE, Korlach J, Flusberg BA, Turner SW, Puglisi JD. 2010. Real-time tRNA transit on single translating ribosomes at codon resolution. Nature 464:1012-7.

19. Chen C, Stevens B, Kaur J, Smilansky Z, Cooperman BS, Goldman YE. 2011. Allosteric vs. spontaneous exit-site (E-site) tRNA dissociation early in protein synthesis. Proc Natl Acad Sci U S A 108:16980-5.

20. Abdulkarim F, Ehrenberg M, Hughes D. 1996. Mutants of EF-Tu defective in binding aminoacyl-tRNA. FEBS Letters 382:297-303.

21. Phillip Y, Schreiber G. 2013. Formation of protein complexes in crowded environments – From in vitro to in vivo. FEBS Letters 587:1046-1052.

22. Dill K, Bromberg S. 2010. Molecular Driving Forces: Statistical Thermodynamics in Biology, Chemistry, Physics, and Nanoscience. Garland Science.

23. Reeh S, Pedersen S. 1978. Regulation of *Escherichia coli* elongation factor synthesis *in vivo*. Gene Expression (11th FEBS Meeting Copenhagen 1977), eds Clark BFC, Klenow H, Zeuthen J (Pergamon, Oxford),:89–98.

Chapter 3:

Near Saturation of Ribosomal L7/L12 Binding Sites with Ternary Complexes in Slowly Growing *E. coli*

Reproduced verbatim from:

Mustafi M, Weisshaar JC. Near Saturation of Ribosomal L7/L12 Binding Sites with Ternary Complexes in Slowly Growing *E. coli*. Journal of molecular biology. 2019;431:2343-53.

3.1 Abstract

For *E. coli* growing rapidly in rich medium at 37°C, the doubling time can be as short as ~20 min and the average rate of translation (k_{trl}) can be as fast as ~20 amino acids/s. For slower growth arising from poor nutrient quality or from higher growth osmolality, k_{trl} decreases significantly. In earlier work from the Hwa lab, a simplified Michaelis-Menten model suggested that the decrease in k_{trl} arises from a shortage of ternary complexes (TCs) under nutrient limitation and from slower diffusion of TCs under high growth osmolality. Here we present a single-molecule tracking study of the diffusion of EF-Tu in *E. coli* growing with doubling times in the range 62-190 min at 37°C due to nutrient limitation, high growth osmolality, or both. The diffusive properties of EF-Tu remain quantitatively indistinguishable across all growth conditions studied. Dissection of the total population into ribosome-bound and free sub-populations, combined with copy number estimates for EF-Tu and ribosomes, indicates that in all cases ~3.7 EF-Tu copies are bound on average to each translating 70S ribosome. Thus the four L7/L12 binding sites adjacent to the ribosomal A-site in *E. coli* are essentially saturated with TCs in all conditions, facilitating rapid testing of aminoacyl tRNAs for a codon match. Evidently the average translation rate is not limited by either the supply of cognate ternary complexes under nutrient limitation or by the diffusion of free ternary complexes at high osmolality. Some other step or steps must be rate limiting for translation in slow growth.

Keywords: Nutrient limitation; high osmolality; superresolution microscopy; ternary complex; diffusion.

Abbreviations: EF-Tu, elongation factor-Tu; aa-tRNA, aminoacyl-tRNA; TC, ternary complex; WT, wild type; MBM, MOPS based minimal medium.

3.2 Introduction

Bacterial cells including *E. coli* are remarkable for their ability to survive and grow under a wide range of environmental conditions [1-5]. A fundamental quantity closely related to growth rate is the average rate of protein synthesis by translating 70S ribosomes, defined as the mean rate of amino acid incorporation into the growing polypeptide chain (here k_{trl}, in aa/s). The translation elongation cycle comprises a complex series of molecular level events including binding of a ternary complex (TC) to an L7/L12 tether adjacent to the ribosomal A-site; testing of the aminoacyl tRNA (aa-tRNA) at the A-site for a codon match; rejection and dissociation of non-matching TCs; formation of a new peptide bond to the correct amino acid; and translocation of the tRNAs through the ribosomal A-, P-, and E-sites [6, 7]. Each TC contains an aa-tRNA, the translation elongation factor EF-Tu, and GTP. For *E. coli*, many rate constants for individual steps of the elongation cycle have been elucidated by careful kinetic studies *in vitro*, both in bulk and at the single molecule level [7-10]. Detailed kinetics models that are consistent with observed average translation rates *in vivo* have been developed [11, 12]. In addition, models incorporating codon-specific elongation rates have been proposed to help explain the effects of depletion of specific TCs under external perturbations [13].

Two important environmental stresses that can severely hinder bacterial growth are nutrient limitation and hyperosmotic stress. In a comprehensive series of papers, Hwa and coworkers have made detailed measurements of the factors governing k_{trl} in live *E. coli* over a wide range of growth rates [14-16]. They explored the effects of nutrient limitation and hyperosmotic stress on the overall growth rate λ, on k_{trl}, on the fraction of the proteome dedicated to ribosomal proteins, on the copy number of the elongation factor EF-Tu relative to that of ribosomes, on the fraction of ribosomes actively carrying out translation, and on the fraction of tRNA copies charged as

aa-tRNA. Remarkably, the data under nutrient limitation [14] with doubling times ranging from 23 min to 20 hr fit a simplified, coarse-grained Michaelis-Menten model involving the cognate ternary complex as substrate and the ribosome as enzyme:

$$\frac{1}{k_{trl}} = \frac{1}{k_{\mathrm{on}} \times [\mathrm{TC}_{\mathrm{eff}}]} + \frac{1}{k_{\mathrm{elong}}} \quad (1)$$

Here k_{on} (M^{-1}-s^{-1}) is the bimolecular rate constant for binding of cognate ternary complexes to the ribosomal A-site (assumed to be diffusion limited), $[TC_{eff}]$ is the concentration of cognate ternary complexes, and k_{elong} (s^{-1}) is the composite rate of all subsequent steps in peptide synthesis. As nutrient quality decreases, the growth rate slows down and the fraction of protein synthesis dedicated to ribosomal proteins decreases. Synthesis of EF-Tu and ribosomal proteins are co-regulated; the ratio of total EF-Tu to ribosomes always lies in the range 6–7 [14-18]. Accordingly, the falloff in k_{trl} as growth rate decreases was judged to arise primarily from a decrease in $[TC_{eff}]$, *i.e.,* from limitations on the substrate concentration, with k_{on} and k_{elong} remaining essentially constant. Sub-lethal doses of the translation inhibitor chloramphenicol (Cm) were also used in order to vary $[TC_{eff}]$ under fixed nutrient conditions. This enhances the fraction of proteins dedicated to ribosomes, and the TC and aa-tRNA concentrations increase proportionally. The Cm data fell on the same Michaelis-Menten plot.

In a more recent study [16], the same quantities were measured using glucose as carbon source in minimal MOPS-buffered medium (MBM) while varying the overall concentration of the impermeable osmolite NaCl in the medium. As the NaCl concentration increased from 0.1 M to 0.6 M, the doubling time at 37°C varied from 43 to 346 min. At each of two elevated NaCl concentrations 0.3 M and 0.4 M, the effective substrate concentration $[TC_{eff}]$ was varied at fixed osmolality by addition of sublethal concentrations of Cm. Lineweaver-Burke plots of k_{trl}^{-1} vs

$[TC_{eff}]^{-1}$ then indicated that while the maximum elongation rate k_{elong} remained fairly constant with increasing osmolality (22–25 aa/s), the binding rate constant k_{on} decreased by a factor of 2.3, from 6.4 x 10^6 $M^{-1}s^{-1}$ at 0.1 M NaCl to 2.8 x 10^6 $M^{-1}s^{-1}$ at 0.4 M NaCl. This decrease was attributed to slower diffusion of ternary complexes in the more crowded cytoplasm at higher osmolality. In summary, Hwa and coworkers conclude that the decrease in overall translation rate under nutrient limitation arises primarily from the scarcity of ternary complexes. The decrease at higher osmolarity arises primarily from increased cytoplasmic crowding, which limits the diffusion coefficient of ternary complexes and thus k_{on}.

We recently reported a single-molecule tracking study of the diffusion of EF-Tu in live *E. coli* growing in EZ rich defined medium (EZRDM) at 30°C (doubling time 60 min) [19]. Analysis of the diffusive trajectories enabled us to distinguish two EF-Tu sub-populations: a slowly diffusing component assigned to EF-Tu copies within ternary complexes bound to translating ribosomes and a more rapidly diffusing component assigned as a composite of free EF-Tu copies and free ternary complexes (not bound to ribosomes). The localization uncertainty $\sigma \sim 40$ nm makes the method insensitive to the internal motion of an EF-Tu copy tethered to an L7/L12 site. The measurements are only sensitive to the overall movement through space of the ribosome-bound EF-Tu, regardless of its binding state. From the fractions of slow and fast diffusive components and the known ratio of 6–7 EF-Tu copies per ribosome, we inferred that on average, approximately 4 ternary complexes are bound to each translating ribosome. Before an aa-tRNA can be tested at the A-site, its ternary complex binds to the CTD of an L7/L12 ribosomal subunit (schematic in Fig. 3.1A) [20-24]. In *E. coli*, four such L7/L12 subunits protrude from the ribosomal stalk adjacent to the A-site [20]. Our quantitative estimate thus indicated that the four L7/L12 subunits are essentially saturated with ternary complexes in

moderately good growth conditions at 30°C. The presence of four TCs on flexible linkers near the A-site presumably facilitates rapid testing of new TCs for a codon match [20].

In view of Hwa's work, here we extend our studies of EF-Tu diffusion to include slower growth (doubling times 62–190 min) at 37°C arising from the effects of either nutrient limitation or hyperosmotic conditions or both. The diffusion coefficients of fast and slow EF-Tu copies remain quite similar under all conditions studied. In all cases, the data indicate that the four L7/L12 sites remain essentially saturated with ternary complexes. Evidently neither the concentration of TCs under nutrient limitation nor the diffusion coefficient of TCs in hyperosmotic conditions limits the overall translation rate.

3.3 Results

3.3.1 Comparison of EF-Tu/ternary complex diffusion under different osmotic conditions.

We used the superresolution technique of photoactivated localization microscopy (PALM) [25] and single-particle tracking (SPT) [26] to probe the diffusion of EF-Tu in *E. coli* under various growth conditions having different translation elongation rates. EF-Tu is an essential protein. The background, wild-type strain (WT) is *E. coli* NCM3722. We used a modified strain in which the C-termini of the two genes encoding EF-Tu, *tufA* and *tufB* [27], are both fused within the chromosome to the gene expressing the photoconvertible fluorescent protein mEos2. Thus all expressed copies carry the mEos2 label.

To vary the growth rate and also the elongation rate, we have grown cells in MOPS based minimal growth medium (MBM) with glucose or acetate as the carbon source and with varying osmolality, ranging from 0.28-0.81 Osm. The osmolality was varied by including different concentrations of NaCl (0.1 M and 0.4 M) in the growth medium. Cells were grown at 37°C. Under these growth conditions, the doubling time varied from 62 to 190 min (Table 3.1). The

doubling time for the WT strain growing in glucose and 0.28 Osm at 37°C is 48 min compared to 62 min for the labeled strain. The labeling increases the doubling time by ~30%, a moderate growth defect. The growth curves for the different conditions are shown in Fig. A3.1. The only phenotypical change observed for the different growth conditions is a decrease in the mean cell length with decreasing growth rate (Fig. A3.2).

The superresolution imaging experiments yield trajectories of the labeled EF-Tu molecules. EF-Tu may occur as freely diffusing bare EF-Tu, EF-Tu within freely diffusing ternary complexes, or EF-Tu within ternary complexes bound to translating 70S ribosomes. The diffusion of free EF-Tu-mEos2 (~69 kDa) [28, 29] and free ternary complex-mEos2 (~93 kDa) are not readily distinguished from one another by short trajectories having significant localization error. Thus we refer to these two populations combined as “fast EF-Tu”. A free protein of similar size should have a diffusion coefficient in the range 4-8 $\mu m^2/s$ [30, 31]. Accordingly, we recently reported the diffusion coefficient of the fast EF-Tu population to be $D_{fast} = 4.9 \pm 1.2$ $\mu m^2/s$ for VH1000 cells growing in EZRDM at 30°C [19]. The 70S ribosome/polysome complexes are much larger than a ternary complex (~2.5 MDa for each 70S ribosome) [32, 33]. The diffusion coefficient of ribosome-bound ternary complexes should be the same as that of the 70S-polysomes, ~0.3 $\mu m^2/s$ [19, 34, 35]. This population is referred to as “slow EF-Tu”. By modeling the distribution of single-step displacements, we obtain quantitative estimates of the fractional populations of fast and slow states of EF-Tu in each growth condition.

We imaged the EF-Tu-mEos2 molecules in a widefield epifluorescence mode. Only a small subset of fluorophores (~1/frame) were activated using a weak 405 nm laser and those molecules were subsequently excited by a 561 nm laser to observe their fluorescence. The locations of these molecules were recorded and then connected over successive frames to form

trajectories. The mean trajectory length was ~3 steps. Imaging was carried out at the fast rate of 2 ms/frame with continuous laser illumination, in order to capture slow and fast EF-Tu copies with similar efficiency. For each of the conditions studied, we analyzed between 1400-2100 trajectories of six steps or longer duration. These trajectories were truncated at the sixth step.

We first present a detailed quantitative analysis of EF-Tu diffusion and fractional binding to translating ribosomes for cells grown in MBM glucose medium with 0.1 M NaCl. There follows a comparison of the results across different growth media.

3.3.2 MBM-glucose growth medium with 0.1 M NaCl. The mean diffusion coefficient D_{Mean} of EF-Tu in each growth condition is obtained from the mean-square displacement (MSD) plot vs lag time (Fig. 3.2A). In our previous study of the VH1000 strain grown in the moderately rich growth medium EZRDM at 30°C [19], we obtained $D_{Mean} = 2.02 \pm 0.19$ μm^2/s, a useful reference number. The present study at 37°C finds only minor differences in D_{mean} across the different growth conditions (Table 3.1). In particular, $D_{mean} = 1.84 \pm 0.19$ μm^2/s for MBM-glucose with 0.1 M NaCl. In each case, the intercept of the MSD plot yields an estimate of the localization error σ, which is typically ~60 nm.

To study the binding of EF-Tu to ribosomes, we used the same set of 6-step trajectories to form a histogram of the distribution of single-step displacements between camera frames, with each step corresponding to a time delay of $\Delta t = 2$ ms. The resulting distribution is normalized to obtain $P_{EF\text{-}Tu}(r)$, as shown in Fig. 3.2B for cells growing in MBM-glucose with 0.1 M NaCl. To analyze this distribution as a sum of contributions from fast and slow EF-Tu copies, we simulate large sets of random walk trajectories in a confining volume which matches the dimensions of an average *E. coli* cell growing in each specific growth condition. Each set uses a particular diffusion coefficient *D* and includes appropriate localization error, as judged from the

intercept of the MSD plot. Each value of D yields a simulated numerical distribution of single-step displacements $P_{model}(r; D)$. These serve as basis functions for two-state fitting of the experimental $P_{EF\text{-}Tu}(r)$ in a least-squares sense. We combine pairs of these simulated distributions representing the fast (D_{fast}) and slow (D_{slow}) populations in varied fractions (f_{slow} and $f_{fast} = 1 - f_{slow}$) to determine the best numerical fit to the experimental $P_{EF\text{-}Tu}(r)$ distribution. The goodness of fit is judged by the reduced chi-square statistic, χ_v^2. For each growth condition, we generate a three-dimensional grid of χ_v^2 values for different choices of D_{slow}, D_{fast} and f_{slow}. The parameters which give the minimum χ_v^2 are chosen as our best-fit parameters. The procedure is explained in more detail in Methods and in references [19, 34].

For MBM-glucose with 0.1 M NaCl, this procedure yields the best-fit values $D_{slow} = 1.35 \pm 0.30$ μm^2/s, $D_{fast} = 3.7 \pm 1.1$ μm^2/s, and $f_{slow} = 0.67 \pm 0.05$, with $\chi_v^2 = 1.07$ (Table 3.1). The uncertainties are estimated from the range of parameter values that would increase χ_v^2 by 0.5 from its best-fit value. These results are very similar to those obtained earlier for the strain VH1000 in EZRDM at 30°C [19]. In that case, we obtained the values $D_{slow} = 1.0 \pm 0.2$ μm^2/s, $D_{fast} = 4.9 \pm 1.2$ μm^2/s, and $f_{slow} = 0.60 \pm 0.05$. One-state fitting to the same data yields only very poor fits; the best value of χ_v^2 was 4.8 (SI, Table A3.3). We also explored three-state fitting of the same $P_{EF\text{-}Tu}(r)$ distribution with D_{slow} constrained to the ribosome value of 0.3 μm^2/s and D_{medium}, D_{fast} and the fractional populations f_{slow} and f_{medium} as adjustable parameters, making a four-dimensional search grid. This fixes $f_{fast} = (1 - f_{slow} - f_{medium})$. The results are detailed in Table A3.2. The best three-state fit gave $\chi_v^2 = 1.02$, only a marginal improvement over the best two-state fit. In all four growth conditions, two-state and three-state fits gave quite similar fractions f_{fast} and diffusion coefficients D_{fast}.

As in the earlier study of the VH1000 strain growing in EZRDM at 30°C [19], D_{slow} is ~5 times larger than the 70S polysome diffusion coefficient of $D_{polysome}$ = 0.3 ± 0.1 μm^2/s. Once again we infer that D_{slow} represents a composite diffusive state. The typical binding time of a ternary complex to the translating ribosome is evidently shorter than one camera frame = 2 ms, so that D_{slow} represents a weighted average over a mixture of bound and free populations. In the earlier study [19] we showed that the spatial distribution of the slow population indeed mimics the three-peaked distribution of the ribosomes [36, 37], most of which are translating at a given moment. Such a short binding time is consistent with the fast overall elongation rates of ~20 amino acids per second and the need to test ~40 aa-tRNAs on average to find a codon match [11, 38]; see Discussion.

In the present case of MBM-glucose with 0.1 M NaCl, in order to match D_{slow} = 1.35 ± 0.3 μm^2/s, the slow population must be a mixture of 69 ± 13% ribosome-bound and 31 ± 13% free copies. This estimate assumes that free ternary complexes within the ribosome-rich regions diffuse with D_{fast} = 3.7 μm^2/s. The conclusion is that at any given moment, 46 ± 9% of the entire EF-Tu population comprises ternary complexes bound to translating ribosomes: this is 0.69 of the 67 ± 5% of copies exhibiting the slow apparent diffusion coefficient D_{slow}.

We can leverage this result to provide a quantitative estimate of the mean number of EF-Tu copies (ternary complexes) bound to each translating ribosome. In all conditions studied here, including MBM-glucose with 0.1 M NaCl, Hwa and others [14, 16, 18] have found that the total copy number of EF-Tu is 6 to 7 times greater than the total copy number of ribosomes. In addition, for MBM-glucose with 0.1 M NaCl, only 85 ± 5% of ribosomes occur as translating 70S copies [14]. From Eq. 4 in Methods, we conclude that on average, the mean number of

EF-Tu bound as ternary complexes to each translating ribosome is $N_{EF\text{-}Tu/70S} = 3.5 \pm 0.8$. That is, the four L7/L12 stalk proteins are essentially saturated with ternary complexes. The overall uncertainty comes from propagating uncertainties in each factor in Eq. 4.

Alternatively, we can obtain an analogous estimate of $N_{EF\text{-}Tu/70S}$ using the three-state fitting results of Table A3.2. Details are provided in the Methods section. Here we assume that f_{slow} arises from a population of ternary complexes that remain ribosome-bound for the entire 2 ms frame duration, f_{medium} is a composite population that makes bound-free transitions during the 2 ms frame time, and f_{fast} arises from freely diffusing copies. For MBM with 0.1 M NaCl, the result is $N_{EF\text{-}Tu/70S} = 3.5$, the same as that obtained from the two-state fits.

3.3.3 Comparisons across different nutrient and osmotic conditions. For the higher salt condition MBM-glucose with 0.4 M NaCl (doubling time 104 min), $D_{Mean} = 1.79 \pm 0.16$ μm^2/s from the MSD plot (Fig. 3.2A), essentially the same as for 0.1 M NaCl. The distributions $P_{EF\text{-}Tu}(r)$ for the two salt conditions are compared directly in Fig. 3.3A, and the two-state decomposition for

0.4 M NaCl is shown in Fig. 3.3B. The two-state fitting procedure yields $D_{slow} = 1.0 \pm 0.1$ μm^2/s, $D_{fast} = 3.5 \pm 1.0$ μm^2/s, and $f_{slow} = 0.65 \pm 0.05$. The raw data and the numerical fitting results are quite similar for the two osmotic conditions, although the doubling time has increased by a factor of 1.65, from 62 min at low salt to 104 min at high salt. For glucose medium at higher salt, the same procedure yields $N_{EF\text{-}Tu/70S} = 3.9 \pm 0.6$ for the estimated number of ternary complexes bound to each translating ribosome.

Still slower doubling times are achieved by changing the growth medium to MBM-acetate with 0.1 M or 0.4 M NaCl, resulting in doubling times of 101 and 190 min, respectively. The values of D_{mean} from MSD plots and the best-fit two-state diffusion coefficients remain quite

similar to those in glucose (Table 3.1). In addition, the estimated number of ternary complexes bound to each translating ribosome remains high, $N_{EF\text{-}Tu/70S}$ = 3.6 ± 0.7 and 3.9 ± 0.7, respectively. For all these cases, the measured distributions $P_{EF\text{-}Tu}(r)$ and the best two-state fits are presented in Figs. A3.3 and A3.4. The numerical results are summarized in Table 3.1 and 3.2.

The Appendix also summarizes the best three-state fits in each case. In all four growth conditions, the three-state fits yield estimates for $N_{EF\text{-}Tu/70S}$ that lie within 10% of the estimates from two-state fits. The conclusion that the four L7/L12 sites are essentially saturated with ternary complexes under all four growth conditions is robust.

Finally, we re-state a control from the earlier study [19] that demonstrates that our analysis does not always find ~4 bound EF-Tu per 70S ribosome. There we expressed a mEos2-labeled EF-Tu^{L148A} mutant from a plasmid and measured its diffusive properties. Rodnina lab [21] has shown that this mutation causes weaker binding to L7/L12. Accordingly, the same analysis procedure yielded the result of 1.8 bound EF-Tu^{L148A} per 70S ribosome. When mEos2-labeled WT EF-Tu was expressed from an analogous plasmid, we recovered the result of ~4 bound EF-Tu copies per 70S ribosome.

3.4 Discussion

It is important to recognize that these measurements locate and track EF-Tu copies, not ternary complexes *per se*. In live *E. coli*, EF-Tu can occur as bare EF-Tu or as EF-Tu within a charged ternary complex (aa-tRNA–EF-Tu–GTP). In our earlier study in EZRDM, we used *in vitro* binding constants to estimate that in *E. coli* the TCs outnumber bare EF-Tu copies by about a factor of 2.2 (~70% of all EF-Tu present as TCs). Our data do not directly demonstrate that the slowly diffusing component involves ternary complexes bound to ribosomes. *In vitro* kinetics

studies have shown that both bare EF-Tu [39] and TCs [21, 22, 40] bind to 70S ribosomes. However, in similar conditions *in vitro*, k_{on} is about 1000 times larger for TCs [41] than for bare EF-Tu [39]. This indicates that an empty L7/L12 site will almost always capture a TC rather than a bare EF-Tu.

For a given mRNA codon waiting for arrival of a matching tRNA at the A-site, the vast majority of ternary complexes are not cognate. We previously estimated that on average ~40 TCs must be tested before finding a cognate TC [11, 38]. Thus our measurements apply to the typical event in which a mismatched TC binds to one of the L7/L12 sites, is tested for a codon match, fails the test, and dissociates from the A-site without GTP hydrolysis becoming once again a free TC. A simple model of this process for non-cognate TCs is depicted in Fig. 3.1A. As suggested before [20], the presence of four flexibly tethered L7/L12 binding sites in close proximity to the A-site may serve to capture TCs efficiently and to provide a steady supply of TCs for rapid codon testing. The average translation rate in *E. coli* can be as fast as ~20 aa/s [3, 42]. If 40 TCs on average must be tested before finding a codon match, the timescale for binding and testing an individual TC must be ~1 ms or faster. It may be much less if subsequent processing of a matching aa-tRNA takes up a substantial fraction of the elongation cycle. That estimate supports our assumption that the best-fit values of $D_{slow} \sim 1\ \mu m^2/s$ are a weighted average of diffusion while bound to the ribosome and diffusion while searching for an open L7/L12 binding site.

Across the different nutrients and different external osmolalities tested, for which the doubling time varies from 62 min to 190 min, we find no significant quantitative differences in EF-Tu/ternary complex diffusive properties. The best-fit diffusion coefficients D_{fast} of the freely diffusing component all lie in the range 3.5–4.3 $\mu m^2/s$, and they overlap each other within the

error estimates (Table 3.1). This observation is qualitatively consistent with the results of an earlier study of GFP diffusion in the cytoplasm of *E. coli* grown in MBM with glucose as carbon source and adapted to high growth osmolality induced by addition of NaCl in the medium [43]. For cells adapted to grow at 0.28 Osm and 0.65 Osm (nearly matching our two MBM/glucose conditions), the mean GFP diffusion coefficient was 13.8 ± 3.8 $\mu m^2/s$ and 13.3 ± 3.2 $\mu m^2/s$, respectively. Only at higher growth osmolality did the GFP diffusion coefficient begin to decrease, and the decrease remained quite moderate even up to 1.45 Osm.

In all growth conditions studied here, our results combined with copy number estimates from the literature indicate that the four L7/L12 stalk proteins on translating ribosomes are nearly saturated with ternary complexes. The estimates for $N_{EF\text{-}Tu/70S}$ (Table 3.2) all lie in the narrow range 3.5–3.9 and overlap each other within the error estimates. A variety of other GTPases, most importantly EF-G, but also including factors such as IF2, EF4/LepA, and RF3, must compete with EF-Tu for L7/L12 binding sites [20, 23, 44, 45]. Most of these factors exhibit *in vitro* binding constants to L7/L12 that are comparable to that of EF-Tu [23, 46]. However, it is plausible that EF-Tu will dominate occupancy of the L7/L12 sites, primarily because of the much smaller copy numbers of its competitors. For example, in glucose minimal medium, there are 6-7 EF-Tu copies per ribosome compared with only ~1 EF-G copy per ribosome [18]. This is consistent with the fact that arrival of every aa-tRNA (cognate and non-cognate) must involve TC binding to L7/L12, whereas EF-G is needed only when a cognate TC is accommodated into the A-site, a relatively rare event. In similar growth conditions, the EF-Tu copy number exceeds those of IF2, EF4/LepA, and RF3 by a factor of 200-300 [18]. Accordingly, these factors are required only for translation initiation, back-translocation, or termination, which are extremely rare events.

Finally, the copy numbers relative to ribosomes of EF-Tu (6-7), EF-G (0.8-0.9), and tRNA (~9) remain sensibly constant across all the growth conditions studied here [14, 16]. In addition, the tRNA charging levels lie in the narrow range 60-80% [14, 16]. We therefore expect the partitioning of EF-Tu copies between TCs and bare EF-Tu to be similar in all the conditions studied here. The stability of the number of bound EF-Tu per 70S ribosome across growth conditions seems consistent with that result.

The present results indicate that delivery of ternary complexes to the L7/L12 binding sites of the translating ribosome is not the rate-limiting step in the overall translation process, at least for the range of growth conditions investigated here. This conclusion disagrees with inferences drawn in the recent work from the Hwa lab. Under nutrient limitation, they concluded that the overall translation rate decreases primarily due to a shortage of ternary complexes [14]. Under hyperosmotic stress, they concluded that the translation rate decreases primarily due to enhanced crowding, which slows the diffusion-limited rate of binding of ternary complexes to the ribosomal A-site [16]. The coarse-grained Michaelis-Menten model with ribosome as enzyme and cognate ternary complexes as substrate fits the Hwa data well, but would seem to require modification.

If delivery of TCs to the L7/L12 sites is not rate limiting for the overall translation rate, what is the rate limiting step? There are many possibilities--protein synthesis is a complex, multistep process. First the 30S subunit must find a Shine-Dalgarno sequence on a message [47]. The 50S subunit must be recruited and synthesis begun with the help of the initiation factors IF1, IF2 and IF3 [48]. Each subsequent elongation cycle involves recruitment and testing of ternary complexes, accommodation of a codon-matched aa-tRNA at the A-site, formation of the new chemical bond to the growing peptide chain, and translocation of the message and the tRNAs

through the ribosome with the help of EF-G [6]. Once the chain is complete, additional factors RF1, RF2 and RF3 assist termination [49]. Our results only indicate that one or several of these many mechanistic steps becomes slower and rate limiting under both nutrient limitation and higher growth osmolality.

One common consequence of both nutrient limitation and osmotic upshift is enhanced synthesis of the "magic spot", (p)ppGpp [50-53]. *In vitro* binding studies indicate that ppGpp competes with GTP for its binding site within many GTPases, including EF-Tu within the ternary complex, EF-G, EF-Ts, the translation initiation factor IF2, and also the release factor RF3 [44, 45, 54]. A simple suggestion is that as growth slows down, one or several of these cofactors occasionally arrives at the ribosome containing ppGpp rather than GTP. For example, if a fraction of ternary complexes contained ppGpp, it would not perturb the initial TC binding step to L7/L12, because the GTP binding site is different from the L7/L12 binding site [21, 55]. However, when a cognate ternary complex arrives at the A-site, the accommodation process is driven by activation of the GTPase within the ternary complex, GTP hydrolysis, and phosphate release [6]. The overall translation rate would be suppressed if some fraction of the cognate TCs contained not GTP, but ppGpp, thus thwarting the accommodation step. This is only one of many possibilities.

3.5 Materials and Methods

3.5.1 Bacterial strains. In *E. coli*, EF-Tu is expressed from two essentially identical genes: *tufA* and *tufB.* Both of these genes were endogenously labeled at the C-terminus with a photoconvertible fluorescent protein, mEos2, via the lambda red technique [56] in the background strain NCM3722, the same strains used by the Hwa lab [14, 16]. The doubling time of the labeled strain is 62 ± 2 min compared to 48 ± 1 min for the wild-type (WT) strain, when

grown in MOPS based minimal medium (MBM) with glucose and normal osmolality (0.28 Osm) at 37°C. The labeling causes a ~30% increase in doubling time, a moderate growth defect considering that

EF-Tu is an essential protein. The growth conditions and the corresponding doubling times of the labeled EF-Tu strain are collected in Table A3.1.

3.5.2 Cell growth and preparation for imaging. The cells were grown in an air shaker (New Brunswick Excella E24, from Eppendorf) maintained at 200 rpm and 37°C. Bulk cultures from frozen glycerol stock solution were grown overnight to stationary phase in LB or LB + 0.3 M NaCl. On the following day the stationary phase culture was first washed and then again grown to stationary phase in MBM, a MOPS-buffered solution with supplemental metal ions (M2101; Teknova, contains 0.05 M NaCl), glucose (0.2% w/v) or Sodium acetate (60 mM), 1.32 mM KH_2PO4, and varying amount of NaCl. The NaCl amount was varied to obtain a final Na^+ concentration of 0.1 M or 0.4 M, yielding final osmolality of ~0.28 Osm and ~0.81 Osm, respectively. Osmolalities were measured with a Wescor Vapro 5520 vapor pressure osmometer (Wescor, Logan, UT). On the following day, the stationary phase culture was divided into subcultures with 100-fold dilution in fresh MBM with appropriate NaCl concentration and grown again to exponential phase (OD = 0.2-0.5). Cells were then plated on a polylysine coated coverslip and covered with a CoverWell perfusion chamber (Electron Microscopy Science, PA) with a well volume of 140 µL.

3.5.3 Superresolution imaging of live *E. coli* cells. The imaging and single-particle trajectory analysis were performed similarly to the method described in our previous study [19]. The cells were imaged within 5 min of plating. Individual fields of view were imaged no longer than 20 s to minimize laser damage. Each prepared sample was imaged for no longer than 30 min, during

which cells continued to grow normally. Cells were imaged on an inverted microscope (Nikon Instruments, model Eclipse-Ti, Melville, NY) equipped with an oil immersion objective (CFI Plan Apo Lambda DM 100x Oil, 1.45 NA; Nikon Instruments), a 1.5x tube lens, and the Perfect Focus System (Nikon Instruments, Melville, NY). The fluorescence images were recorded on a back-plane illuminated electron-multiplying charge-coupled device (EMCCD) camera (Andor Technology, iXon DV-860, South Windsor, CT) at the rate of 485 Hz (2.06 ms/frame). The camera chip consisted of 128 x 128 pixels, each 24 μm x 24 μm. The effective pixel size after 150x magnification is 0.16 μm x 0.16 μm. The fluorescent protein mEos2 was activated using a 405 nm laser (CrystalLaser, Reno, Nevada, CW laser); the photoconverted state was subsequently excited with a 561 nm laser (Coherent Inc., Sapphire CW laser, Bloomingfield, CT). Both lasers illuminated the sample for the entire duration of image acquisition. Emission was collected through a 617/73 bandpass filter (bright line 617/73-25; Semrock, Rochester, NY) or a 610/75 bandpass filter (Chroma technology Corp, Bellows Falls, VT). The 405 nm power density at the sample was ~5-10 W/cm^2, which kept the average number of activated molecules in each camera frame to ~1. The 561 nm laser power density at the sample was ~8 kW/cm^2.

3.5.4 Single-molecule image analysis. The fluorescent images were analyzed using a MATLAB GUI developed in our lab. Two different digital filters were used to attenuate the noise in the images, namely, Gaussian and boxcar. Fluorescent signals were then identified using a peak finding algorithm with a user defined single-pixel intensity threshold. A particle is identified if the local intensity maximum is higher than the threshold. The threshold is carefully chosen large enough so that the algorithm can distinguish between the background and the signal and small enough to avoid cutting trajectories unduly short.

A centroid algorithm was used to locate the identified particles with sub-pixel resolution. Rapidly moving molecules have images that are blurred asymmetrically due to diffusion during the camera frame. Centroid fitting can locate these particles with better accuracy than Gaussian fitting. The centroid algorithm is also faster computationally. A 7 x 7 pixel box was drawn around the intensity maxima and the centroid of all the pixel intensities within the box was calculated. The centroid positions from successive frames were connected to form a trajectory only if they lie within 3 pixel = 480 nm of each other. A modified MATLAB version of the tracking program written by Crocker and Grier was used [57].

3.5.5 Mean-square displacement plots MSD(τ). The mean-square displacement (MSD) as a function of lag time τ provides a measure of the mean diffusion coefficient averaged over all molecules. It is defined by $MSD(\tau) = < (\boldsymbol{r}(t+\tau) - \boldsymbol{r}(t))^2 >$, where $\boldsymbol{r}(t)$ is the two-dimensional location of the particle at time t, τ is the lag time, and the average is taken over all times t and over many trajectories. The slope of the first two points of an MSD(τ) plot provides an estimate of the mean diffusion coefficient: D_{Mean} = slope/4. The MSD equation factors in the localization error σ , which can be measured from the y-intercept of the plot, [58] but it does not account for confinement effects. Even for 6-step long (12 ms) trajectories, for rapidly diffusing species with D ~ 5 μm^2-s^{-1}, confinement restricts diffusive trajectories and causes downward curvature of the MSD plot. Hence the estimated mean diffusion coefficient yields a lower bound of the true D_{Mean}. The trajectory analysis presented below takes into account both the localization error and confinement effects.

3.5.6 Monte Carlo simulations of diffusive trajectories. As explained in our previous work [19, 34], we fit our experimental $P_{EF\text{-}Tu}(r)$ single-step displacement distribution with two-state simulated distributions that account for the confinement effects. There is no analytical solution

that includes confinement effects; the best estimates of the true diffusion coefficients is obtained by simulation. We have assumed that the two diffusive states have different localization errors, σ_{slow} and $\sigma_{fast.}$ The estimation of σ_{slow} and σ_{fast} is explained in detail in our previous paper [19]. We simulated large number of random walk trajectories, each moving with a particular diffusion coefficient D with localization error σ_{slow} or σ_{fast}. The simulations are carried out in a confining spherocylinder, which mimics the mean length of an *E. coli* cell growing in each particular growth medium. The cell diameter was kept at 0.8 μm, consistent with the observation from phase contrast imaging that cell diameter varies little under different growth conditions. Each set of simulated trajectories represents one diffusive state with fixed D and σ. We simulated 5000 6-step long trajectories for each set, with 1000 microsteps during the 2 ms time between camera frames. These trajectories are used to compute model-based, numerical one-step probability distributions $P_{model}(r;D)$ for the numerical least-squares analysis of the corresponding experimental distributions. The simulation procedure is explained in more detail in our previous paper [19].

3.5.7 Fitting of single-step *P*(*r*) distributions to static, two-state models. For every growth condition, experimental trajectories which lasted 6 steps or longer were selected for analysis. The trajectories were truncated at the 6th step. The 6-steps trajectories were then sliced into individual steps. The displacement in every step was calculated as $r_i = \sqrt{(x_{i+1} - x_i)^2 + (y_{i+1} - y_i)^2}$ and were pooled to form the distribution $P(r)$ as in Fig 3.2B. We typically attempt to fit the experimental distribution $P(r)$ in a least-squares sense to a weighted average of two static populations. For unconstrained models including two static (non-exchanging) states, the fitting function is the linear combination $P_{model}(r) = f_{slow}P(r;D_{slow}) + (1 - f_{slow})P(r;D_{fast})$. Here the three fitting parameters are D_{fast}, D_{slow}, and the fractional population f_{slow}, which in turn fixes

f_{fast} = (1 – f_{slow}). For all our fitting procedures, D_{fast} ranged from 0.1 to 9 μm^2/s with interval of 0.1 μm^2/s and D_{slow} ranged from 0.05 to 3 μm^2/s with interval of 0.05 μm^2/s. The goodness of each fit was evaluated by calculating the reduced chi-square statistic (χ_v^2). We generated a 3-D matrix of χ_v^2 values, with each axis representing one of the three fitting parameters. The parameters which gave the minimum χ_v^2 were chosen as the best fit. The $P(r)$ fitting and the error estimation in the fitting parameters are explained in further detail in our previous paper [19]. The fitting results for each of the growth conditions are listed in Table 3.1.

3.5.8 Average number of copies of EF-Tu bound to one translating, 70S ribosome. Two-state modeling of the single-step displacement distribution $P_{EF\text{-}Tu}(r)$ yields the best fit parameters D_{fast}, D_{slow}, and f_{slow} plus their uncertainties. In all cases, D_{slow} is much larger than the diffusion coefficient of translating, 70S ribosomes, D_{70S} = 0.3 ± 0.1 μm^2/s. Therefore we assert that D_{slow} is a weighted average of the 70S diffusion coefficient and of D_{fast} :

$$D_{slow} = \alpha D_{70S} + (1 - \alpha) D_{fast}, \tag{2}$$

where α is the fraction of the apparent slow population that is bound to 70S ribosomes. We can solve for α in terms of measured quantities:

$$\alpha = (D_{fast} - D_{slow}) / \left(D_{fast} - D_{Rb}\right) \tag{3}$$

The mean number of EF-Tu copies bound per 70S ribosome is then:

$$N_{EF-Tu/70S} = \alpha f_{slow} Q / \beta \, , \tag{4}$$

where f_{slow} is the apparent fraction of slow EF-Tu copies, Q is the ratio of total EF-Tu copies to total ribosome copies, and β is the fraction of ribosomes engaged in translation. For all growth conditions studied here, Q lies in the range 6–7 and β (for glucose) = 0.85 ± 0.05 and β (for acetate) = 0.70 ± 0.05. The values for the 0.1 M NaCl media for both glucose and acetate are obtained from ref [14]. The values for higher salt media are kept same as the lower salt ones in

accord with ref [16]. Table 3.2 includes the values of α, *Q*, and β used for each of the four growth conditions studied, along with their estimated uncertainties. The resulting values of $N_{EF\text{-}Tu/70S}$ are included in Table 3.2 in the main text. The uncertainties are derived by propagating uncertainties in each of the factors in Eq. 4.

For three-state fitting (Table A3.3), the analogous equations are:

$$N_{EF-Tu/70S} = (\alpha f_{medium} + f_{slow})Q/\beta \quad (5)$$

$$\alpha = (D_{fast} - D_{medium})/(D_{fast} - D_{slow}) \quad (6)$$

The resulting values are included in Table A3.2.

3.6 Figures and Tables

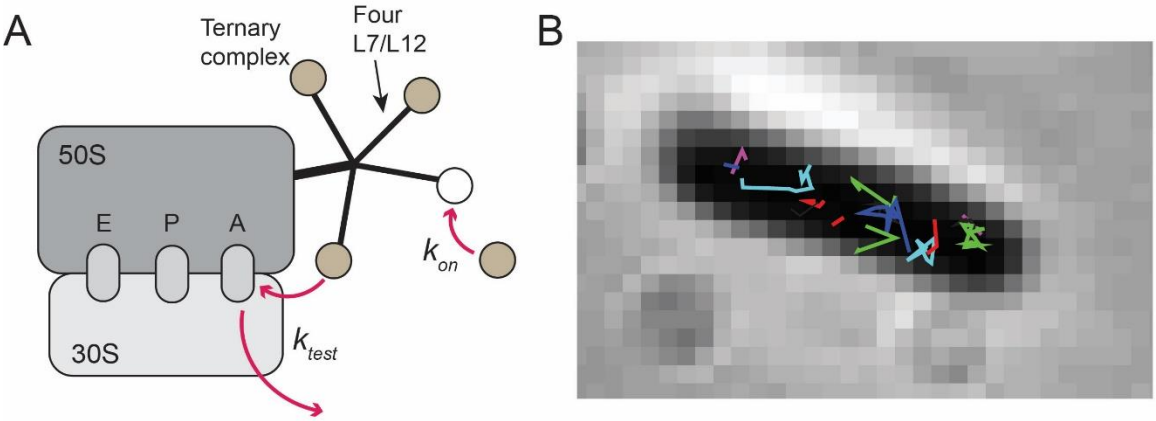

Fig. 3.1: A) Schematic diagram of ternary complexes (TCs) binding to the four L7/L12 ribosomal sites prior to codon testing at the A-site. Because most of the TCs are not cognate, these experiments pertain to the preponderance of events in which a TC binds and is tested and rejected. This must be very rapid to enable delivery of (the unusual) cognate TCs at ~20 aa/s or even faster. **B)** EF-Tu/ternary complex trajectories overlaid on the phase contrast image of a cell grown in MBM-glucose with 0.1 M NaCl at 37°C.

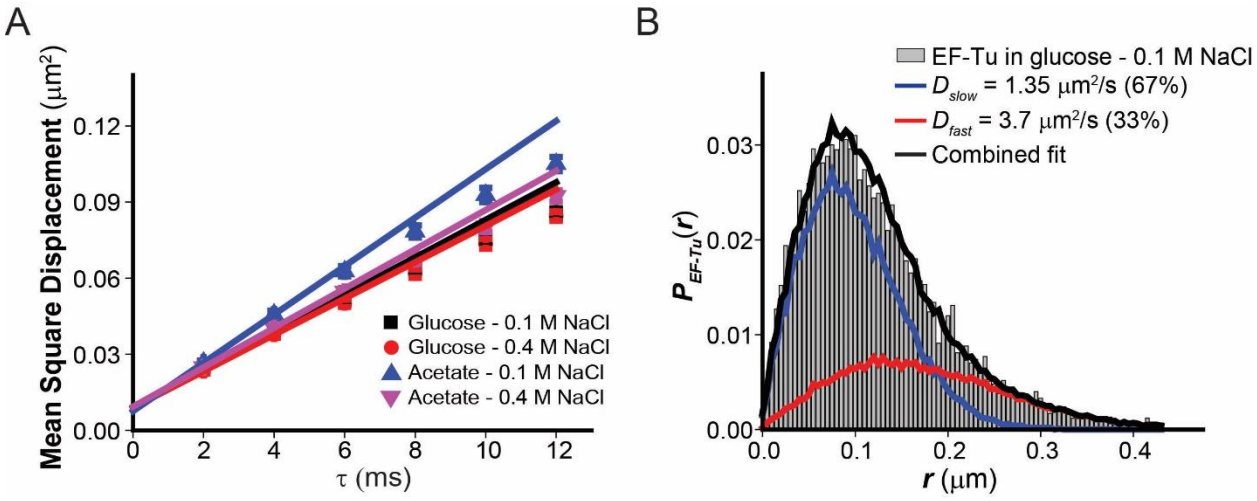

Fig. 3.2: A) MSD vs τ plot of EF-Tu/ternary complex in different growth media at 37°C as indicated. The mean diffusion coefficient D_{mean} as estimated from the slope of the first two points is quite similar in all the different growth conditions studied (Table 3.1). **B)** Histogram of the normalized single-step length distribution of EF-Tu/ternary complex in MBM-glucose with 0.1 M NaCl at 37°C. Best-fit two-state model results are shown. See Table 3.1, Methods, and Appendix for details.

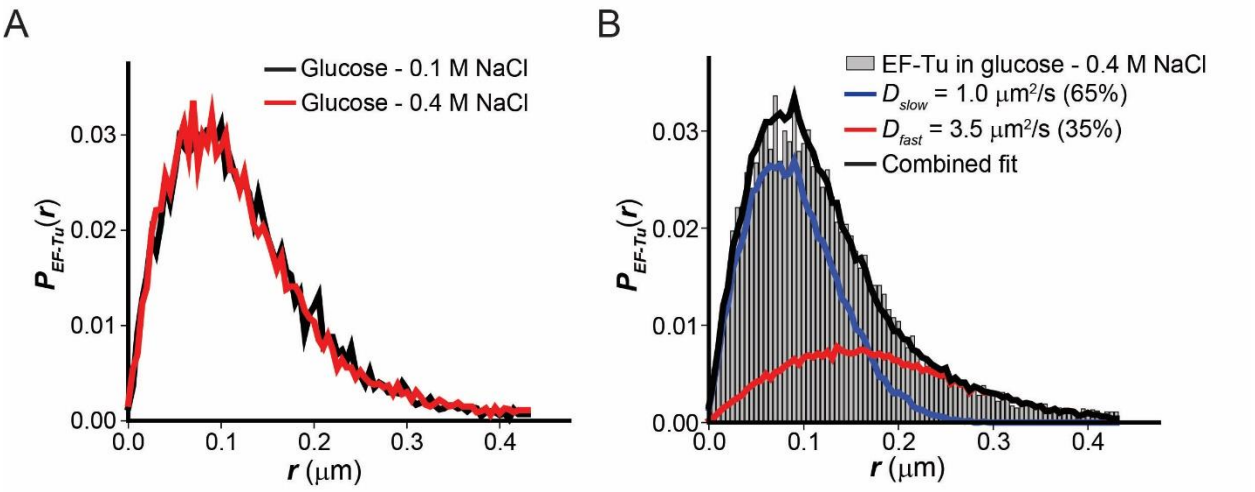

Fig. 3.3: A) Comparison of experimental single-step length distributions of EF-Tu in MBM-glucose plus 0.1 M NaCl and 0.4 M NaCl. The two distributions overlap closely. **B)** Best-fit two-state model of $P_{EF\text{-}Tu}(r)$ in MBM-glucose plus 0.4 M NaCl.

Table 3.1. Results of two-state fitting of EF-Tu diffusion for four different growth conditions.

Growth medium [a]	Osmolality (Osm)	Doubling time (min)	D_{Mean} [b] (μm²/s)	D_{fast} [c] (μm²/s)	D_{slow} [c] (μm²/s)	f_{slow}[c]	χ_v^2 [c]
Glucose - 0.1 M NaCl	0.28	62 ± 2	1.84 ± 0.19	3.7 ± 1.1	1.35 ± 0.30	0.67 ± 0.05	1.07
Glucose - 0.4 M NaCl	0.81	104 ± 4	1.79 ± 0.16	3.5 ± 1.0	1.0 ± 0.1	0.65 ± 0.05	1.28
Acetate - 0.1 M NaCl	0.3	101 ± 2	2.38 ± 0.21	4.3 ± 0.9	1.5 ± 0.3	0.55 ± 0.05	0.95
Acetate - 0.4 M NaCl	0.81	190 ± 9	1.94 ± 0.16	4.1 ± 0.6	1.65 ± 0.20	0.65 ± 0.05	1.15
EZRDM 30°C	0.28	60 ± 3	2.02 ± 0.19	4.9 ± 1.2	1.0 ± 0.2	0.60 ± 0.05	1.24

[a] All at 37°C, except for EZRDM at 30°C (Mustafi and Weisshaar, 2018).

[b] From initial slope of MSD plots (Fig. 3.2A).

[c] Best-fit parameters from two-state fitting of $P_{EF\text{-}Tu}(r)$ histograms (Fig. 3.2B, 3.3B and A3.4B,C and Methods). Fractional population of the fast state is $f_{fast} = (1 - f_{slow})$. χ_v^2 is the reduced chi-square statistic for the best fit.

Table 3.2. Number of EF-Tu bound per 70S ribosome for different growth conditions.

Growth medium	α [a,b]	f_{slow} [a,b]	Q [a,c]	β [a,d]	$N_{EF\text{-}Tu/70S}$ [a]
Glucose – 0.1 M NaCl	0.69 ± 0.13	0.67 ± 0.05	6.5 ± 0.5	0.85 ± 0.05	3.5 ± 0.8
Glucose – 0.4 M NaCl	0.78 ± 0.08	0.65 ± 0.05	6.5 ± 0.5	0.85 ± 0.05	3.9 ± 0.6
Acetate – 0.1 M NaCl	0.70 ± 0.10	0.55 ± 0.05	6.5 ± 0.5	0.70 ± 0.05	3.6 ± 0.7
Acetate – 0.4 M NaCl	0.64 ± 0.08	0.65 ± 0.05	6.5 ± 0.5	0.70 ± 0.05	3.9 ± 0.7

[a] Parameters from Eq. 4.

[b] Values obtained from two-state fitting as shown in Table 3.1.

[c] The copy number ratio of EF-Tu to ribosome stays nearly constant across growth conditions (Dai *et. al.*, 2016, Dai *et. al.*, 2018).

[d] Values for glucose and acetate at 0.1 M NaCl are obtained from Fig 3c of Dai *et. al.*, 2016. The values for higher salt are kept same as the lower salt according to Fig 1d of Dai *et. al.*, 2018.

3.7 References

[1] H. Bremer, P. Dennis, Modulation of chemical composition and other parameters of the cell at different exponential growth rates, EcoSal Plus. doi:10.1128/ecosal.5.2.3 (2008).

[2] D.G. Dalbow, R. Young, Synthesis time of beta-galactosidase in *Escherichia coli* B/r as a function of growth rate, Biochem J. 150 (1975) 13-20.

[3] R. Young, H. Bremer, Polypeptide-chain-elongation rate in *Escherichia coli* B/r as a function of growth rate, Biochem J. 160 (1976) 185.

[4] S.H. Li, Z. Li, J.O. Park, C.G. King, J.D. Rabinowitz, N.S. Wingreen, et al., *Escherichia coli* translation strategies differ across carbon, nitrogen and phosphorus limitation conditions, Nat Microbiol. 3 (2018) 939-947.

[5] F.C. Neidhardt, B. Magasanik, Studies on the role of ribonucleic acid in the growth of bacteria, Biochim Biophys Acta. 42 (1960) 99-116.

[6] R.M. Voorhees, V. Ramakrishnan, Structural basis of the translational elongation cycle, Annu Rev Biochem. 82 (2013) 203-236.

[7] I. Wohlgemuth, C. Pohl, J. Mittelstaet, A.L. Konevega, M.V. Rodnina, Evolutionary optimization of speed and accuracy of decoding on the ribosome, Philos Trans R Soc Lond B Biol Sci. 366 (2011) 2979-2986.

[8] T. Pape, W. Wintermeyer, M.V. Rodnina, Complete kinetic mechanism of elongation factor Tu-dependent binding of aminoacyl-tRNA to the A site of the *E. coli* ribosome, EMBO J. 17 (1998) 7490-7497.

[9] S.C. Blanchard, R.L. Gonzalez, H.D. Kim, S. Chu, J.D. Puglisi, tRNA selection and kinetic proofreading in translation, Nat Struct Mol Biol. 11 (2004) 1008-1014.

[10] P. Geggier, R. Dave, M.B. Feldman, D.S. Terry, R.B. Altman, J.B. Munro, et al., Conformational sampling of aminoacyl-tRNA during selection on the bacterial ribosome, J Mol Biol. 399 (2010) 576-595.

[11] S. Rudorf, M. Thommen, M.V. Rodnina, R. Lipowsky, Deducing the kinetics of protein synthesis in vivo from the transition rates measured in vitro, PLoS Comput Biol. 10 (2014) e1003909.

[12] S. Rudorf, R. Lipowsky, Protein synthesis in *E. coli*: Dependence of codon-specific elongation on tRNA concentration and codon usage, PLoS One. 10 (2015) e0134994.

[13] G. Zhang, I. Fedyunin, O. Miekley, A. Valleriani, A. Moura, Z. Ignatova, Global and local depletion of ternary complex limits translational elongation, Nucleic Acids Res. 38 (2010) 4778-4787.

[14] X. Dai, M. Zhu, M. Warren, R. Balakrishnan, V. Patsalo, H. Okano, et al., Reduction of translating ribosomes enables *Escherichia coli* to maintain elongation rates during slow growth, Nat Microbiol. 2 (2016) 16231.

[15] S. Klumpp, M. Scott, S. Pedersen, T. Hwa, Molecular crowding limits translation and cell growth, Proc Natl Acad Sci U S A. 110 (2013) 16754-16759.

[16] X. Dai, M. Zhu, M. Warren, R. Balakrishnan, H. Okano, J.R. Williamson, et al., Slowdown of translational elongation in *Escherichia coli* under hyperosmotic stress, mBio. 9 (2018) e02375-02317.

[17] F.C. Neidhardt, P.L. Bloch, S. Pedersen, S. Reeh, Chemical measurement of steady-state levels of ten aminoacyl-transfer ribonucleic acid synthetases in *Escherichia coli*, J Bacteriol. 129 (1977) 378-387.

[18] A. Schmidt, K. Kochanowski, S. Vedelaar, E. Ahrne, B. Volkmer, L. Callipo, et al., The quantitative and condition-dependent *Escherichia coli* proteome, Nat Biotechnol. 34 (2016) 104-110.

[19] M. Mustafi, J.C. Weisshaar, Simultaneous binding of multiple EF-Tu copies to translating ribosomes in live *Escherichia coli*, mBio. 9 (2018) e02143-02117.

[20] M. Diaconu, U. Kothe, F. Schlunzen, N. Fischer, J.M. Harms, A.G. Tonevitsky, et al., Structural basis for the function of the ribosomal L7/12 stalk in factor binding and GTPase activation, Cell. 121 (2005) 991-1004.

[21] U. Kothe, H.J. Wieden, D. Mohr, M.V. Rodnina, Interaction of helix D of elongation factor Tu with helices 4 and 5 of protein L7/12 on the ribosome, J Mol Biol. 336 (2004) 1011-1021.

[22] R.R. Traut, D. Dey, D.E. Bochkariov, A.V. Oleinikov, G.G. Jokhadze, B. Hamman, et al., Location and domain structure of *Escherichia coli* ribosomal protein L7/L12: site specific cysteine crosslinking and attachment of fluorescent probes, Biochem Cell Biol. 73 (1995) 949-958.

[23] M. Helgstrand, C.S. Mandava, F.A. Mulder, A. Liljas, S. Sanyal, M. Akke, The ribosomal stalk binds to translation factors IF2, EF-Tu, EF-G and RF3 via a conserved region of the L12 C-terminal domain, J Mol Biol. 365 (2007) 468-479.

[24] A. Liljas, S. Sanyal, The enigmatic ribosomal stalk, Q Rev Biophys. 51 (2018) e12.

[25] E. Betzig, G.H. Patterson, R. Sougrat, O.W. Lindwasser, S. Olenych, J.S. Bonifacino, et al., Imaging intracellular fluorescent proteins at nanometer resolution, Science. 313 (2006) 1642-1645.

[26] S. Manley, J.M. Gillette, G.H. Patterson, H. Shroff, H.F. Hess, E. Betzig, et al., High-density mapping of single-molecule trajectories with photoactivated localization microscopy, Nat Methods. 5 (2008) 155-157.

[27] A.V. Furano, The elongation factor Tu coded by the *tufA* gene of *Escherichia coli* K-12 is almost identical to that coded by the *tufB* gene, J Biol Chem. 252 (1977) 2154-2157.

[28] O. Wiborg, C. Andersen, C.R. Knudsen, B.F.C. Clark, J. Nyborg, Mapping *Escherichia coli* elongation factor Tu residues involved in binding of aminoacyl-tRNA, J Biol Chem. 271 (1996) 20406-20411.

[29] B.P. English, V. Hauryliuk, A. Sanamrad, S. Tankov, N.H. Dekker, J. Elf, Single-molecule investigations of the stringent response machinery in living bacterial cells, Proc Natl Acad Sci U S A. 108 (2011) E365-E373.

[30] A. Nenninger, G. Mastroianni, C.W. Mullineaux, Size dependence of protein diffusion in the cytoplasm of *Escherichia coli*, J Bacteriol. 192 (2010) 4535-4540.

[31] S. Bakshi, B.P. Bratton, J.C. Weisshaar, Subdiffraction-limit study of Kaede diffusion and spatial distribution in live *Escherichia coli*, Biophys J. 101 (2011) 2535-2544.

[32] N. Ban, B. Freeborn, P. Nissen, P. Penczek, R.A. Grassucci, R. Sweet, et al., A 9 A resolution X-ray crystallographic map of the large ribosomal subunit, Cell. 93 (1998) 1105-1115.

[33] W.M. Clemons, J.L.C. May, B.T. Wimberly, J.P. McCutcheon, M.S. Capel, V. Ramakrishnan, Structure of a bacterial 30S ribosomal subunit at 5.5 Å resolution, Nature. 400 (1999) 833-840.

[34] S. Mohapatra, H. Choi, X. Ge, S. Sanyal, J.C. Weisshaar, Spatial distribution and ribosome-binding dynamics of EF-P in live *Escherichia coli*, mBio. 8 (2017) e00300-00317.

[35] A. Sanamrad, F. Persson, E.G. Lundius, D. Fange, A.H. Gynnå, J. Elf, Single-particle tracking reveals that free ribosomal subunits are not excluded from the *Escherichia coli* nucleoid, Proc Natl Acad Sci U S A. 111 (2014) 11413-11418.

[36] S. Bakshi, A. Siryaporn, M. Goulian, J.C. Weisshaar, Superresolution imaging of ribosomes and RNA polymerase in live *Escherichia coli* cells, Mol Microbiol. 85 (2012) 21-38.

[37] Q. Chai, B. Singh, K. Peisker, N. Metzendorf, X. Ge, S. Dasgupta, et al., Organization of ribosomes and nucleoids in *Escherichia coli* cells during growth and in quiescence, J Biol Chem. 289 (2014) 11342-11352.

[38] H. Dong, L. Nilsson, C.G. Kurland, Co-variation of tRNA abundance and codon usage in *Escherichia coli* at different growth rates, J Mol Biol. 260 (1996) 649-663.

[39] P.P. Dennis, H. Bremer, Differential rate of ribosomal protein synthesis in *Escherichia coli* B/r, J Mol Biol. 84 (1974) 407-422.

[40] M.C. Konopka, K.A. Sochacki, B.P. Bratton, I.A. Shkel, M.T. Record, J.C. Weisshaar, Cytoplasmic protein mobility in osmotically stressed *Escherichia coli*, J Bacteriol. 191 (2009) 231-237.

[41] J. Shine, L. Dalgarno, The 3'-terminal sequence of *Escherichia coli* 16S ribosomal RNA: complementarity to nonsense triplets and ribosome binding sites, Proc Natl Acad Sci U S A. 71 (1974) 1342-1346.

[42] B.S. Laursen, H.P. Sørensen, K.K. Mortensen, H.U. Sperling-Petersen, Initiation of protein synthesis in bacteria, Microbiol Mol Biol Rev. 69 (2005) 101.

[43] M. Ehrenberg, V. Dincbas, D. Freistroffer, V. Heurgué-Hamard, R. Karimi, M. Pavlov, et al., Mechanism of bacterial translation termination and ribosome recycling, In: R. Garret, S.R. Douthwaite, A. Liljas, A.T. Matheson, P.B. Moore, H.F. Noller, (eds). The Ribosome: Structure, Function, Antibiotics and Cellular Interactions. Washington, DC: American Society of Microbiology; 2000. p. 541-551.

[44] U. Kanjee, K. Ogata, W.A. Houry, Direct binding targets of the stringent response alarmone (p)ppGpp, Mol Microbiol. 85 (2012) 1029-1043.

[45] R.B. Harshman, H. Yamazaki, MS I accumulation induced by sodium chloride, Biochemistry. 11 (1972) 615-618.

[46] K. Braeken, M. Moris, R. Daniels, J. Vanderleyden, J. Michiels, New horizons for (p)ppGpp in bacterial and plant physiology, Trends Microbiol. 14 (2006) 45-54.

[47] K. Shimizu, Regulation systems of bacteria such as *Escherichia coli* in response to nutrient limitation and environmental stresses, Metabolites. 4 (2013) 1-35.

[48] P. Milon, E. Tischenko, J. Tomsic, E. Caserta, G. Folkers, A. La Teana, et al., The nucleotide-binding site of bacterial translation initiation factor 2 (IF2) as a metabolic sensor, Proc Natl Acad Sci U S A. 103 (2006) 13962-13967.

[49] A.M. Rojas, M. Ehrenberg, S.G. Andersson, C.G. Kurland, ppGpp inhibition of elongation factors Tu, G and Ts during polypeptide synthesis, Mol Gen Genet. 197 (1984) 36-45.

[50] B. Wang, P. Dai, D. Ding, A. Del Rosario, R.A. Grant, B.L. Pentelute, et al., Affinity-based capture and identification of protein effectors of the growth regulator ppGpp, Nat Chem Biol.10.1038/s41589-018-0183-4 (2018).

[51] M. Kjeldgaard, P. Nissen, S. Thirup, J. Nyborg, The crystal structure of elongation factor EF-Tu from *Thermus aquaticus* in the GTP conformation, Structure. 1 (1993) 35-50.

[52] L.C. Thomason, J.A. Sawitzke, X. Li, N. Costantino, D.L. Court, Recombineering: genetic engineering in bacteria using homologous recombination, Curr Protoc Mol Biol. 106 (2014) 1.16.11-39.

[53] J.C. Crocker, D.G. Grier, Methods of digital video microscopy for colloidal studies, J Colloid Interface Sci. 179 (1996) 298-310.

[54] X. Michalet, Mean square displacement analysis of single-particle trajectories with localization error: Brownian motion in an isotropic medium, Phys Rev E Stat Nonlin Soft Matter Phys. 82 (2010) 041914.

3.8 Appendix

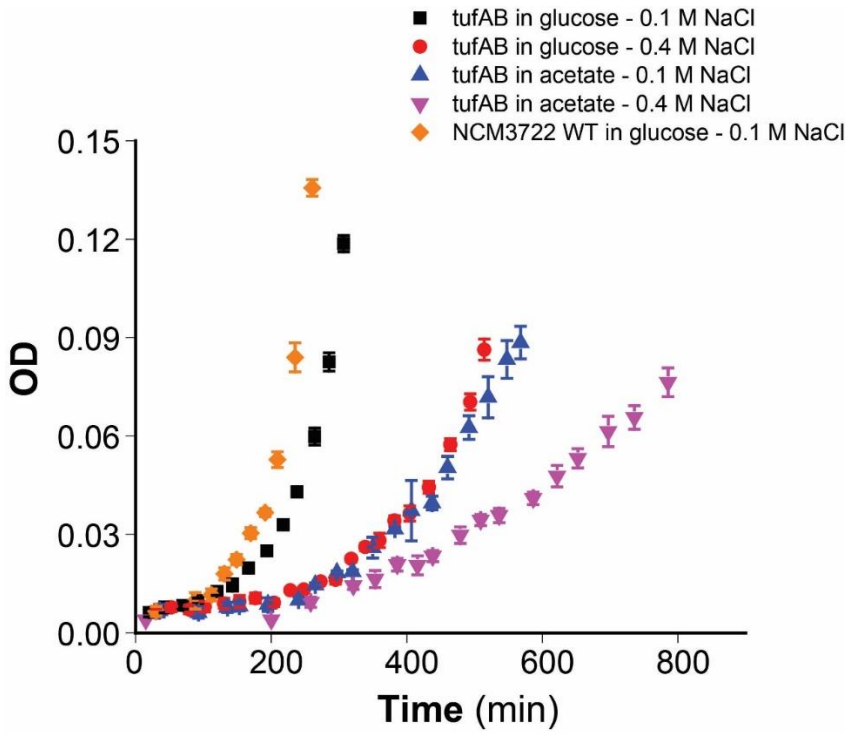

Fig. A3.1: Growth curves of the labeled EF-Tu (*tufAB*) strain in the NCM3722 background in different growth media as indicated. The temperature is 37°C in all cases. The data for WT (NCM3722) cells grown in MBM-glucose - 0.1 M NaCl are shown for comparison with the mutant strains. Growth slows down on changing the carbon source from glucose to acetate and also with increasing salt concentration from 0.1 M to 0.4 M NaCl.

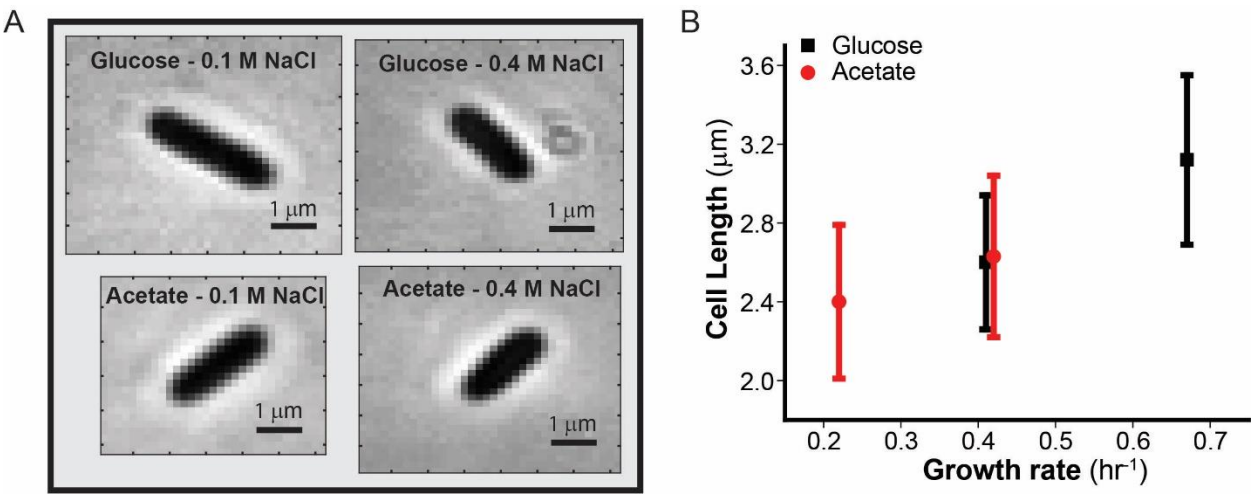

Fig. A3.2: A) Example of typical phase contrast images of cells growing different MBM media as shown. The cell length changes with nutrient limitation as well as with higher osmolality. **B)** Plot of mean cell length vs exponential growth rate λ (hr^{-1}). The exponential growth rate is related to the doubling time t_2 as: $\lambda = \ln 2/t_2$. Data from 40 cells for each condition. The mean cell length increases roughly linearly with growth rate. Vertical bars show ± 1 standard deviation.

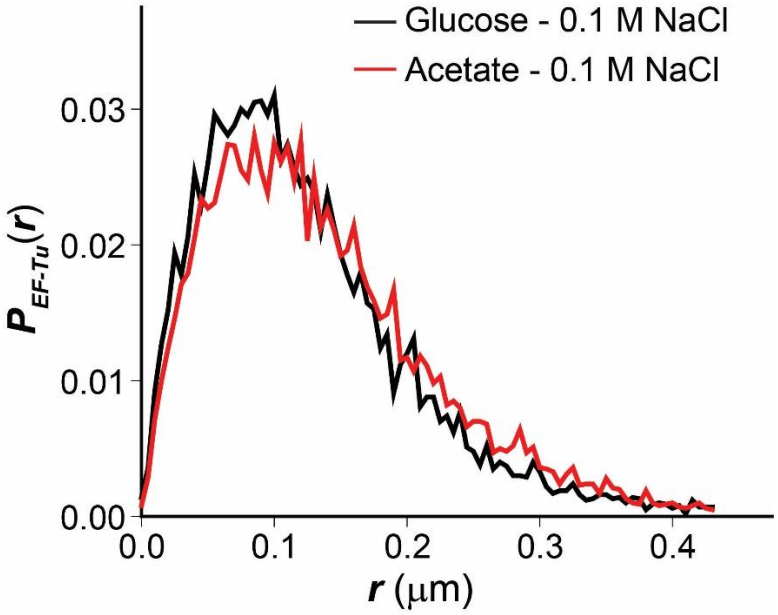

Fig. A3.3: Comparison of experimental single step length distributions of EF-Tu in glucose with 0.1 M NaCl vs acetate with 0.1 M NaCl.

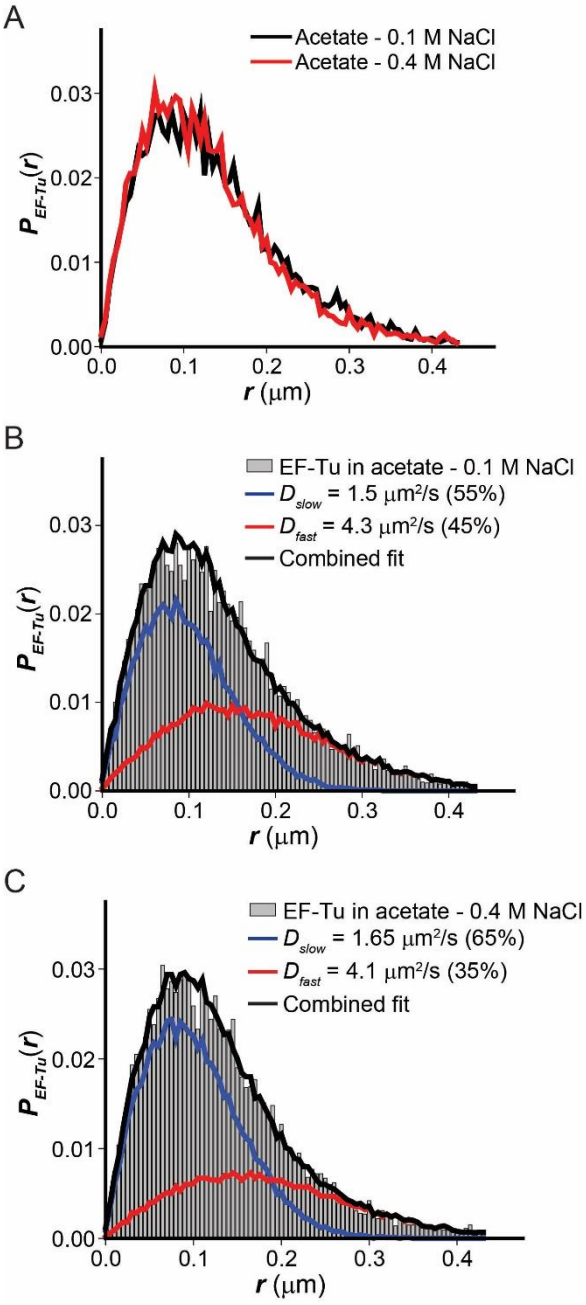

Fig. A3.4: A) Comparison of experimental single step length distributions of EF-Tu in MBM-acetate with 0.1 M NaCl and with 0.4 M NaCl. **B)** Two-state fitting of $P_{EF\text{-}Tu}(r)$ in MBM-acetate with 0.1 M NaCl. **C)** Two-state fitting of $P_{EF\text{-}Tu}(r)$ in MBM-acetate with 0.4 M NaCl.

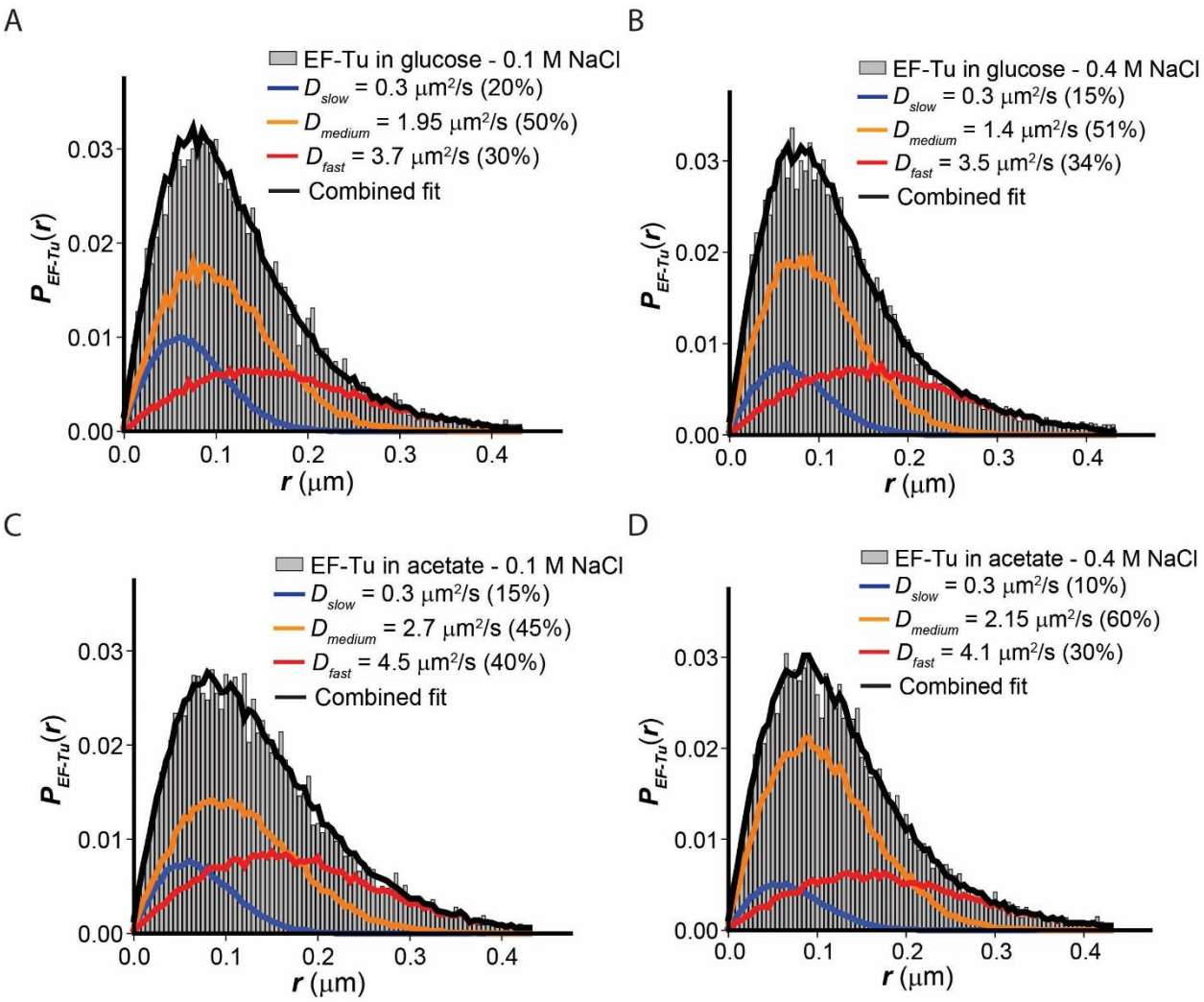

Fig. A3.5: A) Best three-state fits to experimental single step length distributions of EF-Tu in glucose with 0.1 M NaCl. D_{slow} is fixed at 0.3 μm^2/s. **B)** Best three-state fit to $P_{EF\text{-}Tu}(r)$ in glucose with 0.4 M NaCl. **C)** Best three-state fit to $P_{EF\text{-}Tu}(r)$ in acetate with 0.1 M NaCl. **D)** Best three-state fit of $P_{EF\text{-}Tu}(r)$ in acetate with 0.4 M NaCl. See Table A3.2 for summary of best-fit parameters and χ_υ^2.

Table A3.1: Doubling times and the corresponding growth rates of the different strains in different growth conditions.

Growth Medium [a]	Doubling time (min)	Growth rate λ (hr^{-1})
NCM3722 WT in glucose – 0.1 M NaCl	48 ± 1	0.87 ± 0.02
tufAB in glucose - 0.1 M NaCl	62 ± 2	0.67 ± 0.02
tufAB in glucose - 0.4 M NaCl	104 ± 4	0.40 ± 0.02
tufAB in acetate - 0.1 M NaCl	101 ± 2	0.42 ± 0.01
tufAB in acetate - 0.4 M NaCl	190 ± 9	0.22 ± 0.01

[a] All at 37 ˚C.

Table A3.2: Three-state fit parameters of EF-Tu single-step displacement distribution in different growth conditions.

Growth Medium (all at 37°C)	D_{slow} [a] (μm²/s)	D_{medium} [b] (μm²/s)	D_{fast} [b] (μm²/s)	f_{slow} [b]	f_{medium} [b]	χ_v^2 [b]	$N_{EF\text{-}Tu/70S}$ [c]
Glucose - 0.1 M NaCl	0.3	1.95 ± 0.4	3.7 ± 1.2	0.20 ± 0.05	0.50 ± 0.05	1.02	3.5 ± 0.9
Glucose - 0.4 M NaCl	0.3	1.4 ± 0.2	3.5 ± 1.1	0.15 ± 0.05	0.51 ± 0.05	1.24	3.7 ± 0.8
Acetate - 0.1 M NaCl	0.3	2.7 ± 0.6	4.5 ± 1.4	0.15 ± 0.05	0.45 ± 0.05	0.79	3.2 ± 1.1
Acetate - 0.4 M NaCl	0.3	2.15 ± 0.3	4.1 ± 1.2	0.10 ± 0.05	0.60 ± 0.05	1.05	3.8 ± 1.2

[a] D_{slow} was fixed at 0.3 μm²/s in all cases.

[b] Best-fit parameters from three-state fitting of $P_{EF\text{-}Tu}(r)$ histogram.

[c] Calculated using the three-state model of Eq. 5. The middle fraction was considered to be a composite of ribosome-bound and free EF-Tu.

Table A3.3: One-state fits of EF-Tu single step displacement distributions in different growth conditions.

Growth Medium [a]	D (μm²/s)	χ_v^2
Glucose - 0.1 M NaCl	1.4 ± 0.3	4.78
Glucose - 0.4 M NaCl	0.7 ± 0.1	8.87
Acetate - 0.1 M NaCl	2.3 ± 0.2	4.09
Acetate - 0.4 M NaCl	1.3 ± 0.3	5.74

[a] All at 37 ˚C.

Chapter 4:

Long-term Effects of the Proline-rich Antimicrobial Peptide Oncocin112 on the *E. coli* cytoplasm

Reproduced from:

Mustafi M, Zhu Y, Weisshaar JC, Long-term Effects of the Proline-rich Antimicrobial Peptide Oncocin112 on the *E. coli* cytoplasm, 2019, manuscript in preparation.

4.1 ABSTRACT

Proline-rich antimicrobial peptides (PrAMPs) are cationic AMPs unusual for their ability to penetrate bacterial membranes and kill cells without causing membrane permeabilization. Structural studies show that many such PrAMPs bind deep in the peptide exit channel of the ribosome, near the peptidyl transfer center (PTC). Biochemical studies of the particular synthetic PrAMP oncocin112 (Onc112) suggest that on reaching the cytoplasm, the peptide occupies its binding site prior to the transition from initiation to the elongation phase of translation, thus blocking further initiation events. We present a superresolution fluorescence microscopy study of the long-term effects of Onc112 on ribosome, EF-Tu, and DNA spatial distributions and diffusive properties in intact *E. coli* cells. The new data help to corroborate earlier mechanistic inferences from studies *in vitro*. Comparisons with the diffusive behavior induced by the ribosome-binding antibiotics chloramphenicol (Cam) and kasugamycin (Ksg) show how the specific location of each agent's ribosomal binding site affects the long-term distribution of ribosomal species between 30S and 50S subunits vs 70S-polysomes. Analysis of the single-step displacements from ribosome and EF-Tu diffusive trajectories before and after Onc112 treatment suggests that the act of codon testing of non-cognate ternary complexes (TCs) at the ribosomal A-site enhances the dissociation rate of such TCs from their L7/L12 tethers. Such enhancement enables codon testing of the TCs to occur at a rate sufficiently rapid to keep up with the very fast elongation rate of ribosomes for cells in fast exponential growth.

4.2 INTRODUCTION

Most antibiotics currently in use against bacterial infections disable a specific essential cellular mechanism, such as translation (*e.g.*, erythromycin), transcription (rifampicin), membrane biosynthesis (ampicillin), or DNA replication (norfloxacin). As a result, development of resistance by localized mutations in the targeted species is often facile. As harmful bacteria become increasingly resistant to antibiotics, there is a critical need to develop new antibacterial agents. A promising class of compounds is the large family of antimicrobial peptides (AMPs), part of the innate immune response of a wide variety of organisms including humans. Many of these short (~20 aa long), typically cationic peptides are potent bacteriocidal agents that leave eukaryotic cells largely unharmed [1]. The first step in the attack of most cationic AMPs is the permeabilization of the membrane(s) of Gram-negative or Gram-positive species. In general, on gaining access to the bacterial cytoplasm, AMPs subsequently disrupt a variety of cellular processes.

Intriguingly, the subclass known as proline-rich AMPs (PrAMPs) evidently attack and kill Gram-negative bacteria such as *E. coli* without permeabilizing the membranes [2]. These cationic peptides are enriched in proline residues, which often occur in conserved patterns that also include arginine residues [3]. Examples include apidaecin from bees, oncocin from milkweed bugs, and bactenecin 5 and 7 from ruminant animals [3-5]. At low concentrations near the minimum inhibitory concentration (MIC), the PrAMPs primarily use a “Trojan horse” mechanism to enter the bacterial cell via the SbmA transporter or one of its homologs [3, 6]. SbmA resides in the cytoplasmic membrane of some Gram-negative species and imports the highly cationic PrAMPs into the cytoplasm using the proton motive force. Once they have entered the cytoplasm, the PrAMPs target 70S ribosomes. No homolog of the SbmA transporter

occurs in eukaryotic cells, explaining the low cytotoxicity of the PrAMPs. This makes PrAMPs an attractive class of antibacterial agents for further refinement [5].

One such natural PrAMP is oncocin. Specific amino acid residues of oncocin have recently been modified to increase its potency, giving rise to the synthetic oncocin112 (Onc112; sequence VDKPPYLPRPRPPRrIYNr-NH2, in which r denotes d-arginine; net charge +6) [7, 8]. In 2015, two labs published X-ray crystallography structures of Onc112 bound to the 70S ribosome in complex with a short mRNA and with a deacylated $tRNA^{fMet}$ or $tRNA^{Met}$ bound at the P-site [9, 10]. The structures showed that Onc112 binds deep within the peptide exit channel and extends into the peptidyl transferase center (PTC), where it overlaps what would be the binding site of an incoming aa-tRNA at the ribosomal A-site (Fig. 4.1A). From this structure and from biochemical experiments, it was inferred that Onc112 blocks the transition of the 70S ribosome from the initiation complex into the peptide elongation phase of protein synthesis. The suggestion is that Onc112 enters the ribosome through an empty peptide exit channel, *i.e.*, Onc112 must bind before elongation has begun to fill the exit channel and to block the Onc112 binding site. Therefore, ribosomes bearing Onc112 stall at the initiation site and cannot transition to peptide elongation. In addition, experiments using a short, di-cistronic mRNA suggested that binding of Onc112 also destabilizes the initiation complex itself, presumably due to spatial overlap between Onc112 and the fMet moiety of the fMet-$tRNA^{fMet}$ bound in the P-site [10]. Ribosomes can still assemble as 70S initiation complexes on the mRNA, but with decreased stability.

This is somewhat reminiscent of the behavior of certain ribosome-targeting antibiotics such as chloramphenicol (Cam), kasugamycin (Ksg), and many others. Cam binds the 70S ribosome at the A-site crevice near the exit channel, hindering the binding of an incoming aa-

tRNA to the A-site (Fig. 4.1A) [11]. Unlike Onc112, Cam can bind to elongating ribosomes, not just to initiation complexes [12]. Thus Cam potentially blocks elongation by all 70S ribosomes. In another example, Ksg binds to the mRNA exit channel within the 30S subunit, overlapping both the E-site and P-site (Fig. 4.1A) [13]. Ksg prevents binding of fMet-tRNA^{fMet} and also blocks the E-site to prevent elongation. Thus Ksg halts the initiation step and prevents the onset of elongation [13].

We have used fluorescence microscopy to study in real time the sequence of events during the attack of AMPs on single, live *E. coli* cells [14, 15]. Different assays can dissect the onset of outer membrane permeabilization, cytoplasmic membrane permeabilization [16], the halting of growth, induction of oxidative stress [17], and alterations in the spatial distributions and diffusive properties of a variety of cytoplasmic components [18]. In this study, we quantitatively characterize the long-term effects of Onc112 on the spatial distributions ribosomes, EF-Tu, and the chromosomal DNA in intact *E. coli* cells. We also compare the effects of Onc112, Cam, and Ksg on the diffusive behavior of the same cytoplasmic components. The results help to corroborate earlier mechanistic inferences from *in vitro* studies and provide new biophysical insight into their effects on the overall condition of the *E. coli* cytoplasm.

Onc112 and Ksg, both of which block transitions to the elongation phase of translation, have very similar effects on ribosome diffusion, increasing the average diffusion coefficient by a factor of 2. Cam, which can halt translation by 70S ribosomes during the elongation phase, has a minor effect on the average ribosome diffusion coefficient. All three treatments decrease the average EF-Tu diffusion coefficient by a factor of 1.3–1.6. These results correlate well with information from the earlier structural studies of the Onc112, Ksg, and Cam specific binding sites within the ribosome. Analysis of the single-step displacement distributions from ribosome

and EF-Tu diffusive trajectories suggests that the act of codon testing of non-cognate ternary complexes (TCs) at the ribosomal A-site hastens the dissociation of such TCs from their L7/L12 tethers. This enables sufficiently rapid codon testing to keep up with the very fast elongation rate of ribosomes in good growth conditions.

4.3 RESULTS

4.3.1 Effects of Onc112 on cell growth

The minimum inhibitory concentration (MIC) of Onc112 over 6 hr in EZ rich, defined medium (EZRDM) at 30°C is 1 μM (Fig. A4.1). We plated wild-type (WT) VH1000 cells on a poly-L-lysine coated coverslip enclosed by a microfluidic chamber. Such cells grow normally in a flow of fresh, aerated EZRDM. At $t = 0$, we initiate flow of a constant concentration of Onc112 in EZRDM through the microfluidic chamber and monitor cell length vs time as determined from phase contrast images by the program Fiji [19]. In Fig. 4.2A, we plot $L(t)/L_0$, the cell length as a function of time normalized to the length at $t = 0$, averaged over 10-23 cells for different concentrations of Onc112. For all concentrations, the plots begin to curve downward at $t \sim 5$ min after the onset of Onc112 flow. The higher the concentration of Onc112, the sooner cell length begins to plateau. For 5 μM and higher concentrations, the effect on cell growth is similar.

To test for evidence of outer membrane disruption by Onc112 in our conditions, we applied fixed concentrations of the PrAMP to cells expressing GFP with a tag directing transport to the periplasm (strain JCW10). In our standard assay for cell growth and for outer and inner membrane permeabilization to GFP and Sytox orange [16], phase contrast and green and red fluorescence images are captured alternately in time, with a cycle time of 12 s. We saw no

evidence of membrane permeabilization to GFP and Sytox orange, at least up to Onc112 concentrations of 10 μM (10X MIC) over a period of 60 min. The phase contrast images remain stable at least up to Onc112 concentrations of 20 μM over a period of 45 min, indicating little or no loss of cytoplasmic components. There is no evidence of membrane disruption in our conditions, consistent with earlier work.

4.3.2 Spatial distribution of ribosomes, EF-Tu and DNA after Onc112 treatment

For these experiments, cells were grown to exponential phase (OD ~ 0.2-0.4) in EZRDM in culture tubes at 30ºC. At that point we added Onc112 to 20 μM (20x MIC) and incubated the culture for an additional 30-40 min before plating the cells for fluorescence microscopy. Such a high concentration was used to ensure that essentially all of the cells were affected by Onc112 prior to observation by fluorescence microscopy. The modified VH1000 strains of *E. coli* and their labeling schemes are described in Table A4.1. As before [20-23], to locate and track single copies of ribosomal species (MSG196 strain, S2-mEos2 labeling) and of EF-Tu (tufAB strain, mEos2 labeling) we use superresolution fluorescence microscopy (Methods). The gene modifications are made on the chromosome, so that all copies of the protein of interest carry the label. The doubling times of WT, MSG196, and tufAB strains in EZRDM at 30°C are 45 ± 2 min, 49 ± 2 min, and 60 ± 3 min, respectively. Labeling of the S2 protein has only a minor effect on cell growth, whereas labeling of the protein EF-Tu causes a moderate growth defect of ~33%. Fig. 4.2B compares the length distribution of cells growing normally in EZRDM with that of cells treated with 20 μM Onc112 for 30-40 min. The distribution of the treated cells is shifted towards smaller lengths, consistent with slowing and then halting of growth.

In order to detect rapidly diffusing species on the same footing as slowly diffusing species, we imaged single molecules at 2 ms/frame. In each camera frame we maintained a low density of photoactivated mEos2, with 0, 1, or 2 copies per cell. The resulting single-molecule trajectories are short, averaging only about 3 camera frames. For untreated cells in exponential growth, the S2 protein is essentially always incorporated into a complete 30S ribosomal subunit. However, the 30S subunits we track may occur as freely diffusing 30S copies searching for translation initiation sites or as 30S subunits incorporated into translating 70S ribosomes, typically part of a 70S-polysome chain [20, 22]. In earlier work on cells in exponential growth, we analyzed EF-Tu trajectories as arising from a combination of slowly diffusing, ribosome-bound copies and rapidly diffusing copies attributed to free EF-Tu or EF-Tu bound within ternary complexes [21].

Examples of ribosome and EF-Tu trajectories using the same labeling schemes have been shown previously [21]. In Fig. 4.3 we compare the cell-averaged ribosome and EF-Tu spatial distributions in untreated, exponentially growing cells (length range 4-5 μm) with those in cells treated with 20 μM Onc112 for 30-40 min (length range 3-4 μm). In each case the chosen range lies near the peak of the length distribution (Fig. 4.2B). As observed before, in normal exponential growth with 45-min doubling time, most cells exhibit three axially distinct ribosome-rich regions (Fig. 4.3A) [20, 22]. The chromosomal DNA has segregated into two lobes which sit in the valleys between the ribosome peaks. A histogram of the projected axial positions scaled to each cell length shows the three ribosome peaks more quantitatively (Fig. 4.3E). The EF-Tu distribution may also have three axial peaks (Fig. 4.3C), but the dips between the peaks are not nearly as pronounced as those for ribosomes. This is consistent with part of the EF-Tu population being ribosome-bound at a given moment. The spatial distributions after

Onc112 treatment are markedly different. Now the ribosomes concentrate in the two endcaps (Fig. 4.3B, F). The EF-Tu distribution again roughly mimics that of the ribosomes, but the dip between nominal EF-Tu peaks is even less pronounced (Fig. 4.3D, F).

Our next goal was to image ribosomes and the chromosomal DNA in single cells after Onc112 treatment to characterize the degree of DNA-ribosome segregation. For these widefield fluorescence microscopy experiments, we used strain MSG192 (Table A4.1) in which the ribosomal S2 protein is tagged with eYFP in the VH1000 background. This enables co-imaging of the 30S ribosomal subunit using its YFP tag and the chromosomal DNA using the DNA stain Sytox Orange. We studied 88 cells in this way; two representative single-cell images and their axially projected ribosome and DNA linescans are shown in Fig. 4.4. In all cells, the ribosome linescans again show two peaks at the endcaps. All the DNA linescans show a broad, centrally located peak, typically with a small dip at cell center. There is little or no DNA in the endcaps, where DNA-ribosome segregation is strong. The small dip in the DNA axial distribution suggests the presence of two DNA lobes that are not well separated from each other. More pronounced dips occur more often in longer cells. In all cases, the position of the central dip in the DNA linescan corresponds to that of a small, third peak in the ribosome linescan. In widefield images of untreated cells under the same growth conditions, we previously observed substantially more complete spatial segregation of the two DNA lobes (Bakshi *et. al.* [20], Fig. 1). It appears that ribosome-DNA segregation is less severe in the nucleoid region of Onc112-treated cells than in untreated cells.

4.3.3 Diffusion of ribosomes and EF-Tu after Onc112, Cam, and Ksg treatment

The antimicrobial peptide Onc112 and the bactericidal drugs chloramphenicol (Cam) and kasugamycin (Ksg) are all known to halt translation by binding to 70S ribosomes, but the binding modes differ. Next we compare the average diffusive motion of the ribosomal species and the EF-Tu species in untreated cells in exponential growth and in cells treated by Onc112, Cam, and Ksg. The drug treatments used 300 μg/mL (20x MIC) of Cam for ~35 min or 5 mg/mL (30x MIC) of Ksg for ~35 min, similar to the Onc112 treatment of 20x MIC concentration for ~35 min. To characterize the average diffusion coefficient of a species, we form trajectories that track the centroid of each single-molecule image across consecutive 2-ms camera frames. We analyze only trajectories that survive at least 7 camera frames (six steps) and truncate the longer trajectories at the seventh frame. A mean-square displacement vs lag time plot MSD(τ) is formed by measuring the square of the displacement over the lag times τ = 1 step, 2 steps, etc., and averaging over all molecules in all cells. For free Brownian diffusion in two dimensions, MSD(τ) = $4D_{mean}\tau$. We use the initial slope of the plot (first two data points) to provide an estimate of D_{mean} and the *y*-intercept to provide an estimate of the average localization error σ.

MSD(τ) plots for ribosomes over 12 ms are shown in Fig. 4.5A. The downward curvature is likely due to true sub-diffusion rather than confinement effects on the short timescale of the observations. For 2 ms/frame imaging of ribosomes in untreated, exponentially growing *E. coli*, we obtain D_{mean} = 0.40 ± 0.10 μm^2/s [21]. This is reasonably consistent with a smooth extension of the strongly curved MSD plots observed previously on substantially longer timescales [24]. Onc112 treatment and Ksg treatment increase D_{mean} to 0.74 ± 0.09 μm^2/s (by 1.9x) and to 0.79 ±

0.21 μm^2/s (by 2.0x), respectively. Cam treatment yields D_{mean} = 0.48 ± 0.11 μm^2/s, only 1.2 times the result in normal growth.

In an attempt to resolve the ribosomal diffusive motion into sub-populations, the same trajectories in untreated cells and in cells after Onc112 treatment were divided into individual steps of 2 ms duration, providing the distribution of apparent single-step displacements $P_{ribo}(r)$ (Fig. 4.6). In Fig. A4.2, we directly compare the two $P_{ribo}(r)$ curves; it is clear that ribosome diffusion is faster for Onc112-treated cells, consistent with the MSD(τ) plots. As before [21], we model each $P_{ribo}(r)$ distribution using a static two-state model which assumes that the displacements arise from a composite of a slowly diffusing population and a rapidly diffusing population that do not exchange on the 2-ms imaging timescale. The numerical model includes confinement effects and localization uncertainty (Methods and [21]). The fitting parameters are the diffusion coefficient of the slow population D_{slow}, the diffusion coefficient of the fast population D_{fast}, and the fraction of slow copies f_{slow}; by subtraction, $f_{fast} = 1 - f_{slow}$.

For ribosomes in untreated cells the best-fit values are D_{slow} = 0.10 ± 0.10 μm^2/s, f_{slow} = 0.70 ± 0.05, D_{fast} = 1.2 ± 0.5 μm^2/s, and f_{fast} = 0.30 ± 0.05, with χ_v^2 = 0.67 [21]. For Onc112 treated cells, the best-fit values are D_{slow} = 0.25 ± 0.1 μm^2/s, f_{slow} = 0.46 ± 0.05, D_{fast} = 1.3 ± 0.2 μm^2/s, and f_{fast} = 0.54 ± 0.05, with χ_v^2 = 1.1. These results are collected in Table 4.1. $P_{ribo}(r)$ for Onc112-treated cells differs from that of untreated cells primarily due to a shift in fractional population from the slow state to the fast state. The underlying diffusion coefficients remain sensibly constant.

The same MSD and one-step distribution analyses were applied to EF-Tu trajectories obtained at 2 ms/frame from untreated cells and from cells treated with Onc112, Cam, and Ksg.

The MSD(τ) plots in Fig. 4.5B show that on average, EF-Tu diffuses faster in untreated cells than in cells treated with Onc112, Cam, or Ksg. The latter three plots are quite similar in slope. There is again downward curvature. The numerical results from the first two points are: D_{mean} = 2.02 ± 0.19 μm^2/s for the untreated cells [21], 1.25 ± 0.22 μm^2/s after Onc112 treatment (1.6x smaller than in untreated cells), 1.39 ± 0.32 μm^2/s after Cam treatment (1.5x smaller), and 1.52 ± 0.26 μm^2/s after Ksg treatment (1.3x smaller).

The single-step distributions $P_{EF\text{-}Tu}(r)$ for untreated cells and for cells treated with Onc112 and with Cam are compared in Fig. 4.7. These curves were fit to the same static two-state model used for ribosomes. For EF-Tu in untreated cells, the best-fit results are: D_{slow} = 1.00 ± 0.20 μm^2/s, f_{slow} = 0.60 ± 0.05, D_{fast} = 4.9 ± 1.2 μm^2/s, and f_{fast} = 0.40 ± 0.05, with χ_v^2 = 1.2 (Table 4.1) [21]. Consistent with the MSD plots, the two-state fits after Onc112 treatment and after Cam treatment are very similar. For EF-Tu in Onc112-treated cells, the best-fit results are: D_{slow} = 0.50 ± 0.10 μm^2/s, f_{slow} = 0.72 ± 0.05, D_{fast} = 5.0 ± 1.4 μm^2/s, and f_{fast} = 0.28 ± 0.05, with χ_v^2 = 1.4 (Table 4.1). In comparison with untreated cells, Onc112 has decreased D_{slow} by a factor of 2.0 and mildly increased f_{slow} as well. The two-state results for Cam-treated cells are quite similar to the results for Onc112-treated cells (Table 4.1). We obtain D_{slow} = 0.60 ± 0.2 μm^2/s, f_{slow} = 0.72 ± 0.05, D_{fast} = 3.9 ± 1.3 μm^2/s, and f_{fast} = 0.28 ± 0.05, with χ_v^2 = 1.4. Finally, $P_{EF\text{-}Tu}(r)$ after Ksg treatment closely mimics the curves after Onc112 and Cam treatment (Fig. A4.3). This is consistent with the MSD plots. These diffusion results are interpreted in the Discussion.

4.3.4 Sub-diffusion of the DNA locus *Right 2* after Onc112 and Cam treatment

To compare the local dynamics of the chromosomal DNA in untreated cells and in Onc112- and Cam-treated cells, we used the strain JCW154 (Table A4.1). In this strain the DNA

locus *Right 2* is labeled by the fusion protein ParB-GFP, which oligomerizes on a tandem array of *ParS* sites adjacent to the *Right 2* locus. At an imaging rate of 1 frame/s, we can monitor the locus position with accuracy of $\sigma \sim 30$ nm over 600 frames = 10 min without significant photobleaching. In Fig. 4.8 we compare mean-square displacement plots MSD(τ) for untreated cells, for Onc112- and Cam-treated cells, for cells treated with CCCP + 2-deoxy-glucose (which depletes ATP by dissipation of the proton motive force and prevention of glycolysis), and for cells 15 min after treatment with the antimicrobial peptide LL-37. These MSD plots show negative curvature, the signature of sub-diffusive motion, as expected for the local dynamics of a small segment of a large, confined polymer. The degree of curvature varies across the different cases. To enable semi-quantitative comparisons on the 10-s timescale, for each MSD curve we compute an apparent diffusion coefficient D_{app} from the slope of the linear least-squares fit to the first ten experimental points (Fig. 4.8B).

The numerical results are: $D_{app} = (2.0 \pm 0.2) \times 10^{-4}$ $\mu m^2/s$ for normal growth in the exponential phase; $(4.6 \pm 0.2) \times 10^{-5}$ $\mu m^2/s$ after CCCP treatment; $(6.6 \pm 2.4) \times 10^{-6}$ $\mu m^2/s$ after LL-37 treatment; $(6.6 \pm 0.6) \times 10^{-5}$ $\mu m^2/s$ after Cam treatment; and $(8.8 \pm 0.6) \times 10^{-5}$ $\mu m^2/s$ after Onc112 treatment. All the treatments attenuate the jiggling motion of the *Right 2* locus. The human AMP LL-37 has the strongest effect, decreasing D_{app} by a factor of 30 (almost no detectable motion) compared with untreated cells. Treatment with CCCP + deoxy-glucose, which destroys the transmembrane potential, decreases D_{app} by a factor of 4. The effects of Onc112 and of Cam are comparable, decreasing D_{app} by a factor of 2.3 and 3.0, respectively. We previously suggested that LL-37 forms strong non-covalent, polycation/polyanion, “pseudo-crosslinks” that bind the cationic peptide across nearby DNA strands, greatly rigidifying the nucleoid. Onc112 and Cam have a much more modest effect.

4.4 DISCUSSION

We have presented a substantial body of quantitative information comparing the long-term (~35 min) effects of the PrAMP Onc112 and the antibiotics Cam and Ksg on the diffusive behavior of several important cytoplasmic components. Onc112 shortens the average cell length (Fig. 4.2B), redistributes the DNA and ribosomal spatial distributions (Fig. 4.3), maintain strong DNA-ribosome segregation (Fig. 4.4), increases the average diffusion coefficient of ribosomal species (Fig. 4.5A), and decreases the average diffusion coefficient of EF-Tu (Fig. 4.5B). The effects of Ksg are quantitatively similar to those of Onc112 (Fig. 4.5). Cam treatment has a small effect on ribosome average diffusion, but slows EF-Tu average diffusion quite similarly to Onc112 and Ksg (Fig. 4.5). Here we use structural information for the Onc112, Cam, and Ksg binding sites on the ribosome to make sense of the observed diffusive behavior in intact cells.

As depicted in Fig. 4.1A, Onc112 and Ksg bind within the peptide exit channel and in the mRNA exit tunnel, respectively. Both species evidently must find their binding sites prior to the onset of the elongation phase of translation. Once bound, they prevent further elongation events while allowing already elongating 70S ribosomes to continue making protein. For mono-cistronic genes, such 70S ribosomes will produce complete protein copies on a timescale of ~30 s, fall off the mRNA, and be recycled as 30S + 50S subunits. For poly-cistronic genes, which are fairly commonplace in *E. coli*, on completion of an initial protein product the 70S ribosome will either fall off the mRNA or search diffusively trying to find the next downstream Shine-Dalgarno sequence, a process termed “70S-scanning initiation”. If there is no drug molecule blocking the initiation of the elongation cycle, 70S may then go on to produce the next protein prescribed by the mRNA sequence. In any event, after 20-30 min of Onc112 or Ksg treatment, we would anticipate a net conversion of part of the normal population of “dense 70S-polysomes”

to free 30S and 50S subunits and to "sparse 70S-polysomes", as depicted for Onc112 in Fig. 4.1B. The subunits will diffuse faster than the dense polysomes; the sparse polysomes may also diffuse faster than dense polysomes. Accordingly, we observe that the average diffusion coefficient of ribosomal species increases substantially after treatment with Onc112 or Ksg (Fig. 4.5A). In addition, the two-state decomposition of $P_{ribo}(r)$ indicates that the primary effect of Onc112 (Fig. 4.6) is to increase the fractional population of the more rapidly diffusing ribosomal species (presumably 30S subunits), again in accord with the picture in Fig. 4.1B. We suggest that Onc112 and Ksg have very similar effects on ribosome diffusion because they alter the composition of ribosomal species in much the same way.

In contrast, Cam can bind deep within the A-site crevice of all elongating 70S ribosomes and halt translation by blocking accommodation of the next codon-matching aa-tRNA within the peptidyl transferase center [11]. As before [12], we suggest that many dense 70S-polysomes are retained long-term after Cam treatment, as depicted in Fig. 4.1C. As a result, D_{mean} for ribosomes is changed very little by Cam.

For EF-Tu, we showed that before or after Onc112 treatment, the spatial distribution mimics that of the ribosomal species to a degree, but the axial peaks and valleys are less well defined (Fig. 4.3). This is consistent with substantial binding of EF-Tu–containing species to those ribosomal species that segregate most strongly from DNA, presumably the remaining 70S-polysomes. After all three treatments (Onc112, Ksg, and Cam), the mean diffusion coefficient of EF-Tu–containing species decreases by a factor of 1.3–1.6. The two-state decompositions of $P_{EF\text{-}Tu}(r)$ in untreated cells and in cells treated with Onc112 and with Cam indicate quantitatively similar effects of Onc112 and Cam. Both drugs increase the fraction of the slowly diffusing population (from 0.60 for untreated cells to 0.72 for treated cells) while decreasing D_{slow} (from

1.0 μm^2/s to 0.5–0.6 μm^2/s). Importantly, for both treated and untreated cells, D_{slow} for EF-Tu is significantly larger than D_{slow} for ribosomes in the corresponding condition (0.10 μm^2/s for untreated, 0.25 μm^2/s after Onc112 treatment, Fig. 4.6).

Initial binding of ternary complexes to the 70S ribosome occurs on any of four L7/L12 binding sites flexibly tethered to the 50S subunit near the A-site (Fig. 4.1A) [25-27], where the aa-tRNA within each ternary complex is tested for a codon match. For a given mRNA codon poised at the 30S decoding site, the chance that a particular TC carries a cognate (completely matching) aa-tRNA anticodon is roughly 1 in 40. Although the vast majority of aa-tRNAs fail the codon matching test, in good growth conditions the average elongation rate can be as fast as ~20 aa/s (~50 ms per complete elongation cycle). This implies very rapid codon testing on a timescale of ~1 ms or even less. Therefore testing and dissociation of non-cognate TCs from their L7/L12 tethers must occur rapidly on the 2-ms timescale between our camera frames. Accordingly, in our earlier work on untreated cells we suggested that the best-fit value of D_{slow} for EF-Tu was in fact a weighted average over slower diffusion of TCs bound to 70S ribosomes and much faster, free diffusion of unbound TCs. In this interpretation, the smaller the value of D_{slow} for EF-Tu, the longer the time that each non-cognate TC spends bound to its L7/L12 tether prior to dissociation. Our earlier work indicated that the four L7/L12 tethers are essentially saturated with TC binders during fast growth. Presumably this helps provide a steady supply of nearby TCs that can present themselves for codon testing very quickly each time the A-site becomes available after rejection of a non-cognate TC.

Now we apply this same idea to EF-Tu diffusion after Onc112 or Cam treatment. Both treatments result in significantly smaller values of D_{slow} for EF-Tu compared with untreated cells. The data then suggest that non-cognate ternary complexes (the vast majority) bind to L7/L12 for

a substantially longer time period when codon testing at the A-site is blocked by the peptide or antibiotic. In other words, the interaction of a tethered, non-cognate ternary complex with the A-site during the codon-testing event somehow stimulates faster dissociation from L7/L12 than would occur for TC dissociation from an isolated L7/L12 binding site. This is a qualitative inference only. We could be more quantitative if we knew the ratio between EF-Tu and ribosome copy numbers and the fraction of ribosomes occurring as 70S after treatment with each antibacterial agent, as in [21, 23]. Rodnina, Lipowsky, and coworkers [28, 29] have developed a detailed kinetics scheme for the branched, multi-step processes involved in ternary complex binding, selection of cognate aa-tRNAs, and elongation of the growing peptide chain. Our inference that the codon matching test at the A-site hastens the departure of non-cognate TCs fits within their scheme quite readily. In normal growth conditions, direct dissociation of TCs from L7/L12 tethers that are not interacting with the A-site need not be considered.

4.5 MATERIALS AND METHODS

4.5.1 Bacterial strains

Most of the strains used in this work (Table A4.1) contain modifications to the VH1000 background strain. The tufAB strain contains a C-terminus fusion of a photoconvertible protein, mEos2, to the *tufA* and *tufB* genes, both of which express identical copies of EF-Tu. The MSG196 and MSG192 strains contain a C-terminus fusion of mEos2 and YFP, respectively, to the S2 ribosomal protein. The JCW154 strain is in MG1655 background. In this strain the *Right2* locus of the chromosome is fused with a tandem array of parS sites. This strain also contains a plasmid which expresses ParB protein fused with GFP. The construction details are given in our previous papers. The description of the cells used and their corresponding doubling times are given in Table A4.1.

4.5.2 Cell growth and preparation for imaging

The cells were grown in a water bath shaker (New Brunswick Innova 3000, from Eppendorf) maintained at 200 rpm and 30°C. Bulk cultures were harvested from frozen glycerol stock solution and were grown in EZ rich defined medium (EZRDM) overnight until they reached stationary phase. On the following day, the stationary phase culture was divided into subcultures with at least 100-fold dilution in fresh EZRDM and again grown to exponential phase (OD = 0.2-0.5). Cells were then plated on a poly-L-lysine coated coverslip equipped with a CoverWell perfusion chamber (Electron Microscopy Science, PA) of well volume 140 µL. Untreated cells grow normally under these conditions for at least 30 min. For the different drug treatments, when the bulk culture reached exponential phase the cells were treated with the appropriate concentration of the drug and kept in the shaker for 30-40 min more. The drug concentrations were as follows: 20 µM of Onc112 (20x MIC), 300 µg/mL of Cam (20x MIC) and 5 mg/mL of Ksg (30x MIC). The cells were then plated as before. In all cases, the cells were imaged within ~5 min of plating.

4.5.3 Superresolution and widefield imaging of live *E. coli* cells

Cells were imaged with an inverted microscope (model Eclipse-Ti, Nikon Instruments, Melville, NY) equipped with an oil immersion objective (CFI Plan Apo Lambda DM 100x Oil, 1.45 NA), a 1.5x tube lens, and the Perfect Focus System. The localization and single-particle trajectory analyses were performed as described earlier. For superresolution imaging, the individual fields of view were imaged no longer than 20 s to minimize laser damage. Each prepared sample was imaged for no longer than 30 min. During this period the untreated cells continued to grow normally. The fluorescence images were recorded on a back-plane illuminated electron-multiplying charge-coupled device (EMCCD) camera (Andor Technology, iXon DV-

860, South Windsor, CT) at the rate of 485 Hz (2.06 ms/frame). The camera chip comprises 128 x 128 pixels, each 24 μm x 24 μm in real space. The effective pixel size after 150x magnification is 0.16 μm x 0.16 μm.

For superresolution imaging of single molecules, the fluorescent protein mEos2 was activated using a 405 nm laser (CrystalLaser, Reno, Nevada, CW laser); the photoconverted state was subsequently excited with a 561 nm laser (Coherent Inc., Sapphire CW laser, Bloomingfield, CT). Both lasers illuminated the sample for the entire duration of image acquisition. Fluorescence was collected through a 610/75 bandpass filter (Chroma technology Corp, Bellows Falls, VT). The 405 nm power density at the sample was ~5-10 W/cm^2, which kept the average number of activated molecules in each camera frame to ~1. The 561 nm laser power density at the sample was ~8 kW/cm^2.

For widefield imaging of S2-YFP, Sytox-Orange-stained DNA, and tracking of DNA loci, the fluorescence images were obtained on a different EMCCD camera (Andor Technology, iXon DV-897, South Windsor, CT). The camera chip consisted of 512 x 512 pixels, each 16 μm x 16 μm. The effective pixel size after 150x magnification is 0.106 μm x 0.106 μm. For dual color experiments imaging S2-YFP (green channel) and Sytox Orange (red channel), μManager [30] was used to obtain the data and to switch filters between frames using a LB10-NW filter wheel (Sutter). The movies were obtained at 50-ms exposure time for each, with green fluorescence (488 nm excitation), red fluorescence (561 nm excitation), and phase contrast images. To minimize spectral bleed-through in the two-color experiments, we utilized the narrower filters HQ510/20 for the green channel and HQ600/50M for the red channel. Laser intensities at the sample were typically ~100 W/cm^2 at 488 nm and ~2.5 W/cm^2 at 561 nm. The frame rate was 20 Hz (50 ms/frame).

4.5.4 Cell length measurements

Tip-to-tip cell length was estimated from phase contrast images. For time lapse movies of the Onc112 treated cell lengths (Fig. 4.1A), we used FIJI (ImageJ) software to quantify the change in cell length over time. The distribution of cell lengths under different growth conditions (Fig. 4.1B) was obtained from the program Oufti using the parameters optimized for *E. coli* as provided with the software [31]. Results from FIJI and Outfi applied to the same image are similar.

4.5.5 Single-molecule image analysis

The fluorescence images were analyzed using a MATLAB GUI developed in our lab, as described previously [21, 23]. Noise was attenuated by two different digital filters. Fluorescent signals were then identified using a peak finding algorithm with a user-defined single-pixel intensity threshold. A particle is identified if the local intensity maximum is higher than the threshold. The threshold is carefully chosen so that the algorithm can distinguish between background and signal and avoid cutting trajectories unduly short.

Particles were located with sub-pixel resolution using a centroid algorithm. Rapidly moving molecules have images that are blurred asymmetrically due to diffusion during the camera frame. Centroid fitting can locate these particles with better accuracy than Gaussian fitting. The centroid algorithm is also faster computationally. A 7 x 7 pixel box was drawn around the intensity maximum and the centroid of all the pixel intensities within the box was calculated. The centroid positions from successive frames were connected to form a trajectory only if the successive locations lie within 3 pixel = 480 nm of each other. A modified MATLAB version of the tracking program written by Crocker and Grier was applied to form the trajectories [32].

4.5.6 Mean-square displacement plots MSD(τ). For free diffusion in an infinite space, the mean diffusion coefficient averaged over all molecules can be obtained from the mean-square displacement (MSD) as a function of lag time τ. Here $MSD(\tau) = < (\boldsymbol{r}(t+\tau) - \boldsymbol{r}(t))^2 >$, where $\boldsymbol{r}(t)$ is the two-dimensional location of the particle at time t, τ is the lag time, and the average is taken over all times t and over many trajectories. The slope of the first two points of an MSD(τ) plot provides an estimate of the mean diffusion coefficient: D_{Mean} = slope/4. The localization error σ can be estimated from the y-intercept of the plot [33]. For rapidly diffusing species such as free EF-Tu or free ternary complexes imaged at 2 ms/frame, even 6-step (12 ms) trajectories are significantly restricted by confinement. This contributes to downward curvature of the MSD plot. Hence the estimated mean diffusion coefficient yields a lower bound of the true D_{Mean}. To account for confinement, we use simulated numerical trajectories for our analysis of single step displacement distributions $P(r)$, as described next.

4.5.7 Monte Carlo simulations of diffusive trajectories

Even for a homogeneous sample in which all particles have the same diffusion coefficient, there is no analytical formula for $P(r)$ that includes confinement effects and localization error. Instead, we simulate numerical diffusive trajectories using Monte Carlo methods in a spherocylindrical volume. As described previously [21, 23], we fit the experimental single-step displacement distribution $P(r)$ with two-state (or three-state) simulated distributions in order to account for confinement effects and localization error. We have assumed that the two diffusive states have different localization errors, σ_{slow} and $\sigma_{fast.}$ The estimation of σ_{slow} and σ_{fast} is explained in detail in our previous papers. Then we simulate a large number of random walk trajectories, each moving inside the spherocylinder with a particular diffusion coefficient D and with localization error σ_{slow} or σ_{fast}. Each set of simulations are carried out in a confining

spherocylinder, which mimics the average dimension of an *E. coli* cell for a specific growth condition and with a fixed D and σ and camera exposure time of 2 ms. For each parameter set, we calculate 5000 6-step trajectories with molecules initially located randomly within the spherocylinder. The sub-trajectory of each molecule during each camera frame is computed for 1000 microsteps of 2 μs duration. The centroid of each resulting 2 ms sub-trajectory is computed; localization error is included by sampling a Gaussian of appropriate σ. Trajectories are formed by joining the resulting locations over time. The 5000 trajectories are then used to compute a numerical single-step probability distributions $P_{model}(r;D)$ for use in the least-squares analysis of the corresponding experimental distributions.

4.5.8 Fitting of single-step *P*(*r*) distributions to static, two-state models

For every condition studied, experimental trajectories which lasted at least 6 steps were selected for analysis; longer trajectories were truncated after the 6th step. Each experimental single-step displacement was calculated as $r_i = \sqrt{(x_{i+1} - x_i)^2 + (y_{i+1} - y_i)^2}$; these were pooled from all trajectories to form the experimental distribution $P(r)$. We fit the experimental distribution $P(r)$ to a weighted average of two static populations, in a least-squares sense. For two states, the fitting function is $P_{model}(r) = f_{slow}P(r;D_{slow}) + (1 - f_{slow})P(r;D_{fast})$. Here the three fitting parameters are D_{fast}, D_{slow}, and the fractional population f_{slow}, which in turn fixes $f_{fast} = (1 - f_{slow})$. For all our fitting procedures, D_{slow} was sampled from 0.05 to 3 μm^2/s with interval of 0.05 μm^2/s and D_{fast} was sampled from 0.1 to 9 μm^2/s with interval of 0.1 μm^2/s. The goodness of each fit was evaluated by calculating the reduced chi-square statistic (χ_v^2). We generated a 3D matrix of χ_v^2 values, with each axis representing one of the fitting parameters. The parameters which gave the minimum χ_v^2 were chosen as the best fit. The $P(r)$ fitting and the error estimation for the fitting parameters are explained in further detail in our previous papers [21, 23].

4.6 Tables and figures:

Table 4.1. Fitting parameters for the different experimental conditions.

Species imaged [a]	D_{mean} (μm²/s) [b]	f_{slow} [c]	D_{slow} (μm²/s) [c]	D_{fast} (μm²/s) [c]	χ_v^2 [c]
Ribosome (untreated) [21]	0.4 ± 0.1	0.70 ± 0.05	0.1 ± 0.1	1.2 ± 0.5	0.67
Ribosome (Onc112 treatment)	0.74 ± 0.09	0.46 ± 0.05	0.25 ± 0.10	1.3 ± 0.2	1.1
Ribosome (Cam treatment)	0.48 ± 0.11	-	-	-	-
Ribosome (Ksg treatment)	0.79 ± 0.21	-	-	-	-
EF-Tu (untreated) [21]	2.02 ± 0.10	0.60 ± 0.05	1.0 ± 0.1	4.9 ± 1.2	1.24
EF-Tu (Onc112 treatment)	1.25 ± 0.22	0.72 ± 0.05	0.5 ± 0.1	5.0 ± 0.14	1.43
EF-Tu (Cam treatment)	1.39 ± 0.32	0.72 ± 0.05	0.6 ± 0.2	3.9 ± 0.13	1.38
EF-Tu (Ksg treatment)	1.52 ± 0.26	-	-	-	-

[a] All are in VH1000 background, grown in EZRDM at 30 °C.

[b] From initial slope of MSD plots (Fig. 4.5).

[c] Best-fit parameters from two-state fitting of $P_{EF\text{-}Tu}(r)$ histograms (Fig. 4.6 and 4.7). Fractional population of the fast state is $f_{fast} = (1 - f_{slow})$. χ_v^2 is the reduced chi-square statistic for the best fit.

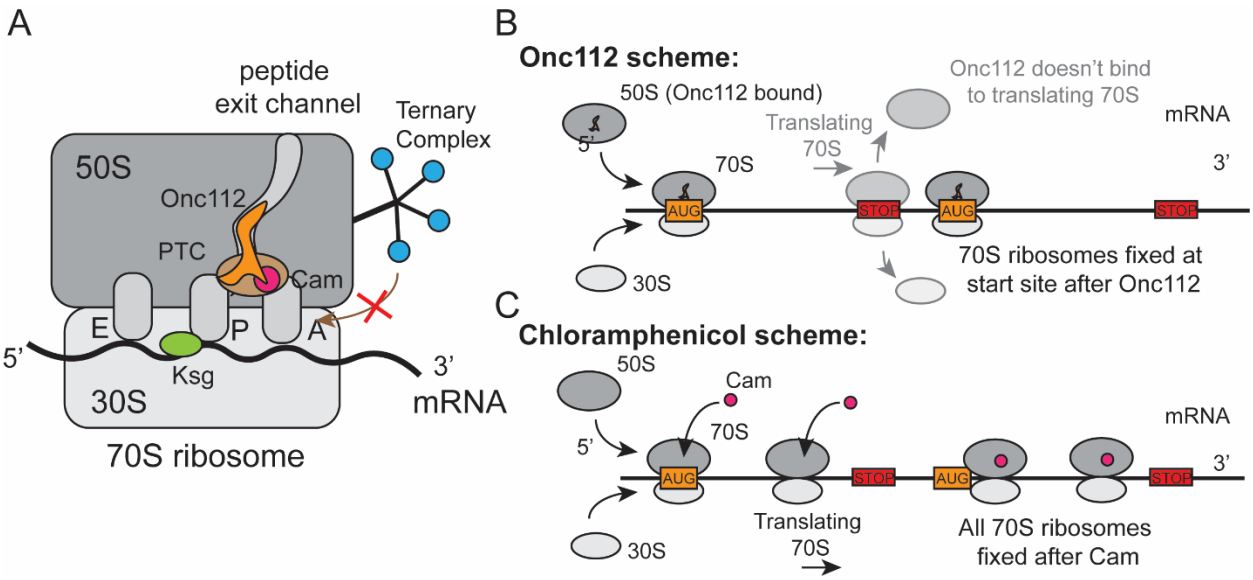

Figure 4.1. A) Schematic of the Onc112, Cam, and Ksg binding sites within a 70S ribosome. Onc112 binds to the peptide exit channel. Cam binds at the A-site cleft. Ksg binds at the mRNA tunnel. **B)** Onc112 prevents the transition from initiation to elongation. Most 70S ribosomes that are already elongating when Onc112 binds will complete their protein and dissociate to 30S and 50S. **C)** Cam halts translation of all 70S ribosomes, including those in the elongation phase.

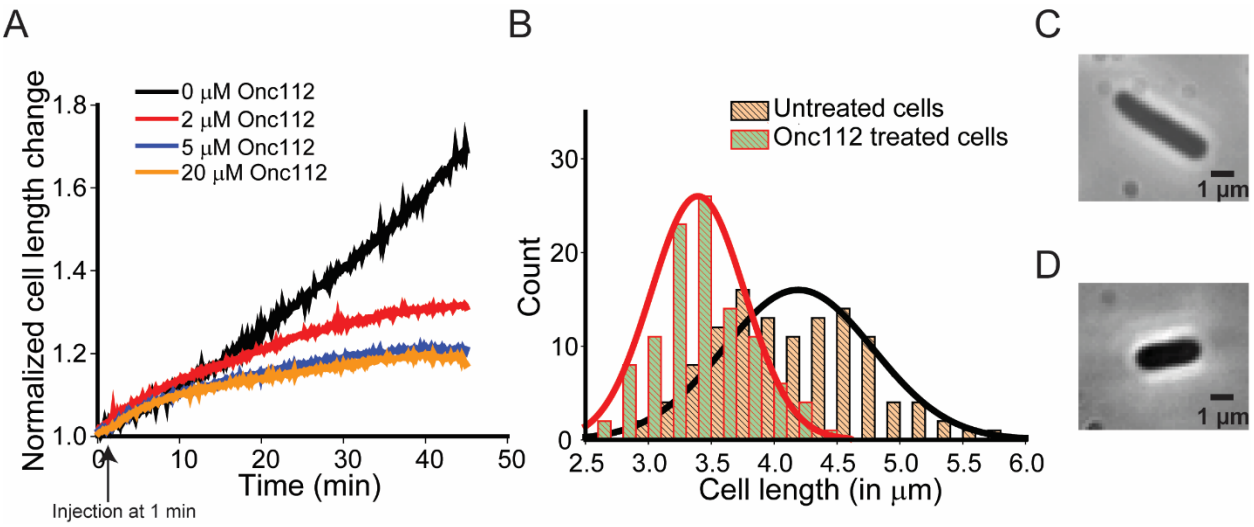

Figure 4.2. Average cell length change vs time for VH1000 WT cells after the onset of flow of different concentration of Onc112. Cell lengths obtained from phase contrast images are normalized to the length at time 0: $L(t)/L_0$. Onc112 was injected at 1 min. Effects of Onc112 become noticeable at $t \sim 5$ min after injection.

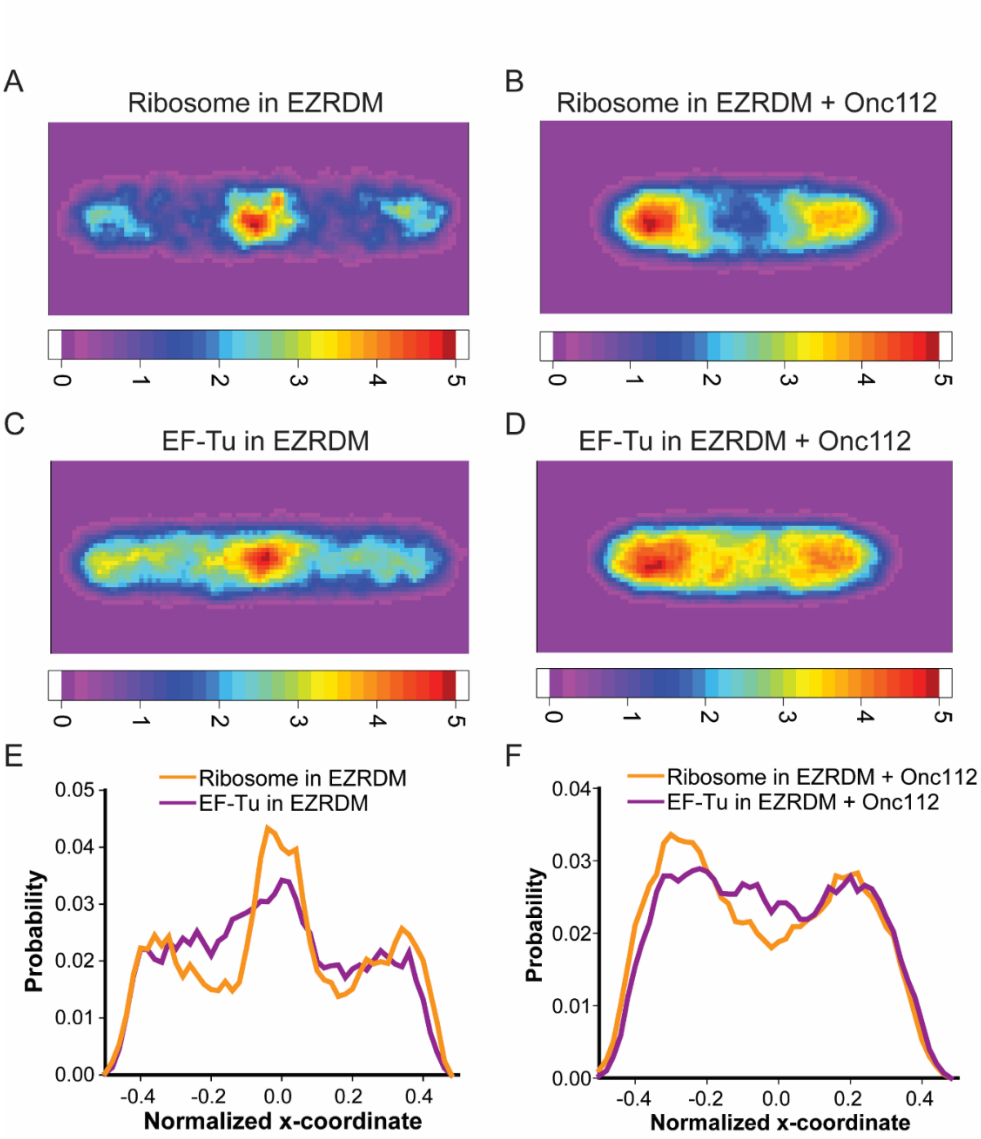

Figure 4.3. A) and B) Superresolution spatial distributions of ribosomes in normal growth conditions and 40 min after the onset of Onc112 treatment. 4-5 μm long untreated cells and 3-4 μm long Onc112 treated cells were used to obtain the spatial distributions. Positions obtained from ~100-200 cells are combined to form the composite distribution. **C) and D)** Analogous spatial distributions of EF-Tu in normal growth conditions and 40 min after the onset of Onc112 treatment. **E)** Axial projections of the distributions shown in A and C. **F)** Axial projections of the distributions shown in B and D.

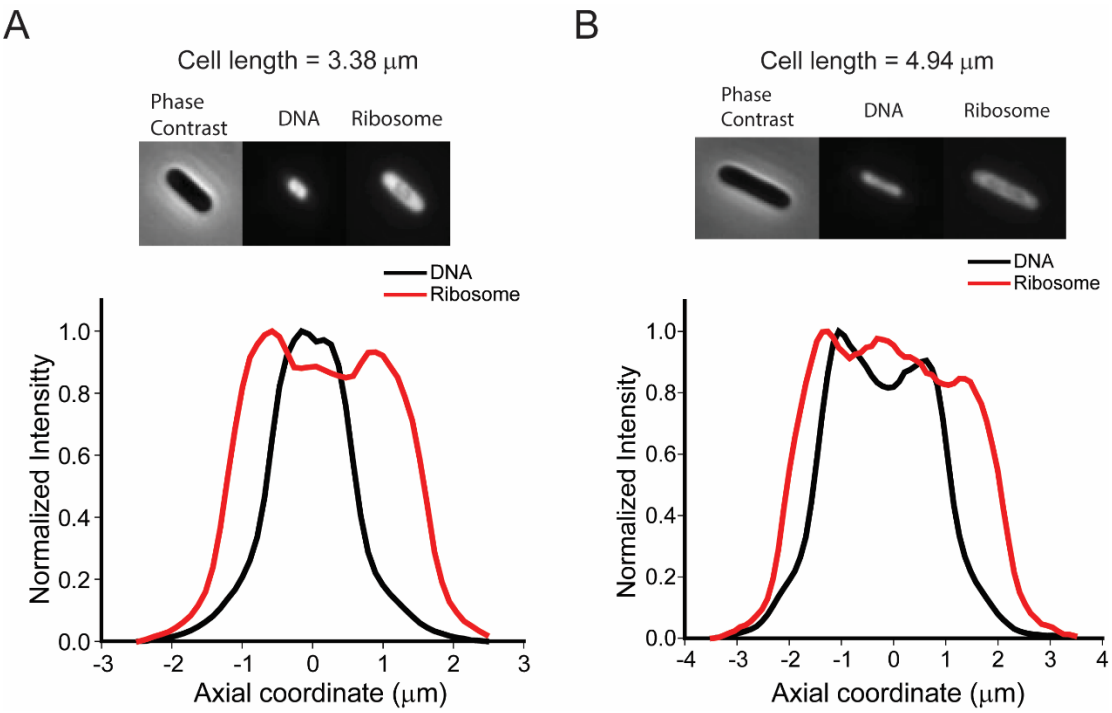

Figure 4.4. *Top row:* Phase contrast cell images and widefield fluorescence images of DNA (Sytox Orange staining) and ribosomes (S2-eYFP labeling) for two different cells treated with Onc112 for at least 30 min. *Bottom row:* Axial projections of the widefield fluorescence images.

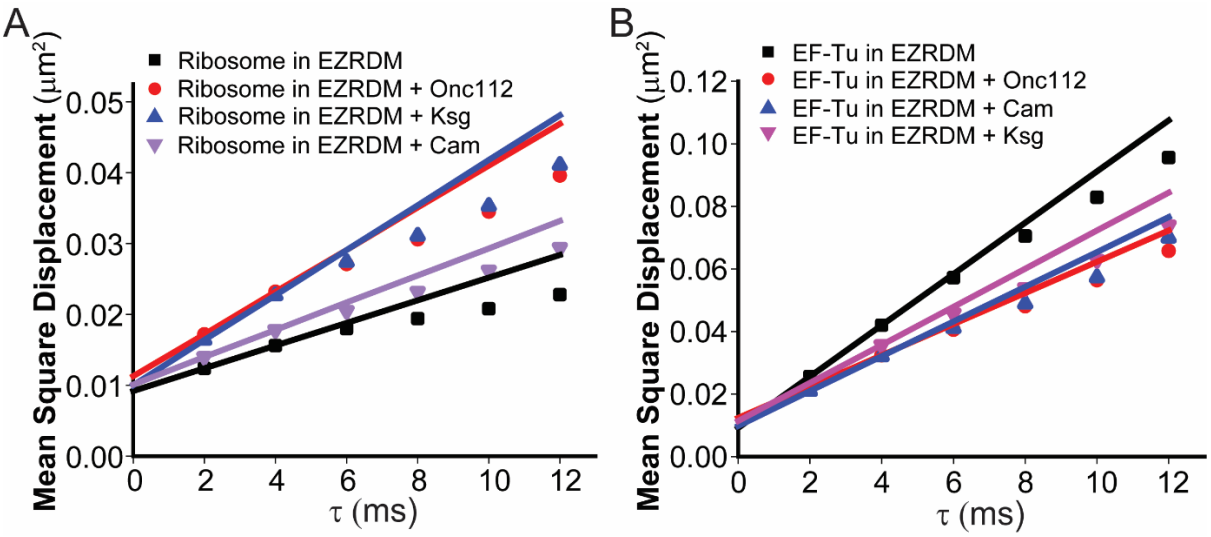

Figure 4.5. A) MSD(τ) plots for ribosomes labeled with the photoswitchable protein mEos2 under different conditions. Average diffusion coefficients D_{Mean} are obtained from the slope of the line through the first two data points as shown. Results are collected in Table 4.1. **B)** As in panel A, MSD(τ) plots for EF-Tu labeled with mEos2. See text and Table 4.1 for average diffusion coefficients D_{Mean} are collected in Table 4.1.

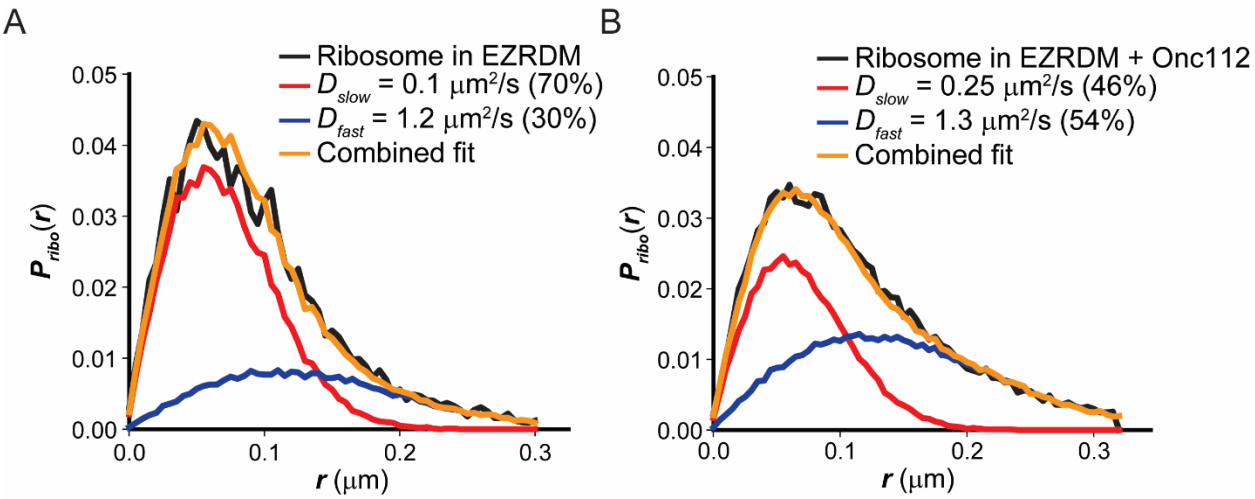

Figure 4.6. Single-step displacement distributions $P_{ribo}(r)$ from single-molecule trajectories (2 ms/frame) of ribosomes labeled by S2-mEos2. Also shown are least-squares best fits from a static, two-state model. **A)** Ribosomes in normal growth conditions. **B)** Ribosomes ~35 min after treatment with 20 μM of Onc112. See text and Table 4.1 for details.

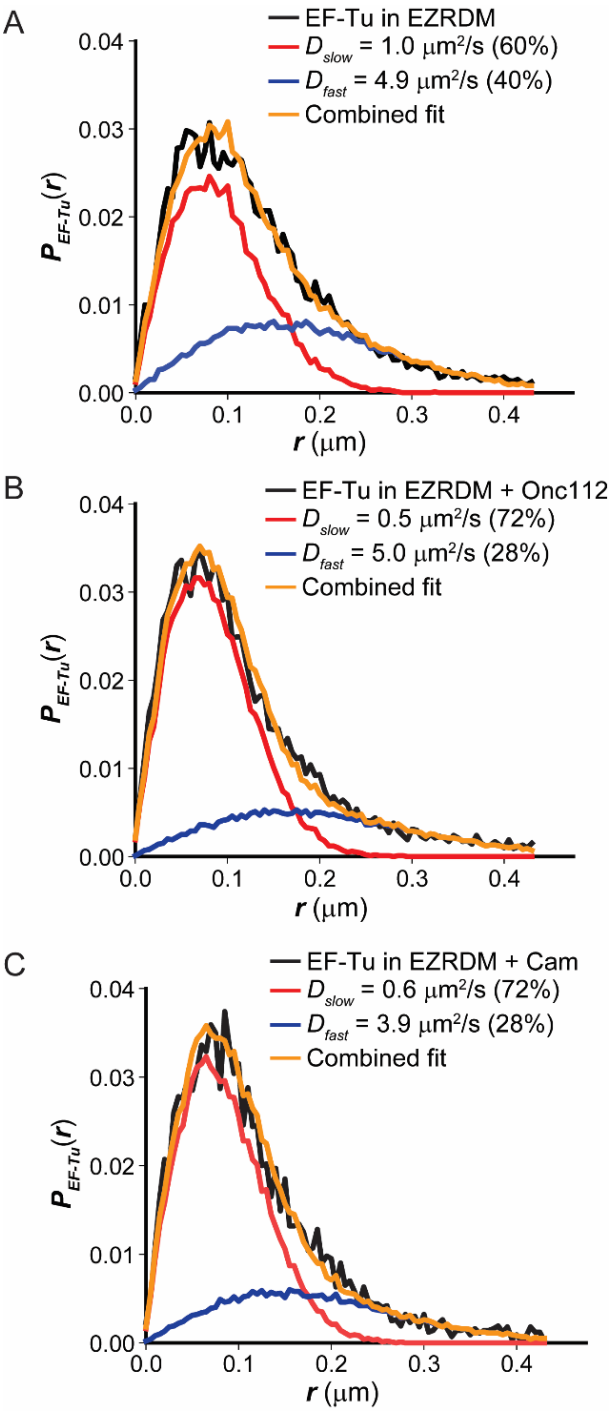

Figure 4.7. Single-step displacement distributions $P_{EF\text{-}Tu}(r)$ from single-molecule trajectories (2 ms/frame) of EF-Tu–mEos2. Also shown are least-squares best fits from a static, two-state model. **A)** Normal growth conditions. **B)** After ~35 min of treatment with 20 μM of Onc112. **C)** After ~35 min of treatment with 300 μg/mL of Cam.

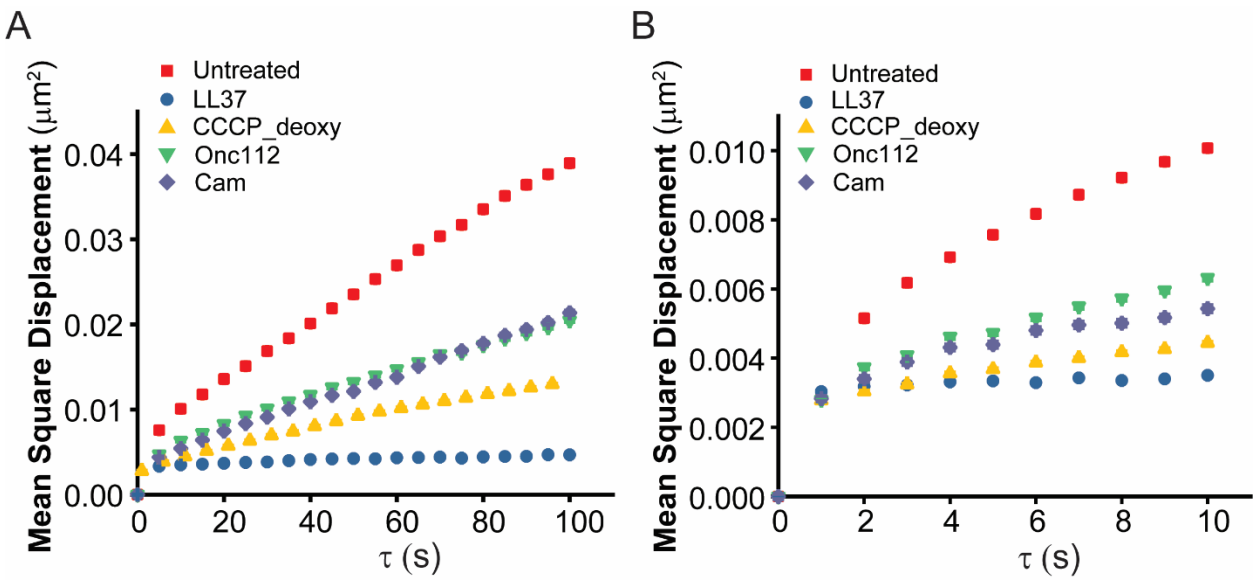

Figure 4.8. MSD(τ) plots from trajectories of the DNA locus *Right2* using the *parS*-ParB-GFP system with imaging at 1 frame/s. Results for untreated cells are compared with those for cells treated with CCCP + 2-deoxy-glucose, LL-37, Onc112, and Cam as described in text. **A)** Lag times from 0–100 s. **B)** Expanded view of the first 10 s. An apparent diffusion coefficient D_{app} is obtained from a linear fit to the first 10 points. The numerical results are: D_{app} = (2.0 ± 0.2) x 10^{-4} μm^2-s^{-1} for normal growth in exponential phase; (4.6 ± 0.2) x 10^{-5} μm^2-s^{-1} after CCCP treatment; (6.6 ± 2.4) x 10^{-6} μm^2-s^{-1} after LL-37 treatment; (8.8 ± 0.6) x 10^{-5} μm^2-s^{-1} after Onc112 treatment; and (6.6 ± 0.6) x 10^{-5} μm^2-s^{-1} after Cam treatment. See text for details.

4.7 References:

[1] Antimicrobial Peptides - 2019

Basics for Clinical Application: Springer; 2019.

[2] Casteels P, Tempst P. Apidaecin-type peptide antibiotics function through a non-poreforming mechanism involving stereospecificity. Biochem Biophys Res Commun. 1994;199:339-45.

[3] Graf M, Mardirossian M, Nguyen F, Seefeldt AC, Guichard G, Scocchi M, et al. Proline-rich antimicrobial peptides targeting protein synthesis. Nat Prod Rep. 2017;34:702-11.

[4] Polikanov YS, Aleksashin NA, Beckert B, Wilson DN. The mechanisms of action of ribosome-targeting peptide antibiotics. Front Mol Biosci. 2018;5:48.

[5] Graf M, Wilson DN. Intracellular antimicrobial peptides targeting the protein synthesis machinery. Adv Exp Med Biol. 2019;1117:73-89.

[6] Mattiuzzo M, Bandiera A, Gennaro R, Benincasa M, Pacor S, Antcheva N, et al. Role of the *Escherichia coli* SbmA in the antimicrobial activity of proline-rich peptides. Mol Microbiol. 2007;66:151-63.

[7] Knappe D, Piantavigna S, Hansen A, Mechler A, Binas A, Nolte O, et al. Oncocin (VDKPPYLPRPRPPRRIYNR-NH2): a novel antibacterial peptide optimized against gram-negative human pathogens. J Med Chem. 2010;53:5240-7.

[8] Knappe D, Kabankov N, Hoffmann R. Bactericidal oncocin derivatives with superior serum stabilities. Int J Antimicrob Agents. 2011;37:166-70.

[9] Roy RN, Lomakin IB, Gagnon MG, Steitz TA. The mechanism of inhibition of protein synthesis by the proline-rich peptide oncocin. Nat Struct Mol Biol. 2015;22:466-9.

[10] Seefeldt AC, Nguyen F, Antunes S, Perebaskine N, Graf M, Arenz S, et al. The proline-rich antimicrobial peptide Onc112 inhibits translation by blocking and destabilizing the initiation complex. Nat Struct Mol Biol. 2015;22:470-5.

[11] Bulkley D, Innis CA, Blaha G, Steitz TA. Revisiting the structures of several antibiotics bound to the bacterial ribosome. Proc Natl Acad Sci U S A. 2010;107:17158-63.

[12] Bakshi S, Choi H, Mondal J, Weisshaar JC. Time-dependent effects of transcription- and translation-halting drugs on the spatial distributions of the *E. coli* chromosome and ribosomes. Mol Microbiol. 2014;94:871-87.

[13] Schluenzen F, Takemoto C, Wilson DN, Kaminishi T, Harms JM, Hanawa-Suetsugu K, et al. The antibiotic kasugamycin mimics mRNA nucleotides to destabilize tRNA binding and inhibit canonical translation initiation. Nat Struct Mol Biol. 2006;13:871-8.

[14] Agrawal A, Weisshaar JC. Effects of alterations of the *E. coli* lipopolysaccharide layer on membrane permeabilization events induced by Cecropin A. BBA-Biomembranes. 2018;1860:1470-9.

[15] Choi H, Rangarajan N, Weisshaar JC. Lights, Camera, Action! Antimicrobial Peptide Mechanisms Imaged in Space and Time. Trends Microbiol. 2016;24:111-22.

[16] Sochacki KA, Barns KJ, Bucki R, Weisshaar JC. Real-time attack on single *Escherichia coli* cells by the human antimicrobial peptide LL-37. Proc Natl Acad Sci U S A. 2011;108:E77.

[17] Choi H, Yang Z, Weisshaar JC. Single-cell, real-time detection of oxidative stress induced in Escherichia coli by the antimicrobial peptide CM15. Proc Natl Acad Sci U S A. 2015;112:E303-10.

[18] Zhu Y, Mohapatra S, Weisshaar JC. Rigidification of the *Escherichia coli* cytoplasm by the human antimicrobial peptide LL-37 revealed by superresolution fluorescence microscopy. Proc Natl Acad Sci U S A. 2019;116:1017.

[19] Schindelin J, Arganda-Carreras I, Frise E, Kaynig V, Longair M, Pietzsch T, et al. Fiji: an open-source platform for biological-image analysis. Nat Methods. 2012;9:676-82.

[20] Bakshi S, Siryaporn A, Goulian M, Weisshaar JC. Superresolution imaging of ribosomes and RNA polymerase in live *Escherichia coli* cells. Mol Microbiol. 2012;85:21-38.

[21] Mustafi M, Weisshaar JC. Simultaneous binding of multiple EF-Tu copies to translating ribosomes in live *Escherichia coli*. mBio. 2018;9:e02143-17.

[22] Bakshi S, Choi H, Weisshaar JC. The spatial biology of transcription and translation in rapidly growing *Escherichia coli*. Front Microbiol. 2015;6:636.

[23] Mustafi M, Weisshaar JC. Near Saturation of Ribosomal L7/L12 Binding Sites with Ternary Complexes in Slowly Growing *E. coli*. J Mol Biol. 2019;431:2343-53.

[24] Gray WT, Govers SK, Xiang Y, Parry BR, Campos M, Kim S, et al. Nucleoid size scaling and intracellular organization of translation across bacteria. Cell. 2019;177:1632-48.e20.

[25] Diaconu M, Kothe U, Schlunzen F, Fischer N, Harms JM, Tonevitsky AG, et al. Structural basis for the function of the ribosomal L7/12 stalk in factor binding and GTPase activation. Cell. 2005;121:991-1004.

[26] Kothe U, Wieden HJ, Mohr D, Rodnina MV. Interaction of helix D of elongation factor Tu with helices 4 and 5 of protein L7/12 on the ribosome. J Mol Biol. 2004;336:1011-21.

[27] Traut RR, Dey D, Bochkariov DE, Oleinikov AV, Jokhadze GG, Hamman B, et al. Location and domain structure of *Escherichia coli* ribosomal protein L7/L12: site specific cysteine crosslinking and attachment of fluorescent probes. Biochem Cell Biol. 1995;73:949-58.

[28] Rudorf S, Thommen M, Rodnina MV, Lipowsky R. Deducing the kinetics of protein synthesis in vivo from the transition rates measured in vitro. PLoS Comput Biol. 2014;10:e1003909.

[29] Rudorf S, Lipowsky R. Protein Synthesis in E. coli: Dependence of Codon-Specific Elongation on tRNA Concentration and Codon Usage. PLoS One. 2015;10:e0134994.

[30] Edelstein AD, Tsuchida MA, Amodaj N, Pinkard H, Vale RD, Stuurman N. Advanced methods of microscope control using μManager software. J Biol Methods. 2014;1.

[31] Paintdakhi A, Parry B, Campos M, Irnov I, Elf J, Surovtsev I, et al. Oufti: an integrated software package for high-accuracy, high-throughput quantitative microscopy analysis. Mol Microbiol. 2016;99:767-77.

[32] Crocker JC, Grier DG. Methods of digital video microscopy for colloidal studies. J Colloid Interface Sci. 1996;179:298-310.

[33] Michalet X. Mean square displacement analysis of single-particle trajectories with localization error: Brownian motion in an isotropic medium. Phys Rev E Stat Nonlin Soft Matter Phys. 2010;82:041914.

4.8 Appendix:

4.8.1 Tables and figures:

Table A4.1: *E. coli* strains and doubling times in EZRDM at 30°C.

Strain label	Description	Doubling time (min)
VH1000	The background strain. Most of the labeled strains are in same background.	45 ± 2
tufAB	Both *tufA* and *tufB* chromosomally labeled with mEos2 at C-terminus.	60 ± 3
MSG196	*rpsB* (ribosome S2 protein) chromosomally labeled with mEos2 at C-terminus.	49 ± 2
MSG192	*rpsB* (ribosome S2 protein) chromosomally labeled with eYFP at C-terminus. (The doubling time for same construct in MG1655 is reported)	~54 [1]
JCW154	*Right2* locus of the chromosome is labeled with parS sites. ParB-GFP is expressed from a plasmid. This strain is in MG1655 background.	~47 [2]

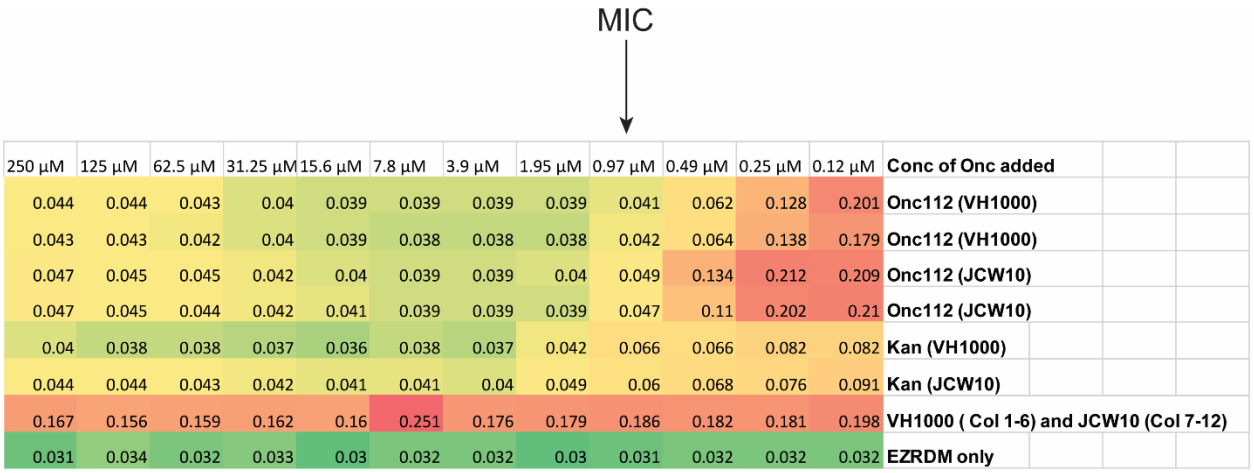

250 µM	125 µM	62.5 µM	31.25 µM	15.6 µM	7.8 µM	3.9 µM	1.95 µM	0.97 µM	0.49 µM	0.25 µM	0.12 µM	Conc of Onc added
0.044	0.044	0.043	0.04	0.039	0.039	0.039	0.039	0.041	0.062	0.128	0.201	Onc112 (VH1000)
0.043	0.043	0.042	0.04	0.039	0.038	0.038	0.038	0.042	0.064	0.138	0.179	Onc112 (VH1000)
0.047	0.045	0.045	0.042	0.04	0.039	0.039	0.04	0.049	0.134	0.212	0.209	Onc112 (JCW10)
0.047	0.045	0.044	0.042	0.041	0.039	0.039	0.039	0.047	0.11	0.202	0.21	Onc112 (JCW10)
0.04	0.038	0.038	0.037	0.036	0.038	0.037	0.042	0.066	0.066	0.082	0.082	Kan (VH1000)
0.044	0.044	0.043	0.042	0.041	0.041	0.04	0.049	0.06	0.068	0.076	0.091	Kan (JCW10)
0.167	0.156	0.159	0.162	0.16	0.251	0.176	0.179	0.186	0.182	0.181	0.198	VH1000 (Col 1-6) and JCW10 (Col 7-12)
0.031	0.034	0.032	0.033	0.03	0.032	0.032	0.03	0.031	0.032	0.032	0.032	EZRDM only

Fig A4.1: The OD values are shown in the heat map. MIC was tested for 2 strains – VH1000 WT strain and JCW10. The MIC value was chosen as the minimum concentration of Onc112 for which there was no appreciable growth of cells after 6 hours.

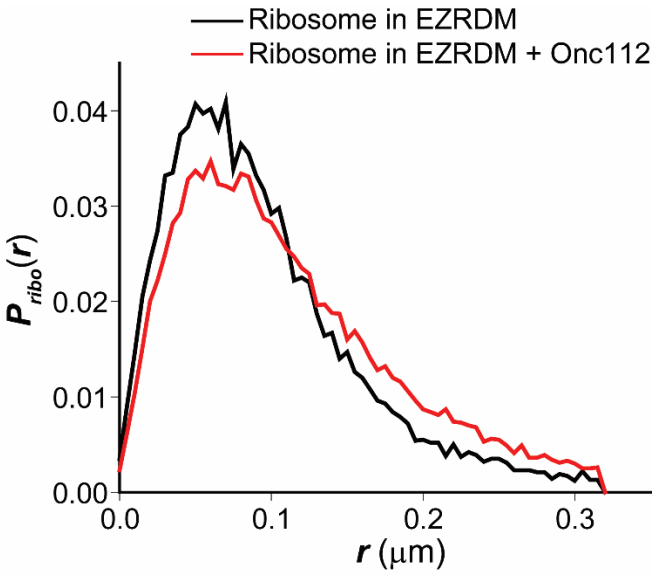

Fig A4.2: The $P_{ribo}(r)$ for untreated and Onc112 treated cells. The ribosome single step displacement distribution of Onc112 treated cells is noticeably faster than that of untreated cells. This indicates there are more free ribosomes in Onc112 treated cells.

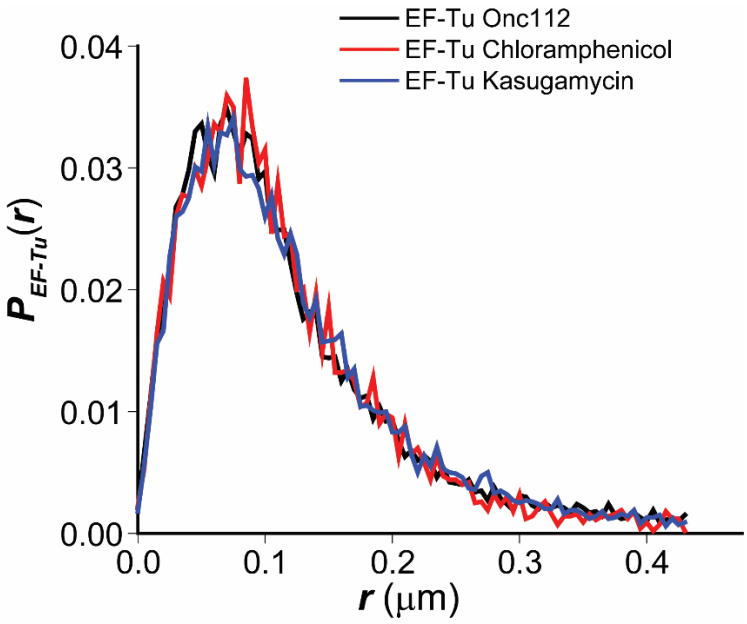

Fig A4.3: The $P_{EF\text{-}Tu}(r)$ for Onc112, Cam and Ksg treated cells. The EF-Tu single step displacement distribution for all the cells are identical. This indicates the effect of all the drugs on the EF-Tu dynamics is similar.

4.8.2 Supplemental references:

[1] Bakshi S, Siryaporn A, Goulian M, Weisshaar JC. Superresolution imaging of ribosomes and RNA polymerase in live *Escherichia coli* cells. Mol Microbiol. 2012;85:21-38.

[2] Choi H, Yang Z, Weisshaar JC. Single-cell, real-time detection of oxidative stress induced in Escherichia coli by the antimicrobial peptide CM15. Proc Natl Acad Sci U S A. 2015;112:E303-10.

Chapter 5

Future Directions

In this thesis, I have detailed our work on understanding the role of EF-Tu in the Translation process. EF-Tu initiates the elongation cycle by bringing an aatRNA to the ribosomes as a ternary complex. Numerous studies have been performed over the years to understand this process. However, it has not been possible to obtain the actual spatio-temporal dynamics picture of such processes till the development of superresolution microscopy. The *in vitro* experiments over the years have deciphered the steps involved in the elongation cycle, but the rates associated with these steps don't portray the actual picture. The rates are too slow for the elongation cycle to complete in ~50 ms. Our measurements suggest, the interaction of ternary complex with ribosomes is extremely short lived. This is also comparable to the theoretical rate estimate. Another aspect of our research was to study how Onc112, a proline rich AMP, affects the translation process. This antibacterial drug has a different mode of interaction with the ribosomes compared to antibiotics like Chloramphenicol (Cam) and Kasugamycin (Ksg). However, our measurements show all these drugs share both similarities and dissimilarities on how they affect the elongation process. Along these lines, these are still a lot of information about the Translation process which eludes us. By using superresolution imaging, it is possible to gain much better understanding of the elongation cycle dynamics. In future, we plan to pursue the following research:

5.1 Studying elongation factor G (EF-G) dynamics in live E. coli:

EF-G is the translation factor which binds to the ribosome after the aatRNA match has been found and EF-Tu has dissociated from the ribosome. EF-G helps with the translocation of the tRNA and mRNA from the A to the P-site. Thus, to understand the elongation cycle completely, it is important to understand the EF-G spatio-temporal dynamics in live cells. Like EF-Tu, EF-G is a GTPase, i.e, it undergoes GTP hydrolysis to perform its enzymatic action. But unlike EF-Tu,

EF-G always undergoes GTP hydrolysis as it only binds when a matching tRNA is found. Thus, studying the EF-G dynamics will give us a proper insight into the rate of GTP hydrolysis, which is the slowest step in the elongation cycle.

5.2 Studying EF-Tu dynamics in stationary phase cells:

All our experiments were done when bacteria reach the exponential phase of its growth. But in most practical scenario, bacteria stay in the stationary phase. In this phase, the cellular dynamics changes drastically. Most of the cellular processes slow down or stop completely. We want to study what is the fate of the elongation cycle in stationary phase. Preliminary data indicates that the unbinding of EF-Tu from the L7/L12 protein slows down significantly. This slowdown can affect the rate of all consecutive steps in the cycle.

5.3 Probing the effect of Api137 on the translation process:

Apidaecin137 (Api137) is a proline rich AMP (PrAMP), like Onc112. Api137 shares some similarities with Onc112. It is a short peptide with net positive charged. It also binds to the peptide exit channel of a ribosome. However, the effect of Api137 on the Translation process is very different compared to Onc112. Api137 stops the termination step of Translation by inhibiting release factor activity. As, only little details are available on PrAMP functions *in-vitro* and *in-vivo*, it is important to gain more insight into these antimicrobial agents. Studying Api137 should give us more information about the structural and other physical characteristics of the PrAMPs which lead to difference in their activity.

Chapter 6:

Why is protein production so efficient?

Communicating research to a non-scientific audience as a part of the Wisconsin Initiative for Science Literacy (WISL) program.

I greatly appreciate the initiative taken by WISL, which allows me and many others to explain our research to a non-scientific audience. All scientific research is done with the goal of being useful to many people. Thus, it is imperative that we get to communicate our findings with others. Thanks to all the members of WISL for providing this platform.

6.1 What kind of chemistry do I do?

Technically, I am a physical chemist, but my research is mostly biological. Thus, I am, more appropriately, a Biophysicist! In physical chemistry, we try to understand how different materials or substances interact with one another. Materials can interact in many ways – similar particles can interact among themselves, or two different particles can interact and lead to the formation of a new substance, etc. Physical chemists are mostly interested in how fast or strong the interactions are, or what kind of energy change is involved, or some other observables like how many particles are interacting. However, as I stated above, I study mostly biological substances, specifically the interactions of different proteins – the entire dynamics of their interaction. This might still seem vague but hopefully should be clearer in the following paragraphs.

6.2 What is my research about?

Our lab – The Weisshaar lab, is dedicated to learning how different biological systems function inside any organism. The smallest block in every organism where complex biological processes occur is a cell. Each cell consists of DNA, RNA and many different proteins. Some examples of these processes are - making different proteins, uptake of nutrients, changing the form of the nutrients, making another copy of DNA, etc. Different cellular systems or machinery carry out different processes and each system includes multiple proteins working together, each

with a different function. The number of cells in an organism vary – Humans have billions of cells in our body, but bacteria only has a single cell. Many of these processes in different organisms share quite a lot of similarities. Thus, we chose our model organism to be a specific bacterium called *E. coli*, as this is a relatively simple system to study. There are different ways to approach the question of understanding cellular processes and the most obvious or the most popular approach is to lyse the cell or disintegrate the cellular membrane by physical or chemical means, which spills all the cellular content. This method allows us to study only that specific protein system. This approach is called *in vitro* study. This approach can also be described as studying a specific cellular system outside the cellular environment. *In vitro* experiments give us a lot of control over what we are studying and has helped the whole scientific community learn a lot about these systems. Scientists have figured out how fast different proteins can interact with one another to carry out their biological functions. Even though it is important to know the rate of such interactions, the results from these experiments can be significantly different from the actual rates. The major issue with such experiments is that the cellular environment can be very different from the *in vitro* environment. This environment plays a major role in determining how fast a protein can move and find its interacting partner. Crowding can slow the motion of a protein but can also bring its interacting partner closer. It has also been observed that the binding interaction between proteins is stronger inside cells compared to *in vitro* [1]. Our lab's research has been focused on studying the live cell dynamics of different cellular processes. My research has been focused on understanding the dynamics of a specific process called Translation inside live cells.

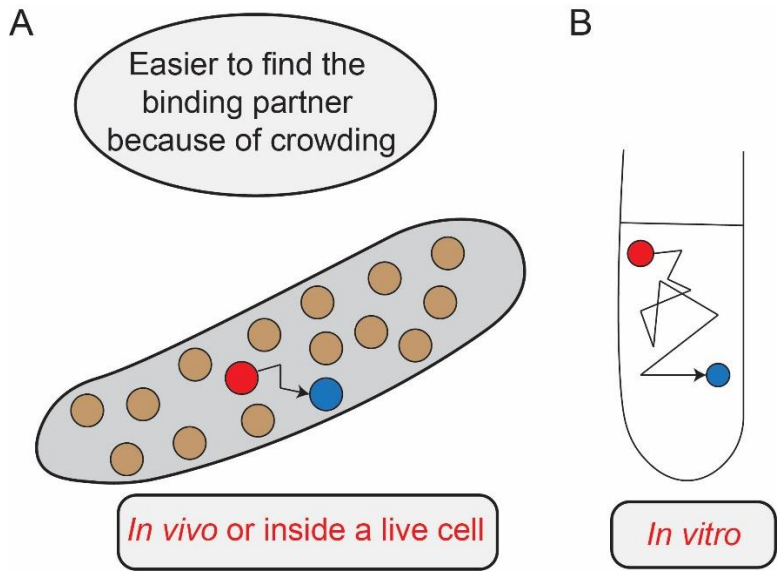

Fig 6.1: A) Cartoon representation of protein interaction inside a bacterial cell. Due to crowding from other proteins, the rate of protein interaction can increase as they can come closer to each other. **B)** Cartoon representation of *in vitro* conditions. In this example the rate of interaction is significantly lower in *in vitro* conditions. Proteins are not drawn to scale.

6.3 What technique do we use?

A very efficient way to visualize what happens inside a live cell is by fluorescence imaging. To understand this technique, we should have some background about fluorescence. There are certain materials that when illuminated by light of a specific color, absorb that light and emit light of a different color. This emission is called fluorescence. Not all materials show fluorescence. The ones that do are called fluorophores. Many materials are fluorophores, including some proteins. For our imaging experiments, we attach a fluorescent protein to the protein we want to study, and now the fluorescent light can show us how the protein of interest is moving around. We look at these fluorescence emissions under a microscope to understand the dynamic behavior of the protein.

This seems very straightforward and an efficient way to study protein dynamics. But this technique has a huge limitation – the resolution. Anything smaller than ~250 nm cannot be seen under a microscope [2]. They appear as a blob of 250 nm radius. To give a perspective of the size, human hair is around the thickness of ~0.1 mm (1 mm = 1,000,000 nm), which is around 400 times larger than this resolution limit. Thus, substances as small as hair can easily be seen in a microscope. Then what is the issue? Well, the average protein size is around 2-10 nm. Thus, it is around 10,000-50,000 times smaller than the thickness of human hair. Also, a bacterium itself is around 4 µm long and 1 µm thick (1 µm = 1,000 nm). Thus, it is 100 times smaller than hair. The proteins inside the bacteria are not very far apart and usually there are thousands of them. So, it is very difficult to tell them apart by fluorescence microscopy.

In 2006, three research groups had a breakthrough in the resolution limit problem of microscopy [3-5]. They had figured out a way, by using special fluorophores or fluorescent proteins, to achieve resolution around 30 nm. Now, there was a way to study these protein interactions inside the crowded bacterial cell. This superresolution imaging technique was called Photoactivatable Localization Microscopy (PALM). Prof Eric Betzig received the Nobel Prize in 2014 for its development. For my research, I use the PALM technique to visualize translation of specific proteins in a cell and understand their dynamics inside the live cell.

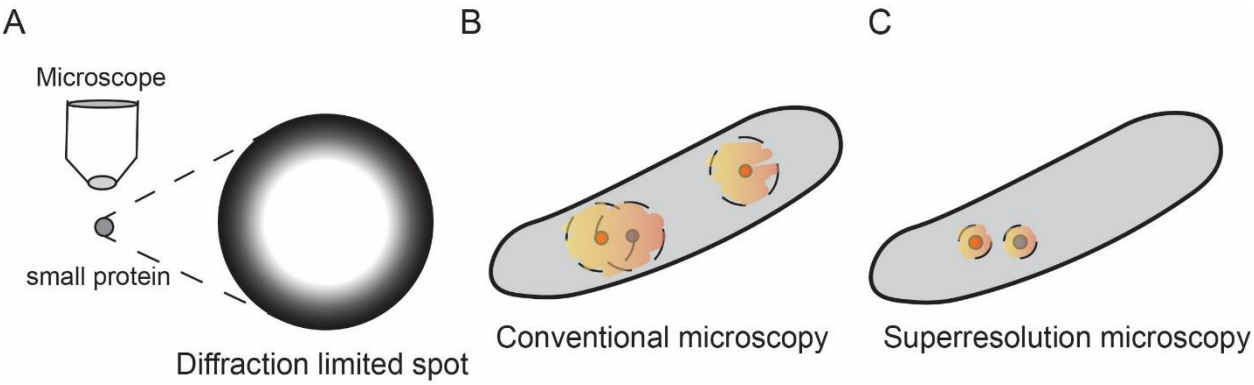

Fig 6.2: A) When the fluorescence of a small protein is viewed under a microscope, it appears as a giant blob of light. This limits our ability to differentiate 2 proteins when they are close to each other. **B)** Figure showing how the fluorescence image of two small proteins present very close to each other inside a bacterial cell will appear. The yellowish orange region represents the fluorescence image. **C)** Figure showing how the fluorescence image of the same proteins look by using superresolution microscopy. Now, it is much easier to track individual proteins.

6.4 What is translation and what have I discovered?

Translation is an essential and complex process in which new proteins are formed in a cell. The process involves numerous different proteins working in tandem. The most important component involved in translation is called a Ribosome. Ribosomes are huge complexes made up of both proteins and RNA. They are the largest component of a bacterial cell. The term DNA might be familiar to most. It is the genetic material inside every organism. Differences in DNA among individuals lead to differences in physical features, etc. There is another material which is like DNA inside every organism called RNA. RNA is produced from DNA by a process called transcription. Similar to DNA, RNA is coded to determine which proteins should be produced and in what quantity. When RNA is formed, they travel to the ribosomes, which then decode the RNA and make proteins. Many proteins help the ribosomes in this process. One such protein is

Elongation Factor-Tu (EF-Tu). EF-Tu binds to a specific region of a ribosome and helps start the protein making process [6].

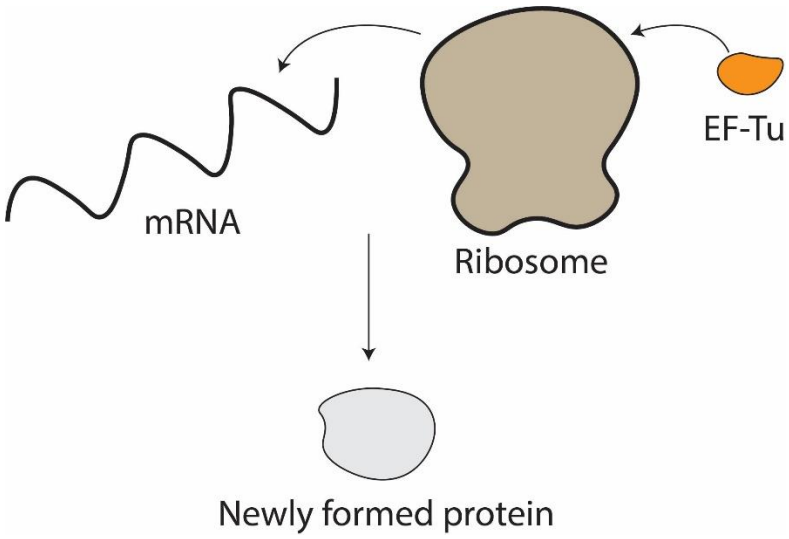

Fig 6.3: Schematic representation of how the translation process works. Ribosome binds to the mRNA (messenger RNA) and EF-Tu binds to the ribosome to start the translation process. The product is a newly formed protein.

I used PALM to study how exactly EF-Tu interacts with ribosomes and found few, previously unknown, interesting components in the Translation pathway. First, I was able to estimate the speed of this interaction, which helps us understand the rate of the entire translation process. My measured rate was drastically different from the rate measured by *in vitro* experiments, which were deemed to be very slow. I also observed that multiple EF-Tu can bind to the same ribosome, which helps us understand why Translation process is so efficient and why the rate of translation is so high [7].

After developing a proper understanding of the EF-Tu dynamics in live cells, I tried to understand if the motion of EF-Tu in the bacteria had any effect on the rate of translation overall.

These proteins move around in a cell crowded by thousands of different proteins and must find their target efficiently. Thus, the crowding can change the rate of the cellular processes. To verify this hypothesis, I changed the cellular crowding by changing the growth conditions of the bacterial cells and measured the EF-Tu dynamics in the different conditions. Surprisingly, the dynamics hardly changed even though the overall translation rate changed significantly. This showed that the translation rate was independent of the motion of EF-Tu in a cell [8].

Bacterial resistance to antibiotics is one of the global challenges we face. Many scientists are doing research to develop new means to kill bacteria. I wanted to contribute to this effort with my knowledge of the Translation process. I started doing experiments to understand how different antibiotics or antimicrobial peptides affect this process. As I stated, translation is an extremely important process which occurs in every cell. Stopping this process can lead to bacterial death. To stop bacterial infections, scientists have developed numerous antibiotics to target the translation process. But our understanding of their effect isn't perfect. Thus, I studied a few such anti-bacterial materials to understand their effect on EF-Tu and ribosome dynamics.

6.5 What is the significance of my research?

Translation is one of the most important processes occurring in a cell: it determines which proteins will get produced in what quantity. These proteins, in turn, contribute to the proper functioning of the cell or the organism itself. Thus, it is important to understand how Translation occurs. Even though much research has been done to understand the translation process, our understanding of it is far from perfect. Also, most of these studies were done *in vitro*, which might not represent the actual picture. My findings shed light on this important process. I have reported how fast the EF-Tu – Ribosome interaction can occur and why the

translation process is very efficient. I also show how different the actual rate can be compared to the *in vitro* experiments.

The other part of my research was focused on understanding the difference in the effects of different anti-bacterial agents on the translation process. A lot of research is being done to produce different anti-bacterial drugs, but their exact effect is unknown. It is important to understand how different physical characteristics of these drugs – like structure, if they can or cannot function in water (called hydrophilicity or hydrophobicity, respectively), etc. - can lead to very different effects. If we can understand how different physical characteristics of drugs create specific effects, we can optimize those drugs to make them more efficient. By studying these characteristics and their effects, we may also be able to discover unknown steps in the translation process. I found one such step in the EF-Tu binding process, which is important in the overall mechanism.

Understanding processes like Translation is vitally important because this knowledge paves the path for drug development. Much research centers on treating bacterial infections, and as mentioned above, many of the drugs lose their efficacy in a short period of time. Thus, newer drugs are developed to target other functional aspects of the bacterium. By understanding these vital processes, we can develop newer targets to combat bacterial infections. Also, understanding the mechanism of current antibacterial drugs can help us optimize their functionality, increasing their antibacterial potency.

6.6 References:

[1] Phillip Y, Schreiber G. Formation of protein complexes in crowded environments – From *in vitro* to *in vivo*. FEBS Lett. 2013;587:1046-52.

[2] Abbe E. Beiträge zur Theorie des Mikroskops und der mikroskopischen Wahrnehmung. Archiv für Mikroskopische Anatomie. 1873;9:413-68.

[3] Betzig E, Patterson GH, Sougrat R, Lindwasser OW, Olenych S, Bonifacino JS, et al. Imaging intracellular fluorescent proteins at nanometer resolution. Science. 2006;313:1642-5.

[4] Rust MJ, Bates M, Zhuang X. Sub-diffraction-limit imaging by stochastic optical reconstruction microscopy (STORM). Nat Methods. 2006;3:793-5.

[5] Hess ST, Girirajan TPK, Mason MD. Ultra-high resolution imaging by fluorescence photoactivation localization microscopy. Biophys J. 2006;91:4258-72.

[6] Voorhees RM, Ramakrishnan V. Structural basis of the translational elongation cycle. Annu Rev Biochem. 2013;82:203-36.

[7] Mustafi M, Weisshaar JC. Simultaneous binding of multiple EF-Tu copies to translating ribosomes in live *Escherichia coli*. mBio. 2018;9:e02143-17.

[8] Mustafi M, Weisshaar JC. Near Saturation of Ribosomal L7/L12 Binding Sites with Ternary Complexes in Slowly Growing *E. coli*. Journal of molecular biology. 2019;431:2343-53.